

UNCLASSIFIED

267 522

*Reproduced
by the*

**DEFENSE SERVICES TECHNICAL INFORMATION AGENCY
ARLINGTON HALL STATION
ARLINGTON 12, VIRGINIA**



UNCLASSIFIED

Best Available Copy

NOTICE: When government or other drawings, specifications or other data are used for any purpose other than in connection with a definitely related government procurement operation, the U. S. Government thereby incurs no responsibility, nor any obligation whatsoever; and the fact that the Government may have formulated, furnished, or in any way supplied the said drawings, specifications, or other data is not to be regarded by implication or otherwise as in any manner licensing the holder or any other person or corporation, or conveying any rights or permission to manufacture, use or sell any patented invention that may in any way be related thereto.

267522

WADD TECHNICAL REPORT 61-133
VOLUME II

XEROX
62-1-4

**PASSIVE AERODYNAMIC ATTITUDE STABILIZATION
OF NEAR EARTH SATELLITES**

**Volume II
AERODYNAMIC ANALYSIS**

PAUL H. DAVISON
NORTH AMERICAN AVIATION, INC.
COLUMBUS, OHIO

JULY 1961

ASTIA
JUL 11 1961

AERONAUTICAL SYSTEMS DIVISION

Best Available Copy

NOTICES

When Government drawings, specifications, or other data are used for any purpose other than in connection with a definitely related Government procurement operation, the United States Government thereby incurs no responsibility nor any obligation whatsoever, and the fact that the Government may have formulated, furnished, or in any way supplied the said drawings, specifications, or other data, is not to be regarded by implication or otherwise as in any manner licensing the holder or any other person or corporation, or conveying any rights or permission to manufacture, use, or sell any patented invention that may in any way be related thereto.

Qualified requesters may obtain copies of this report from the Armed Services Technical Information Agency, (ASTIA), Arlington Hall Station, Arlington 12, Virginia.

This report has been released to the Office of Technical Services, U. S. Department of Commerce Washington 25, D. C., for sale to the general public.

Copies of ASD Technical Reports and Technical Notes should not be returned to the Aeronautical Systems Division unless return is required by security considerations, contractual obligations, or notice on a specific document.

WADD TECHNICAL REPORT 61-133
VOLUME II

**PASSIVE AERODYNAMIC ATTITUDE STABILIZATION
OF NEAR EARTH SATELLITES**

Volume II
AERODYNAMIC ANALYSIS

PAUL H. DAVISON
NORTH AMERICAN AVIATION, INC
COLUMBUS, OHIO

JULY 1961

FLIGHT DYNAMICS LABORATORY
CONTRACT N. AF 33(616)-7100
PROJECT Nr 1366
TASK Nr 13967

AERONAUTICAL SYSTEMS DIVISION
AIR FORCE SYSTEMS COMMAND
UNITED STATES AIR FORCE
WRIGHT PATTERSON AIR FORCE BASE, OHIO

FOREWORD

The research reported herein was performed by North American Aviation, Inc., Columbus, Ohio for the Hypersonic Flight Section, Flight Branch of the Flight Dynamics Laboratory, Wright Air Development Division. The work was accomplished under Air Force Contract No. AF 33(616)-7100, Project No. 1766, Task No. 13967, "A Study of Aerodynamically Oriented and Stabilized Satellites." This research was carried out by the Engineering Research and Aerothermodynamics Development Groups of the Columbus Division, North American Aviation, Inc., with Dr. D. H. Schelle, Engineering Research Group, as Project Engineer. Mr. Joseph Ondrejka, Flight Dynamics Laboratory, was WADD Project Engineer.

The results of this study are reported in a series of three volumes of which this is Volume II. The other reports in this series are:

VOLUME I: "Librations due to Combined Aerodynamic and Gravitational Torques," by D. H. Schelle

VOLUME III: "Mathematical Techniques and Computer Program," by O. C. Juelich

Particular credit should be given to Mr. J. E. Shuter for his contributions to the analysis of the more complex satellite shapes presented in this report.

ABSTRACT

Aerodynamic drag and stability coefficients of several simple satellite configurations are calculated using an approximate, but nearly exact, free molecule theory. The models examined are the cylinder-sphere, pointed cone, truncated cone, power law body, hemisphere-cylinder and cone-cylinder. From the viewpoint of maximum aerodynamic effects, favorable center-of-mass locations are obtained by concentrating a homogeneous payload forward of the center-of-volume. For calculation purposes, the aft portion of the models are assumed to be rigid, but massless, shells or skirts.

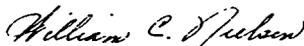
Based upon the analysis of satellite angular motion, the aerodynamic pitching moment slope is combined with the pitching moment of inertia to form a stability parameter which, when maximized, describes the optimum external geometry of each model for a specified payload mass distribution. The various optimum configurations are shown to have low fineness ratios (order of unity), thereby permitting the gravitational torque to augment the aerodynamic torque. Among the configurations analyzed, the pointed and truncated conical bodies and the power law bodies are the most stable.

The aerodynamic damping-in-pitch derivative is also calculated for the cylinder, sphere and cone. Aerodynamic damping, however, has an insignificant contribution to the satellite's angular motion.

PUBLICATION REVIEW

This report has been reviewed and is approved.

FOR THE COMMANDER:



WILLIAM C. NIELSEN
Colonel, USAF
Chief, Flight Dynamics Laboratory

TABLE OF CONTENTS

	<u>Page No.</u>
INTRODUCTION	1
DISCUSSION	
1. Review of Free Molecule Aerodynamics	3
1.1 Introduction	3
1.2 Shear and Pressure Coefficients	3
1.3 Force and Moment Equations	7
2. Drag Analysis	14
2.1 Introduction	14
2.2 Cylinder	14
2.3 Cone	17
2.4 Sphere	20
2.5 Flat Plate	20
2.6 Summary of Configurations	22
3. Static Stability Analysis	29
3.1 General Considerations	29
3.2 Aerodynamic Pitching Moment	30
3.2.1 Introduction	30
3.2.2 Pitching Moment of Basic Body Shapes	30
3.2.2.1 Cylinder	30
3.2.2.2 Sphere	32
3.2.2.3 Cone	34
3.2.3 Pitching Moment Slopes of Complex Body Shapes	44
3.2.3.1 Power Law Body	44
3.2.3.2 Truncated Cone	46
3.2.3.3 Hemisphere-Cylinder	49
3.2.3.4 Cone-Cylinder	50
3.3 Miscellaneous Effects on Stability	52
3.3.1 Introduction	52
3.3.2 Effect of Uniform Temperature Level on Stability	52
3.3.2.1 Cylinder	52
3.3.2.2 Sphere	53
3.3.2.3 Cone	53
3.3.3 Effect of Asymmetric Temperature Variation on Stability	58
3.3.4 Effect of Longitudinal Temperature Distribution on Stability	62

3.3.4	Effect of Asymmetric Reflection Coefficient Variations on Stability	65
3.3.6	Effect of Non-Diffuse Reflection Coefficients on Stability	65
3.3.6.1	Cylinder	66
3.3.6.2	Sphere	66
3.3.6.3	Cone	66
3.4	Optimum Shapes	74
3.4.1	review and Introduction	74
3.4.2	Basic Body Shapes	76
3.4.2.1	Cylinder	76
3.4.2.2	Sphere	77
3.4.2.3	Cone	77
3.4.2.4	Comparison of Basic Body Shapes	78
3.4.3	Complex Body Shapes	91
3.4.3.1	Power Law Body	91
3.4.3.2	Truncated Cone	95
3.4.3.3	Hemisphere-Cylinder	102
3.4.3.4	Cone-Cylinder	110
4.	Dynamic Stability Analysis	116
4.1	General Considerations	116
4.2	Damping-in-Pitch of Basic Body Shapes	117
4.2.1	Introduction	117
4.2.2	Cylinder	117
4.2.3	Sphere	120
4.2.4	Cone	121
4.2.5	Comparison of Basic Body Shapes	120
	CONCLUSIONS	137
	APPENDIX A - THE EFFECT OF SOLAR RADIATION PRESSURE ON SATELLITE TORQUE	142
	BIBLIOGRAPHY	151

LIST OF FIGURES

<u>Figure</u>		<u>Page No.</u>
1.	Vector Diagram for Body of Revolution	13
2.	Temperature and Molecular Speed Ratio	23
3.	Cylinder Drag Coefficients	24
4.	Cone Drag Coefficients	25
5.	Sphere Drag Coefficients	26
6.	Flat Plate Drag Coefficients	27
7.	Correlation of Drag Coefficients	28
6.	Cylinder Nomenclature	30
9.	Sphere Nomenclature	32
10.	Cone Nomenclature	34
11.	Cylinder Static Pitching Moment Versus Angle of Attack - $\lambda/D = 1$	37
12.	Cylinder Static Pitching Moment Versus Angle of Attack - $\lambda/D = 2$	38
13.	Cylinder Static Pitching Moment Versus Angle of Attack - $\lambda/D = 5$	39
14.	Sphere Static Pitching Moment Versus Angle of Attack	40
15.	Cone Static Pitching Moment Versus Angle of Attack - $\delta = 15^\circ$	41
16.	Cone Static Pitching Moment Versus Angle of Attack - $\delta = 30^\circ$	42
17.	Cone Static Pitching Moment Versus Angle of Attack - $\delta = 45^\circ$	43
18.	Power Law Body Nomenclature	4
19.	Truncated Cone Nomenclature	46
20.	Hemisphere-Cylinder Nomenclature	48

<u>Figure</u>	<u>Page No.</u>
21. Cone-Cylinder Nomenclature	50
22. Effect of Surface Temperature on Cylinder Static Pitching Moment	54
23. Effect of Surface Temperature on Sphere Static Pitching Moment	55
24. Effect of Surface Temperature on Cone Static Pitching Moment	56
25. Effect of Surface Temperature on Cone Static Pitching Moment Slope	57
26. Body of Revolution at Zero Angle of Attack	58
27. Effect of Longitudinal Temperature Distribution on Cone Pitching Moment Slope	64
28. Effect of $\sigma \neq \sigma' \neq 1$ on Cylinder $C_{m\alpha}$	71
29. Effect of $\sigma \neq \sigma' \neq 1$ on Sphere $C_{m\alpha}$	72
30. Effect of $\sigma \neq \sigma' \neq 1$ on Cone $C_{m\alpha}$	73
31. Cylinder Nomenclature	76
32. Sphere Nomenclature	79
33. Sphere Inertia and Volume Characteristics	81
34. Cone Nomenclature	82
35. Comparison of Basic Body Shapes - $v/v_T = 1/4$	87
36. Comparison of Basic Body Shapes - $v/v_T = 1/2$	88
37. Comparison of Basic Body Shapes - $v/v_T = 3/4$	89
38. Comparison of Basic Body Shapes - $v/v_T = 1$	90
39. Power Law Body Nomenclature	91
40. Static Stability Parameter $(\Gamma m/v^{1/3})_{\max}$ for Power Law Bodies	95
41. Truncated Cone Nomenclature	96

<u>Figure</u>		<u>Page No.</u>
42.	Static Stability Parameter $(\Gamma m / r^{1/3})_{\max}$ for Truncated Cones	107
43.	Hemisphere-Cylinder Nomenclature	102
44.	Comparison of Hemisphere-Cylinder Configurations - $r/r_T = 1/4$	107
45.	Comparison of Hemisphere-Cylinder Configurations - $r/r_T = 1/2$	107
46.	Comparison of Hemisphere-Cylinder Configurations - $r/r_T = 3/4$	109
47.	Cone-Cylinder Nomenclature	110
48.	Comparison of Cone-Cylinder Configurations - $r/r_T = 1/4$	113
49.	Comparison of Cone-Cylinder Configurations - $r/r_T = 1/2$	114
50.	Comparison of Cone-Cylinder Configurations - $r/r_T = 3/4$	115
51.	Cylinder Damping-in-Pitch Derivative Versus Angle of Attack - $l/D = 1$	127
52.	Cylinder Damping-in-Pitch Derivative Versus Angle of Attack - $l/D = 2$	128
53.	Cylinder Damping-in-Pitch Derivative Versus Angle of Attack - $l/D = 5$	128
54.	Effect of Surface Temperature on Cylinder Damping-in-Pitch	130
55.	Sphere Damping-in-Pitch Derivative Versus Angle of Attack	131
56.	Effect of Surface Temperature on Sphere Damping-in-Pitch	132
57.	Cone Damping-in-Pitch Derivative Versus Angle of Attack - $\delta = 15^\circ$	133
58.	Cone Damping-in-Pitch Derivative Versus Angle of Attack - $\delta = 30^\circ$	134

<u>Figure</u>		<u>Page No.</u>
59.	Cone Darning-in-Fitch Derivative Versus Angle of Attack - $\delta = 45^\circ$	175
60.	Effect of Surface Temperature on Cone Darning-in-Fitch	176
61.	Comparison of Basic Body Shapes - $\sqrt{r}/r_T = 1/2$	177
62.	Comparison of Basic Body Shapes - $\sqrt{r}/r_T = 3/4$	178

LIST OF TABLES

<u>Table</u>		<u>Page No.</u>
1.	Cylinder Summary	73
2.	Sphere Summary	81
3.	Cone Summary	82
4.	Power Law Body Summary	94
5.	Truncated Cone Summary	99

LIST OF SYMBOLS

A	Area
B, C	Truncated cone parameters, defined by Eqs. (153)
c	Photon speed
\bar{c}	Reference length
C_D	Drag coefficient = (Drag) / $\frac{1}{2} \rho_\infty V_\infty^2 S_H$
C_D^+	Drag coefficient based on projected frontal area normal to free-stream = (Drag) / $\frac{1}{2} \rho_\infty V_\infty^2 S^+$
C_L	Lift coefficient = (Lift) / $\frac{1}{2} \rho_\infty V_\infty^2 S_H$
C_m	Pitching moment coefficient = (Pitching moment) / $\frac{1}{2} \rho_\infty V_\infty^2 S_H \bar{c}$
$C_{m\alpha}$	Pitching moment slope = $\partial(C_m) / \partial\alpha$
C_{m0}	Pitching moment at zero angle of attack
C_{mq}	Damping-in-pitch derivative = $\partial(C_m) / \partial(q\bar{c} / 2V_\infty)$
C_p	Pressure coefficient, defined by Eq. (7)
C_T	Shear stress coefficient, defined by Eq. (5)
D	Maximum or base diameter of satellite
$f(\epsilon), \eta(\epsilon), h(\epsilon), p(\epsilon)$	Universal free-molecule flow functions, defined by Eqs. (45), (46), (41) and (42) respectively
$\tilde{f}(\epsilon), \tilde{\eta}(\epsilon), \tilde{h}(\epsilon), \tilde{p}(\epsilon)$	Universal free-molecule flow functions, defined by Eqs. (71) and (193)
$F(\xi), G(\xi)$	Exact cylinder functions, defined by Eqs. (32)
h	Altitude
I_0, I_1	Modified Bessel functions of the first kind
\bar{I}	Principal moment of rotary inertia about the γ body-fixed axis

\bar{I}_x	Principal moment of rotary inertia about the x body-fixed axis
J, K	Cone-cylinder parameters, defined by Eqs. (89)
l	Body length
l_c	Length of cylindrical portion of satellite
L	Torque or moment
m	Mass
M	Inertia parameter $\equiv (\bar{I}_x - \bar{I}) / \bar{I}$
n	Power law body exponent, defined by Eq. (74)
\bar{N}	Inward normal vector in an element of surface area
P	Pressure
G_p^*	Dimensionless aerodynamic stability parameter, defined by Eq. (121)
q	Angular pitching velocity component
\vec{Q}	Position vector, defined in Fig. 1
$Q(\xi_m)$	Exact sphere function, defined by Eq. (50)
α_p^*	Dimensionless aerodynamic damping-in-pitch parameter, defined by Eq. (175)
λ	Reflectivity
r	Geocentric radius to satellite mass center
r, θ, x	Cylindrical coordinate system, defined in Fig. 1 or Fig. 2b
r'	Body slope $= dr/dx$
R	Maximum or base radius of satellite $= \frac{1}{2} D$
S	Molecular speed ratio
S_R	Reference area
S^*	Projected body frontal area normal to free-stream

t	Dummy variable
\vec{T}	Tangent vector in an element of surface area
T	Absolute temperature
V	Satellite payload volume
V_T	Total satellite volume
V_∞	Free-stream speed = V_R , the satellite speed relative to local atmosphere
W	Satellite payload weight at sea level
X, Y	Hemisphere-cylinder parameters, defined by Eqs. (85)
α	Angle of attack
α_e	Equilibrium angle of attack
β	Truncated cone nose-to-base diameter ratio
Γ	Aerodynamic stability parameter, defined by Eq. (122)
Γ_f	Aerodynamic damping-in-pitch parameter, defined by Eq. (176)
δ	Cone semivertex angle
Δ	An increment due to temperature differences
$\Delta\sigma, \Delta\sigma'$	$\sigma_x - \sigma_u$ and $\sigma_x' - \sigma_u'$
ϵ	Spherical payload length-to-diameter ratio, defined in Fig. 32
$\epsilon(S, \sigma)$	Error incurred by a two term approximation to the Gaussian error function, defined by Eq. (11)
ζ	Dimensionless slope parameter $\equiv r'/t \tan \alpha$
η	Ratio of payload length to total satellite length
Θ	Pitch angle, the inclination between X body-fixed axis and local horizon
Θ	Reference temperature ratio

λ	Photon reflection coefficient
μ	Product of Earth's mass and universal gravitational constant
ν	Temperature distribution exponent
F	Dimensionless speed ratio function in exact cylinder solution
ρ_{∞}	Atmospheric density
σ	Surface reflection coefficient for tangential momentum, defined by Eq. (3)
σ'	Surface reflection coefficient for normal momentum, defined by Eq. (4)
$\sigma_{\lambda}, \sigma_{\lambda}'$	$(\sigma_{\lambda} + \sigma_{\mu})/2$ and $(\sigma_{\lambda}' + \sigma_{\mu}')/2$
τ	Shear stress
δ_m	Limiting azimuth angle on surface exposed to free-stream flow

Subscripts

A	Aerodynamic; also average
cm	Center of mass
d, D	Value of a quantity for wholly diffuse reflection
g	Gravitational
HC	Hemisphere-cylinder
i	Incident quantity
l	Quantity evaluated on lower surface; or quantity evaluated at semi-latus rectum
N	Component normal to surface = $(\vec{i}) \cdot \vec{N}$
max	Maximum value of a quantity
p	Quantity evaluated at perigee

r	Reflected quantity
S	Quantity evaluated on shielded or shadow side of body; also solar
T	Component tangent to surface = $(\vec{n}) \cdot \vec{T}$
u	Quantity evaluated on upper surface
w	Quantity evaluated at wall or surface
x	About x body-fixed axis
y	About y body-fixed axis
∞	Free-stream conditions

INTRODUCTION

Although the effects of rarefied aerodynamic forces on satellite performance (e.g., orbit decay) have, by necessity, been extensively considered, there has been little concern over the utilization of these forces for passive attitude control and stability of satellite vehicles. This rather mild interest appears to have been primarily due to the uncertainty of the characteristics of the upper atmosphere (say in excess of 100 miles altitude) as well as to the reluctance to accept relatively unproven (or unknown) methods of estimating rarefied aerodynamic characteristics. With improved and more frequent experimental investigations, however, the physics of the upper atmosphere is becoming more clearly understood. Likewise, through the inspiration of Schaaf, Patterson, Stalder and their colleagues (Refs. 1, 3, 5, 8, 9, 12, 13, 17), the experimental and analytical determination of the mechanics of rarefied gases is being continually advanced. Consequently, it is expected that satellite aerodynamics in the near-Earth regime (say less than 400 miles altitude) will warrant increased attention as more sophisticated vehicles are inherently utilized.

The application of rarefied gas kinetics; viz., free-molecule aerodynamics, has been, until recently, hopelessly complicated for all but a few academic problems. These classical applications (e.g., Refs. 8, 17, 18), however, have provided foundations which have led to the development of approximate free-molecule methods for estimating aerodynamic forces and moments on convex bodies. One notable, but restrictive, approach is the "Newtonian-Diffuse" method of Gustafson (Ref. 19, 20) which implies that the random molecular motion is insignificant when compared with the vehicle's motion. Another more general free-molecule theory (Ref. 6) was developed which considerably simplified the force and moment calculations without seriously compromising the accuracy of the results. This method, which is outlined and used herein, only requires that the average normal component of the molecular speed ratio be greater than unity over the portion of the body surface exposed to the free-stream. For most satellite configurations, however, this requirement is compatible with the expected conditions. Moreover, there are no assumptions as to the nature of the molecule-surface interaction process, other than the interaction may be described by the usual momentum exchange coefficients, σ and σ' (Ref. 5); and in fact, these reflection coefficients, as well as the satellite surface temperature, may be regarded as variables over the exposed body surface.

As in the case of any aerodynamic configuration, the aerodynamic design of a satellite must consider the external shape and surface conduction of the vehicle as well as the internal mass distribution, or inertia

Manuscript released by the author February 1961 for publication as a WADD Technical Report.

characteristics. This, of course, means that certain design compromises are inevitable among the various devices aboard the vehicle; e g., solar "paddles" may not be compatible with efficient aerodynamic design. Nevertheless, feasibility studies of satellite aerodynamic stabilization must be kept elementary and uncluttered. It is for this reason that the discussion in this report is primarily concerned with simple, aerodynamic configurations. These basic designs, however, are certainly no more idealized than the classic "dumbbell" satellite used in gravity gradient studies.

Although this study is primarily concerned with the pitch stability and orientation of specific satellite configurations, aerodynamic force and moment equations are presented (Refs. 4, 6) which may be utilized for calculating aerodynamic coefficients, both static and dynamic, of other convex body shapes not treated herein. In addition, the basic free-molecule force and moment equations are amenable to the calculation of the effects of solar pressure, as illustrated in Appendix A of this report.

1. REVIEW OF FREE-MOLECULE AERODYNAMICS

1.1 Introduction

The purpose of this section is to review, without elaboration, the nomenclature and equations which are frequently referenced throughout this volume. Most of this material has been presented extensively in the open literature, and consequently, original sources and/or more detailed analyses will be cited whenever possible.

1.2 Shear and Pressure Coefficients

For a surface element exposed to a free-molecular stream, the impinging molecules do not strike the rebounding molecules near the surface with sufficient frequency to vary the incident momentum and energy. This hypothesis therefore permits separation of the incident momentum flux from the momentum flux due to the reflected or re-emitted molecules. Using the standard approximations for a molecular stream in Maxwellian equilibrium, the surface tangential (shear) and normal (pressure) components of the incident momentum flux per unit area may be written as (Refs. 1 through 5, e.g.)

$$\tau_i = \frac{1}{2} \rho_\infty V_\infty^2 \frac{S_N S_T}{S_\infty^2} \left\{ \frac{e^{-S_N^2}}{S_N \sqrt{\pi}} + [1 + \text{erf } S_N] \right\} \quad (1)$$

$$p_i = \frac{1}{2} \rho_\infty V_\infty^2 \left(\frac{S_N}{S_\infty} \right)^2 \left\{ \frac{e^{-S_N^2}}{S_N \sqrt{\pi}} + \left[1 + \frac{1}{2S_N^2} \right] [1 + \text{erf } S_N] \right\} \quad (2)$$

where S_N and S_T are respectively the normal and tangential components of the free-stream molecular speed ratio S_∞ .

The incident pressure and shear stresses determined above must now be combined with the contributions of the reflected molecules to give the total free-molecule stresses. The conventional (but not universal)

¹Because of the empirical nature of the analysis to follow, a discussion of the conceptual difference between "reflection" and "re-emission" is not warranted.

practice is to relate the reflected shear and pressure stresses to the incident stresses by the empirical reflection coefficients σ and σ' (Refs. 1, 2 and 5). These coefficients describe the amount of momentum transferred to the body surface in terms of departures from completely diffuse reflection. At this extreme, the molecules are assumed reflected with Maxwellian random motion corresponding to the surface temperature. At the other extreme, the incident molecules are assumed to be specularly reflected with the normal component of velocity unchanged in magnitude but reversed in direction. Then, by using these extremes, the reflection coefficients are defined by (Ref. 1, e.g.)

$$\sigma \equiv \frac{\tau_i - \tau_r}{\tau_i - \tau_d} \quad (3)$$

$$\sigma' \equiv \frac{p_i - p_r}{p_i - p_d} \quad (4)$$

where the subscript r refers to the actual stress due to the reflected molecules, and where the subscript d refers to the value of the reflected stress due to wholly diffuse reflection. Then when $\sigma = \sigma' = 1$ the reflection is diffuse, and when $\sigma = \sigma' = 0$, the reflection is specular. The portion of the shear stress due to diffuse reflection (τ_d), however, is identically zero since there is no preferred tangential direction for molecules reflected diffusely. On the other hand, the diffuse pressure term p_d has a non-zero value and has been derived as (Refs. 1 and 3)

$$p_d = \frac{1}{2} \rho_\infty V_\infty^2 \left(\frac{S_N}{S_\infty} \right) \frac{\sqrt{\pi}}{2 S_\infty} \sqrt{\frac{T_w}{T_\infty}} \left\{ \frac{e^{-S_N^2}}{S_N \sqrt{\pi}} + [1 + \operatorname{erf} S_N] \right\} \quad (5)$$

where T_w and T_∞ are respectively the surface and free stream temperatures.

By combining Eqs. (1) through (5), it is easily shown that the total shear and pressure coefficients are

$$C_T \equiv \frac{\tau}{\frac{1}{2} \rho_\infty V_\infty^2} = C_{\tau_i} - C_{\tau_r} = \sigma C_{\tau_i} \quad (6)$$

$$C_p = \sigma \frac{S_N S_T}{S_\infty^2} \left\{ \frac{e^{-S_N^2}}{S_N \sqrt{\pi}} + [1 + \operatorname{erf} S_N] \right\}$$

$$C_p \equiv \frac{P}{\frac{1}{2} \rho_{\infty} V_{\infty}^2} = C_{p_i} + C_{p_r} = (2-\sigma') C_{p_i} + \sigma' C_{p_d}$$

$$C_p = \frac{1}{S_{\infty}^2} \left\{ \left[\frac{2-\sigma'}{\sqrt{\pi}} S_N + \frac{\sigma'}{2} \sqrt{\frac{T_w}{T_{\infty}}} \right] e^{-S_N^2} + \left[(2-\sigma') \left(S_N^2 + \frac{1}{2} \right) + \frac{\sigma'}{2} \sqrt{\frac{T_w}{T_{\infty}}} \sqrt{\frac{T_w}{T_{\infty}}} S_N \right] (1 - \text{erf } S_N) \right\} \quad (7)$$

By the method of Reference 4 or 6, the Gaussian error function in the foregoing equations may be rearranged and integrated by parts to give

$$\text{erf}(S_N) \equiv \frac{2}{\sqrt{\pi}} \int_0^{S_N} e^{-t^2} dt = 1 - \frac{e^{-S_N^2}}{S_N \sqrt{\pi}} + \frac{1}{\sqrt{\pi}} \int_{S_N}^{\infty} e^{-t^2} \frac{dt}{t^2} \quad (8)$$

where the last term may now be regarded as a small remainder of a two-term approximation. For a surface element exposed to the free-stream flow, substitution of Eq. (18) into Eqs. (6) and (7) yields

$$C_T = 2\sigma \frac{S_T}{S_N} \left(\frac{S_N}{S_{\infty}} \right)^2 \left[1 + \frac{1}{2} \epsilon(S_N) \right] \quad (9)$$

$$C_p = \left\{ 2(2-\sigma') \left(\frac{S_N}{S_{\infty}} \right)^2 + \frac{\sigma' \sqrt{\pi}}{S_{\infty}} \sqrt{\frac{T_w}{T_{\infty}}} \left(\frac{S_N}{S_{\infty}} \right) + \frac{2-\sigma'}{S_{\infty}^2} \right\} \left[1 + \frac{1}{2} \epsilon(S_N) \right] - \frac{(2-\sigma')}{2\sqrt{\pi}} \frac{e^{-S_N^2}}{S_N S_{\infty}^2} \quad (10)$$

where, for S_N greater than unity,

$$\epsilon(S_N) \equiv \frac{1}{\sqrt{\pi}} \int_{S_N}^{\infty} e^{-t^2} \frac{dt}{t^2} = O\left(\frac{e^{-S_N^2}}{2\sqrt{\pi} S_N^3}\right) \ll 1 \quad (11)$$

For a surface element shielded from the free-stream, S_N and S_T may be considered negative and Eqs. (6) and (7) become

$$C_{\gamma_s} = -\sigma \frac{S_T}{S_N} \left(\frac{S_N}{S_\infty}\right)^2 \epsilon(S_N) \quad (12)$$

$$C_{P_s} = -\left\{ 2(2-\sigma') \left(\frac{S_N}{S_\infty}\right)^2 - \frac{\sigma' \sqrt{\pi}}{S_\infty} \sqrt{\frac{T_w}{T_\infty}} \left(\frac{S_N}{S_\infty}\right) + \frac{2-\sigma'}{S_\infty^2} \right\} \frac{\epsilon(S_N)}{2} + \frac{2-\sigma'}{2\sqrt{\pi}} \frac{e^{-S_N^2}}{S_N S_\infty^2} \quad (13)$$

where it should be noted that

$$\operatorname{erf}(-x) = -\operatorname{erf}(x) .$$

If the order of magnitude of Eq. (11) is utilized, then Eqs. (9) and (10) are approximately (Ref. 6),

$$C_\gamma \cong 2\sigma \frac{S_T}{S_N} \left(\frac{S_N}{S_\infty}\right)^2 \quad (14)$$

$$C_P \cong 2(2-\sigma') \left(\frac{S_N}{S_\infty}\right)^2 + \frac{\sigma' \sqrt{\pi}}{S_\infty} \sqrt{\frac{T_w}{T_\infty}} \left(\frac{S_N}{S_\infty}\right) + \frac{2-\sigma'}{S_\infty^2} . \quad (15)$$

Likewise for the shielded or shadowed element,

$$C_{\gamma_s} \cong 0 \quad (16)$$

$$C_{P_s} \cong 0 . \quad (17)$$

Eqs. (14) through (17) are based on the former restriction that $|S_N| \geq 1$ at every point on the body. For most applications, however, it is sufficiently accurate to assume that the foregoing equations are valid for the mean S_N on the body greater than unity.

1.3 Force and Moment Equations

Force and pitching moment integrals may now be formulated using the stress coefficients obtained above. Referring to Fig. 1, it is not difficult to show that the drag, lift and pitching moment coefficients for a surface element are (Ref. 4)

$$C_D = \frac{1}{S_A} \int_{\text{SURF}} \left\{ \left[C_P - \frac{S_N}{S_T} C_T \right] [(\vec{N} \cdot \vec{i}) \cos \alpha - (\vec{N} \cdot \vec{k}) \sin \alpha] + \frac{S_m}{S_T} C_T \right\} dA$$

$$C_L = \frac{1}{S_T} \int_{\text{SURF}} \left\{ \left[C_P - \frac{S_N}{S_T} C_T \right] [(\vec{N} \cdot \vec{i}) \sin \alpha - (\vec{N} \cdot \vec{k}) \cos \alpha] \right\} dA \quad (18)$$

$$C_m = \frac{1}{S_T \bar{c}} \int_{\text{SURF}} \left\{ \left[C_P - \frac{S_N}{S_T} C_T \right] [(\vec{j} \times \vec{Q}) \cdot \vec{n}] + \frac{S_m}{S_T} C_T [(\vec{j} \times \vec{Q}) \cdot \frac{\vec{S}_m}{S_m}] \right\} dA$$

where S_A and \bar{c} are the reference area and length respectively. For an arbitrary body of revolution, it is elementary to show that

$$\vec{Q} = -(x - x_{cm}) \vec{i} - r \sin \theta \vec{j} + r \cos \theta \vec{k}$$

$$\vec{N} = \frac{1}{\sqrt{1+r'^2}} \left\{ -r' \vec{i} + \sin \theta \vec{j} - \cos \theta \vec{k} \right\} \quad (19)$$

$$\frac{\vec{S}_m}{S_m} = -\cos \alpha \vec{i} - \sin \alpha \vec{k}$$

$$dA = r \sqrt{1+r'^2} dx d\theta$$

where $r' = dr/dx$ and the normal vector \bar{N} is always directed inward (convex body). The substitution of Eqs. (19) into Eqs. (18) yields the following general expressions for the force and moment coefficients for a body of revolution:

$$C_D = \frac{1}{S_T} \int_{\text{SURF}} \left\{ \left[C_P - \frac{S_N}{S_T} C_T \right] \left[r' \cos \alpha + \sin \alpha \cos \beta \right] + C_T \frac{S_m}{S_T} \sqrt{1+r'^2} \right\} r dx d\beta$$

$$C_L = \frac{1}{S_T} \int_{\text{SURF}} \left\{ \left[C_P - \frac{S_N}{S_T} C_T \right] \left[-r' \sin \alpha + \cos \alpha \cos \beta \right] \right\} r dx d\beta \quad (20)$$

$$C_m = -\frac{1}{S_T \bar{c}} \int_{\text{SURF}} \left\{ \left[C_P - \frac{S_N}{S_T} C_T \right] \left[r r' + x - x_{cm} \right] \cos \beta \right. \\ \left. + C_T \frac{S_m}{S_T} \sqrt{1+r'^2} \left[r \cos \beta \cos \alpha + (x - x_{cm}) \sin \alpha \right] \right\} r dx d\beta.$$

These expressions become, upon substitution of the approximate stress coefficients,

$$C_D \cong \frac{1}{S_T} \int_{\text{SURF}} \left\{ \left[2(2-\sigma-\sigma') \left(\frac{S_N}{S_m} \right)^2 + \frac{\sigma' \sqrt{\pi}}{S_m} \sqrt{\frac{T_m}{T_\infty}} \left(\frac{S_N}{S_m} \right) \right. \right. \\ \left. \left. + \frac{2-\sigma'}{S_m} \right] \left[r' \cos \alpha + \sin \alpha \cos \beta \right] + 2\sigma' \left(\frac{S_N}{S_m} \right) \sqrt{1+r'^2} \right\} r dx d\beta \quad (21)$$

$$C_L \cong \frac{1}{S_T} \int_{\text{SURF}} \left\{ \left[2(2-\sigma-\sigma') \left(\frac{S_N}{S_m} \right)^2 + \frac{\sigma' \sqrt{\pi}}{S_m} \sqrt{\frac{T_m}{T_\infty}} \left(\frac{S_N}{S_m} \right) \right. \right. \\ \left. \left. + \frac{2-\sigma'}{S_m} \right] \left[-r' \sin \alpha + \cos \alpha \cos \beta \right] \right\} r dx d\beta$$

$$C_m \approx -\frac{1}{S_\infty \bar{c}} \left\{ \int_{\text{SURF}} \left[\lambda (2 - \sigma - \sigma') \left(\frac{S_N}{S_\infty} \right)^2 + \frac{\sigma' \sqrt{\pi}}{S_\infty} \sqrt{\frac{I_{zz}}{I_{xx}}} \left(\frac{S_N}{S_\infty} \right) + \frac{2 - \sigma'}{S_\infty} \right] [rr' + x - x_{cm}] \cos \vartheta \right. \\ \left. + 2\sigma \sqrt{1+r'^2} \left(\frac{S_N}{S_\infty} \right) [r \cos \vartheta \cos \alpha + (x - x_{cm}) \sin \alpha] \right\} r dx d\vartheta \quad (21) \\ (\text{cont.})$$

where the integration now applies only on the portion of the body exposed to the incident molecular stream. Referring to Fig. 1 and Eqs. (19), it may be seen that for the steady state case,

$$\frac{S_N}{S_\infty} = \vec{N} \cdot \frac{\vec{S}_\infty}{S_\infty} = \frac{1}{\sqrt{1+r'^2}} [r' \cos \alpha + \sin \alpha \cos \vartheta] \quad (22)$$

In a similar manner, the incremental velocity distribution can be found for a body pitching about its center of mass; i.e.,

$$\Delta \frac{S_N}{S_\infty} = \frac{q \cos \vartheta}{V_\infty \sqrt{1+r'^2}} [rr' + x - x_{cm}] \quad (23)$$

where q is the pitch rate. The effective normal component of the molecular speed ratio is then

$$\left(\frac{S_N}{S_\infty} \right)_{\text{eff}} = \frac{1}{\sqrt{1+r'^2}} \left\{ r' \cos \alpha + \sin \alpha \cos \vartheta + \left(\frac{q \bar{c}}{2V_\infty} \right) \lambda \left[\frac{rr' + x - x_{cm}}{\bar{c}} \right] \cos \vartheta \right\} \quad (24)$$

where $q \bar{c} / 2V_\infty$ is the conventional non-dimensional pitch rate.

The approximate static force and moment coefficients for an arbitrary body of revolution are found by substituting Eq. (22) into Eqs. (21). The result is

$$\begin{aligned}
 C_D &\equiv \frac{2}{S_\pi} \int_0^{d_m} \int_0^{\hat{\ell}} \left\{ \frac{2(2-\sigma-\sigma')}{1+r^2} \left[r' \cos \alpha + \sin \alpha \cos \beta \right]^2 \right. \\
 &\quad \left. + \frac{\sigma' \sqrt{\pi}}{S_\omega \sqrt{1+r^2}} \sqrt{\frac{\Gamma_w}{T_\omega}} \left[r' \cos \alpha + \sin \alpha \cos \beta \right] + \frac{2-\sigma'}{S_\omega^2} \right. \\
 &\quad \left. + 2\sigma' \right\} r' \cos \alpha + \sin \alpha \cos \beta \Big\} r dx d\beta \\
 C_L &\equiv \frac{2}{S_\pi} \int_0^{d_m} \int_0^{\hat{\ell}} \left\{ \frac{2(2-\sigma-\sigma')}{1+r^2} \left[r' \cos \alpha + \sin \alpha \cos \beta \right]^2 \right. \\
 &\quad \left. + \frac{\sigma' \sqrt{\pi}}{S_\omega \sqrt{1+r^2}} \sqrt{\frac{\Gamma_w}{T_\omega}} \left[r' \cos \alpha + \sin \alpha \cos \beta \right] \right. \\
 &\quad \left. + \frac{2-\sigma'}{S_\omega^2} \right\} \left\{ -r' \sin \alpha + \cos \alpha \cos \beta \right\} r dx d\beta \\
 C_m &\equiv \frac{-2}{S_\pi \bar{c}} \int_0^{d_m} \int_0^{\hat{\ell}} \left\{ \frac{2(2-\sigma-\sigma')}{1+r^2} \left[r' \cos \alpha + \sin \alpha \cos \beta \right]^2 + \frac{\sigma' \sqrt{\pi}}{S_\omega \sqrt{1+r^2}} \sqrt{\frac{\Gamma_w}{T_\omega}} \left[r' \cos \alpha + \sin \alpha \cos \beta \right] \right. \\
 &\quad \left. + \frac{2-\sigma'}{S_\omega^2} \right\} \left\{ r r' + x - x_{cm} \right\} \cos \beta \\
 &\quad \left. + 2\sigma' \left\{ r' \cos \alpha + \sin \alpha \cos \beta \right\} \left\{ r \cos \alpha \cos \beta + (x - x_{cm}) \sin \alpha \right\} \right\} r dx d\beta
 \end{aligned} \tag{25}$$

where $\hat{\ell}$ is the body length¹ and where

$$\begin{aligned}
 d_m &= \cos^{-1}(-r'/\tan \alpha) \quad \text{for } r' \leq |\tan \alpha| \\
 &= \pi \quad \text{for } r' \geq |\tan \alpha|.
 \end{aligned}$$

¹For integration purposes, x is now being defined as positive aft of the nose.

An aerodynamic parameter frequently utilized is the static pitching moment coefficient slope at zero angle of attack. For bodies of revolution with $r' > 0$, the derivative of the third of Eqs. (25) yields

$$C_{m_\alpha} \equiv \left[\frac{\partial C_m}{\partial \alpha} \right]_{\substack{\alpha \rightarrow 0 \\ q \rightarrow 0}} \cong -\frac{2\pi}{S\pi c} \int_0^l \left\{ \left[\frac{2(2-\sigma-\sigma')}{1+r'^2} + \frac{\sigma' \sqrt{\pi}}{2S_\infty \sqrt{1+r'^2}} \sqrt{\frac{T_w}{T_\infty}} \right] [rr' + x - x_{cm}] \right. \\ \left. + \sigma [r + 2r'(x - x_{cm})] \right\} r dx \quad (26)$$

where σ , σ' and T_w are taken to be independent of the azimuth angle δ . The damping in pitch derivative C_{m_q} may be found by differentiating the third of Eqs. (21) with respect to $q\bar{c}/2V_\infty$ while using Eq. (24); i.e.,

$$C_{m_q} \equiv \frac{\partial C_m}{\partial \left(\frac{q\bar{c}}{2V_\infty} \right)} \cong -\frac{4}{S\pi c^2} \int_0^l \int_0^\delta \left\{ \left[\frac{2(2-\sigma-\sigma')}{1+r'^2} \right] [r' \cos \alpha + \left(\sin \alpha + \frac{\sigma}{V_\infty} (rr' + x - x_{cm}) \right) \cos \delta] \right. \\ \left. + \frac{\sigma' \sqrt{\pi}}{S_\infty \sqrt{1+r'^2}} \sqrt{\frac{T_w}{T_\infty}} \right\} [rr' + x - x_{cm}] \cos \delta \\ + 2\sigma \left\{ r \cos \alpha \cos \delta + (x - x_{cm}) \sin \alpha \right\} \left. \right\} [rr' + x - x_{cm}] \cos \delta r dx d\delta \quad (27)$$

which becomes for $\alpha = 0$, $r' > 0$, and $q \rightarrow 0$,

$$C_{m_q} \Big|_{\substack{q \rightarrow 0 \\ \alpha = 0}} \cong -\frac{4\pi}{S\pi c^2} \int_0^l \left\{ \left[\frac{2(2-\sigma-\sigma')}{1+r'^2} r' + \frac{\sigma' \sqrt{\pi}}{2S_\infty \sqrt{1+r'^2}} \sqrt{\frac{T_w}{T_\infty}} \right] [rr' + x - x_{cm}] \right. \\ \left. + \sigma r \right\} [rr' + x - x_{cm}] r dx \quad (28)$$

The foregoing integrals, Eqs. (16), (19), (25, through (28), will be useful in the drag and moment analyses to follow. When possible, the basic Eqs. (18) and (20) will be solved using the exact shear and pressure coefficients Eqs. (6) and (7). For most applications, however, the approximate Eqs. (25) through (27) will satisfy the accuracy requirements.

2. DRAG ANALYSIS

2.1 Introduction

In the expressions for satellite lifetime and atmosphere influence on orbital elements, the well-known ballistic coefficient, $C_D S_{\pi} / 2m$, inherently appears¹. The problem of evaluating the coefficient may be phrased two ways: if the drag coefficient, C_D , is based on a fixed reference area, S_{π} , then C_D is a strong function of the attitude of the satellite; alternately, if an average C_D is assumed for all satellite attitudes, then the proper reference area becomes variable. It is this latter approach which is more commonly taken. That is, let S_{π} equal the projected frontal area of the satellite (normal to free-stream), and then assume a constant C_D which is based on this frontal area. The discussion in this section is concerned with the verification or nullification of this assumption. Three practical configurations - cylinder, cone and sphere - are considered along with the "academic" flat plate.

All free-molecule drag coefficients are calculated using the exact methods when possible. The approximate method of Ref. 6, which is outlined in Section 1, is used for comparisons or when the exact expressions are not integrable. The reflection coefficients, G and G' , as well as the surface temperature T_w are assumed constant over the body surface. If the free stream temperature T_{∞} is taken from the A/GC 1959 Model Atmosphere (Ref. 7), and if the relative velocity is assumed to be approximately the inertial velocity, then the variation of the speed ratio S_{∞} with altitude for nearly circular orbits may be calculated. This variation of S_{∞} , along with a curve of $(1/S_{\infty}) \sqrt{T_w/T_{\infty}}$ for $T_w = 550^{\circ}\text{R}$,² are shown in Fig. 2 and are used in the drag analyses to follow.

2.2 Cylinder

The cylinder drag coefficient must be divided into two parts: that due to the blunt ends and that due to the cylindrical surface. The corresponding frontal areas are

$$\begin{aligned} S_{\text{END}}^* &= \pi R^2 \cos \alpha \\ S_{\text{CYL}}^* &= 2Rl \sin \alpha \\ S_{\pi} &= S_{\text{TOTAL}}^* = \pi R^2 \left[\cos \alpha + \frac{4(l/R)}{\pi} \sin \alpha \right] \end{aligned} \quad (29)$$

¹ See Appendix C of Volume I of this series of reports.

² Gustafson (Ref. 20) also assumes $T_w = 550^{\circ}\text{R}$.

where all starred symbols will now refer to the frontal area system. The free-molecule drag coefficient of the combined flat nose and base is the same as a flat plate at angle of attack. This result may be found as (Ref. 2 or 4)

$$C_{D_{EMOS}}^* = \frac{1}{\cos \alpha + \frac{a(\ell/D)\sin \alpha}{\pi}} \left\{ \frac{\sigma^1 \sqrt{\pi} \cos^2 \alpha}{S_{\infty}} \sqrt{\frac{T_w}{T_{\infty}}} + \frac{Z}{S_{\infty} \sqrt{\pi}} \left[\sigma + \cos^2 \alpha (2 - \sigma - \sigma^1) \right] e^{-S_{\infty}^2 \cos^2 \alpha} + \cos \alpha \left[2\sigma + \frac{Z - \sigma^1}{S_{\infty}} + 2 \cos^2 \alpha (2 - \sigma - \sigma^1) \right] \text{erf}(S_{\infty} \cos \alpha) \right\} \quad (30)$$

where the third of Eqs. (29) is used for the reference area. The free molecule drag coefficient of the cylindrical portion may be formulated in a similar manner except that the integrations are more tedious. The exact expression has been obtained by Talbot (Ref. 8). The result is,

$$C_{D_{Cyl}}^* = \frac{\sin \alpha}{\sin \alpha + \frac{\pi}{4(\ell/D)} \cos \alpha} \left\{ \left[(4 - 2\sigma^1 + \sigma) F(\xi) - \sigma G(\xi) \right] \sin^2 \alpha \cdot \frac{\sigma^1 \sqrt{\pi}^{3/4}}{4 S_{\infty}} \sqrt{\frac{T_w}{T_{\infty}}} \sin d + \sigma G(\xi) \right\} \quad (31)$$

where $\xi \equiv S_{\infty} \sin \alpha$, and where

$$F(\xi) \equiv \sqrt{\pi} e^{-\xi^2/2} \left\{ \left(\frac{\xi}{3} + \frac{1}{2\xi} \right) I_0 \left(\frac{\xi^2}{2} \right) + \left(\frac{\xi}{3} + \frac{1}{6\xi} \right) I_1 \left(\frac{\xi^2}{2} \right) \right\} \quad (32)$$

$$G(\xi) \equiv \sqrt{\pi} e^{-\xi^2/2} \left\{ \left(\xi + \frac{1}{\xi} \right) I_0 \left(\frac{\xi^2}{2} \right) + \xi I_1 \left(\frac{\xi^2}{2} \right) \right\}$$

If diffuse molecular reflection is assumed, then $\sigma = \sigma^1 = 1.0$ and Eqs. (30) and (31) may be combined and simplified to yield the total drag coefficient.

$$C_{D_{TOTAL}}^* = \frac{1}{\sin \alpha + \frac{\pi}{4(\ell/D)} \cos \alpha} \left\{ \frac{\pi^{3/2}}{4 S_{\infty}} \sqrt{\frac{T_w}{T_{\infty}}} \left(\frac{\cos^2 \alpha}{\ell/D} + \sin^2 \alpha \right) + \frac{\sqrt{\pi}}{2 S_{\infty} (\ell/D)} e^{-S_{\infty}^2 \cos^2 \alpha} + \left(2 + \frac{1}{S_{\infty}} \right) \frac{\pi \cos \alpha}{4(\ell/D)} \text{erf}(S_{\infty} \cos \alpha) + \left[3F(\xi) - G(\xi) \right] \sin^2 \alpha + G(\xi) \sin d \right\} \quad (33)$$

For $\alpha = 0$, $[3F(\alpha) - G(\alpha)] \sin^2 \alpha \rightarrow 0$, $G(\alpha) \sin \alpha \rightarrow \sqrt{\pi}/S_\infty$ and Eq. (33) becomes

$$C_{D\alpha=0}^* = \frac{\sqrt{\pi}}{S_\infty} \sqrt{\frac{T_w}{T_\infty}} + \frac{2}{\sqrt{\pi} S_\infty} e^{-S_\infty^2} + \left(2 + \frac{1}{S_\infty^2}\right) \text{erf}(S_\infty) + \frac{4(l/D)}{\sqrt{\pi} S_\infty} \quad (34)$$

Now for near-Earth orbits, S_∞ is always in excess of 5.0; therefore, $e^{-S_\infty^2} \rightarrow 0$ and $\text{erf}(S_\infty) \rightarrow 1.0$, and

$$C_{D\alpha=0}^* \cong \frac{\sqrt{\pi}}{S_\infty} \sqrt{\frac{T_w}{T_\infty}} + 2 + \frac{1}{S_\infty^2} + \frac{4(l/D)}{\sqrt{\pi} S_\infty} \quad (35)$$

which is slightly greater than 2 for small l/D . For large l/D , however, the cylinder "skin friction" term $4(l/D)/\sqrt{\pi} S_\infty$ may be dominant. It should be noted that the approximate theory of Ref. 6 is not applicable for this $\alpha = 0$ case since S_w on the cylindrical portion is zero. The first three terms of Eq. (35), however, are due to the blunt nose and would be obtained from the approximate theory.

At another extreme, $\alpha = \pi/2$, the reference area becomes lD and Eq. (33) reduces to

$$C_{D\alpha=\pi/2}^* = \frac{\pi^{3/2}}{4 S_\infty} \sqrt{\frac{T_w}{T_\infty}} + \frac{\sqrt{\pi}}{2(l/D) S_\infty} + 3F(S_\infty) \quad (36)$$

This equation may also be simplified for large S_∞ since it can be shown that $F(S_\infty) \rightarrow 2/3$; i.e.,

$$C_{D\alpha=\pi/2}^* \cong \frac{\pi^{3/2}}{4 S_\infty} \sqrt{\frac{T_w}{T_\infty}} + \frac{\sqrt{\pi}}{2(l/D) S_\infty} + 2 \quad (37)$$

which is seen to be near 2 for all reasonable l/D and S_∞ . Consequently, for large l/D , $C_{D\alpha=0}^*$ at angles of attack of zero and 90° may be considerably different.

Eq. (33) may be solved for other values of angle of attack and fineness ratio. Several combinations, along with the approximate Eqs. (35) and (37), are shown in Fig. 3 for C_D^* versus S_∞ . It is interesting to note from Fig. 3 that the minimum C_D^* of a cylinder occurs for some intermediate angle of attack.

2.3 Cone

Unfortunately, the exact free-molecule drag coefficient has not been explicitly determined for the case of a right circular cone at angle of attack. Nevertheless, numerical solutions have been obtained for inclined cones and are presented by Stalder and Zurick (ref. 9) for completely diffuse and completely specular reflection. For zero angle of attack, however, the first of Eqs. (20) is easily integrated to give the exact drag coefficient as

$$C_D^*_{\alpha=0} = \left\{ \frac{2-\sigma-\sigma'}{S_{\infty}\sqrt{\pi}} \sin\delta + \frac{\sigma}{S_{\infty}\sqrt{\pi} \sin\delta} + \frac{\sigma'}{2S_{\infty}^2} \left| \frac{\sqrt{T_w}}{T_{\infty}} \right. \right\} e^{-S_{\infty}^2 \sin^2\delta} \\ + \left\{ (2-\sigma-\sigma') \sin^2\delta + \frac{\sigma'\sqrt{\pi}}{2S_{\infty}} \left| \frac{\sqrt{T_w}}{T_{\infty}} \right. \sin\delta + \frac{2-\sigma'}{2S_{\infty}^2} + \sigma \right\} \left[1 + \operatorname{erf}(S_{\infty} \sin\delta) \right] \quad (38)$$

where δ is the cone semivertex angle and where the base contribution is neglected. For diffuse molecular reflection, $\sigma = \sigma' = 1.0$ and Eq. (38) reduces to

$$C_D^*_{\alpha=0} = \left\{ \frac{1}{S_{\infty}\sqrt{\pi} \sin\delta} + \frac{1}{2S_{\infty}^2} \left| \frac{\sqrt{T_w}}{T_{\infty}} \right. \right\} e^{-S_{\infty}^2 \sin^2\delta} \\ + \left\{ \frac{\sqrt{\pi}}{2S_{\infty}} \left| \frac{\sqrt{T_w}}{T_{\infty}} \right. \sin\delta + 1 + \frac{1}{2S_{\infty}^2} \right\} \left[1 + \operatorname{erf}(S_{\infty} \sin\delta) \right]. \quad (39)$$

As $S_{\infty} \sin\delta$ becomes larger than unity, the exponential and error function approach the limits zero and one respectively, as previously noted, and

$$C_D^*_{\alpha=0} \approx \frac{\sqrt{\pi}}{S_{\infty}} \left| \frac{\sqrt{T_w}}{T_{\infty}} \right. \sin\delta + 2 + \frac{1}{S_{\infty}^2} \quad (40)$$

which is the same as the solution of the first of Eqs. (25), for $\alpha = 0$. For very thin cones, Eq. (39) predicts free-molecule drag coefficients considerably higher than calculated by Eq. (40), as may be seen in Fig. 4.

For cones at angle of attack, the approximate theory outlined in Section 1.3 (or Ref. 6) may be conveniently utilized if the average S_N on the cone is greater than unity. This restriction may be expressed as

$$S_\infty > \frac{P(\zeta)}{h(\zeta)} \frac{1}{\cos \alpha \sin \delta}$$

where $\zeta \equiv \tan \delta / \tan \alpha$ and

$$h(\zeta) \equiv \frac{1}{\pi} \left\{ \cos^{-1}(-\zeta) + \frac{1}{\zeta} \sqrt{1-\zeta^2} \right\} \quad [\zeta \leq 1.0] \\ \equiv 1.0 \quad [\zeta \geq 1.0] \quad (4.1)$$

$$P(\zeta) \equiv \frac{1}{\pi} \left\{ \cos^{-1}(-\zeta) \right\} \quad [\zeta \leq 1.0] \\ \equiv 1.0 \quad [\zeta \geq 1.0] \quad (4.2)$$

Since the frontal area of the inclined cone must also be known, it is not difficult to show that

$$S_\pi = S_{\text{cone}}^* = \pi R^2 \cos \alpha h(\zeta) \quad (4.3)$$

where R is the radius of the base. The first of Eqs. (25) may be integrated and combined with Eqs. (4.3) to give

$$C_D^* \equiv 2(2-\sigma-\sigma') \sin^2 \delta \cos^2 \alpha \frac{f(\zeta)}{h(\zeta)} + \frac{\sigma' \pi}{S_\infty} \int_{T_\infty}^{\sqrt{\cdot}} \sin \delta \cos \alpha \frac{g(\zeta)}{h(\zeta)} (4.4) \\ + \frac{2-\sigma'}{S^2} + 2\sigma'$$

where

$$f(\epsilon) \equiv \frac{1}{\pi} \left\{ \left(1 + \frac{3}{2\epsilon^2} \right) \cos^{-1}(-\epsilon) + \frac{1}{\epsilon} \left(\frac{11}{6} + \frac{2}{3\epsilon^2} \right) \sqrt{1-\epsilon^2} \right\} \quad [\epsilon \leq 1.0] \\ \equiv 1 + \frac{3}{2\epsilon^2} \quad [\epsilon \geq 1.0] \quad (45)$$

$$g(\epsilon) \equiv \frac{1}{\pi} \left\{ \left(1 + \frac{1}{2\epsilon^2} \right) \cos^{-1}(-\epsilon) + \frac{3}{2\epsilon} \sqrt{1-\epsilon^2} \right\} \quad [\epsilon \leq 1.0] \\ \equiv 1 + \frac{1}{2\epsilon^2} \quad [\epsilon \geq 1.0] \quad (46)$$

Eq. (44) is also presented in Refs. 4 and 6¹ for the case of $S_{\pi} = \pi R^2$.

For diffuse reflection, Eq. (44) simplifies to,

$$C_D^* \cong \frac{\sqrt{\pi}}{S_{\infty}} \sqrt{\frac{T_w}{T_{\infty}}} \sin \delta \cos \alpha \frac{g(\epsilon)}{h(\epsilon)} + 2 + \frac{1}{S_{\infty}^2} \quad (47)$$

For $\alpha = \pi/2$,

$$\sin \delta \cos \alpha \frac{g(\epsilon)}{h(\epsilon)} \rightarrow \frac{\pi}{4} \cos \delta$$

and Eq. (47) becomes,

$$C_{D_{\alpha=\pi/2}}^* \cong \frac{\pi^{3/2} \cos \delta}{4 S_{\infty}} \sqrt{\frac{T_w}{T_{\infty}}} + 2 + \frac{1}{S_{\infty}^2} \quad (48)$$

Eqs. (39), (40), (47) and (48) are plotted in Fig. 4 for several angle of attack and cone angle combinations.

¹The last term of the cone C_D equation in Ref. 6 should be:

$$\left(\frac{2 - \sigma_w}{S_{\infty}^2} + 2 C_T \right) \cos \alpha h(\epsilon)$$

2.4 Sphere

The sphere is an extremely simple case to analyze since the frontal area remains constant regardless of angle of attack. The exact free-molecule drag coefficient for a sphere is written as (Ref. 1, 2 or 4)

$$C_D^* = (2 - \sigma' + \sigma') Q(S_\infty) + \frac{2\sigma' \sqrt{\pi}}{3 S_\infty} \sqrt{\frac{T_w}{T_\infty}} \quad (49)$$

where

$$Q(S_\infty) \equiv \frac{2S_\infty^3 + 1}{2\sqrt{\pi} S_\infty^2} e^{-S_\infty^2} + \frac{4S_\infty^4 + 4S_\infty^2 - 1}{4S_\infty^4} \operatorname{erf}(S_\infty) \quad (50)$$

Eq. (49) for diffuse reflection is obviously

$$C_D^* = 2Q(S_\infty) + \frac{2\sqrt{\pi}}{3 S_\infty} \sqrt{\frac{T_w}{T_\infty}} \quad (51)$$

The approximate drag coefficient of a complete sphere may be obtained by integrating the first of Eqs. (25) over the forward hemisphere; i.e.,

$$C_D^* \cong 2 + \frac{1}{S_\infty^2} + \frac{2\sqrt{\pi}}{3 S_\infty} \sqrt{\frac{T_w}{T_\infty}} \quad (52)$$

where the shadow area contributes very little to the total drag. The difference between these last two equations may be seen in Fig. 5. Here, again, the drag coefficient approaches the "Newtonian-diffuse" value of 2.

2.5 Flat Plate

The infinitely thin flat plate is difficult to analyze from the frontal area point-of-view since at zero angle of attack the area is zero while the drag is finite; i.e.,

$$C_{D_{\text{area}}}^* \rightarrow \infty$$

It is interesting, however, to calculate C_D^* for other angles of attack for comparison with the three-dimensional configurations. For arbitrary values of the reflection coefficients, the exact C_D^* may be expressed as

$$C_D^* = \frac{\sigma' \sqrt{\pi} \sin \alpha}{S_\infty} \sqrt{\frac{T_w}{T_a}} + \left\{ \frac{2\sigma}{\sqrt{\pi} S_\infty \sin \alpha} + \frac{2(2-\sigma-\sigma') \sin \alpha}{S_\infty \sqrt{\pi}} \right\} e^{-S_\infty^2 \sin^2 \alpha} + \left\{ 2\sigma + \frac{2-\sigma'}{S_\infty^2} \right\} + 2(2-\sigma-\sigma') \sin^2 \alpha \operatorname{erf}(S_\infty \sin \alpha) \quad (53)$$

which becomes for $\sigma = \sigma' = 1.0$,

$$C_D^* = \frac{\sqrt{\pi} \sin \alpha}{S_\infty} \sqrt{\frac{T_w}{T_a}} + \frac{2e^{-S_\infty^2 \sin^2 \alpha}}{\sqrt{\pi} S_\infty \sin \alpha} + \left(2 + \frac{1}{S_\infty^2} \right) \operatorname{erf}(S_\infty \sin \alpha) \quad (54)$$

and for $S_\infty \sin \alpha$ larger than unity,

$$C_D^* \approx \frac{\sqrt{\pi} \sin \alpha}{S_\infty} \sqrt{\frac{T_w}{T_a}} + 2 + \frac{1}{S_\infty^2} \quad (55)$$

A flat plate normal to the free-stream ($\alpha = 90^\circ$) has an exact diffuse drag coefficient of

$$C_D^*_{\alpha=90} = \frac{\sqrt{\pi}}{S_\infty} \sqrt{\frac{T_w}{T_a}} + \frac{2e^{-S_\infty^2}}{S_\infty \sqrt{\pi}} + \left(2 + \frac{1}{S_\infty^2} \right) \operatorname{erf}(S_\infty) \quad (56)$$

which approaches, for large speed ratios,

$$C_D^*_{\alpha=90} \approx \frac{\sqrt{\pi}}{S_\infty} \sqrt{\frac{T_w}{T_a}} + 2 + \frac{1}{S_\infty^2} \quad (57)$$

Eqs. (54) through (57) are plotted in Fig. 6 for several angles of attack. The deviations at small angle of attack, as for the case of the cylinder, are clearly seen.

2.6 Summary of Configurations

A comparison of diffuse, frontal drag coefficients for the cylinder, cone, sphere and flat plate is shown in Fig. 7. If only the three-dimensional shapes are considered, it may be seen that most of the drag coefficients lie in a $\pm 5\%$ band for all practical molecular speed ratios. A noteworthy exception is the cylinder near zero angle of attack. Then it may be concluded that the practice of assuming a constant drag coefficient per unit frontal area for a satellite at all altitudes is not, in general, correct, although for some shapes it may be an acceptable approximation. The problem of estimating the ballistic coefficients, therefore, appears to deserve additional study.

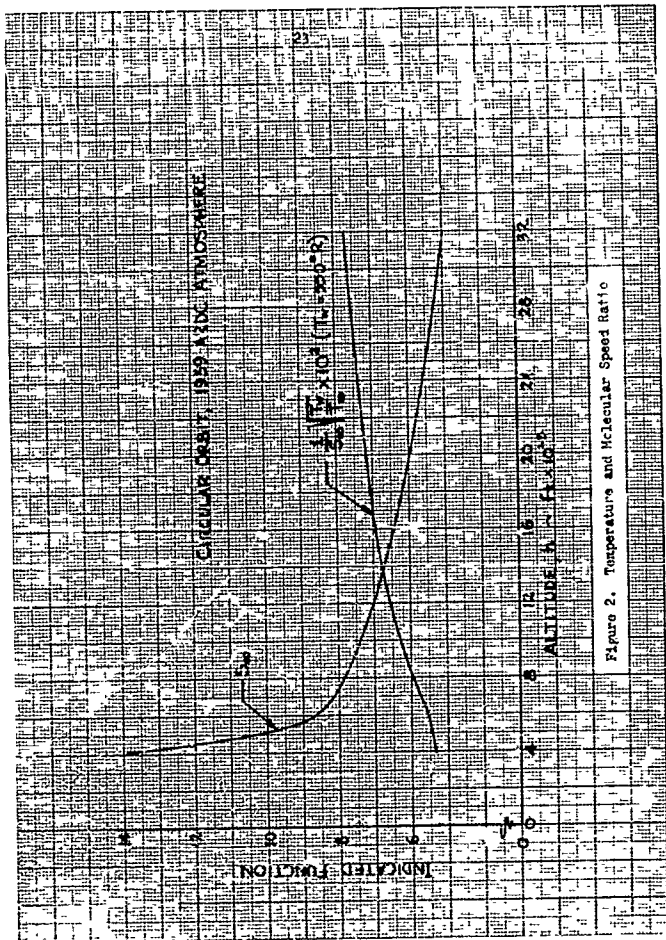
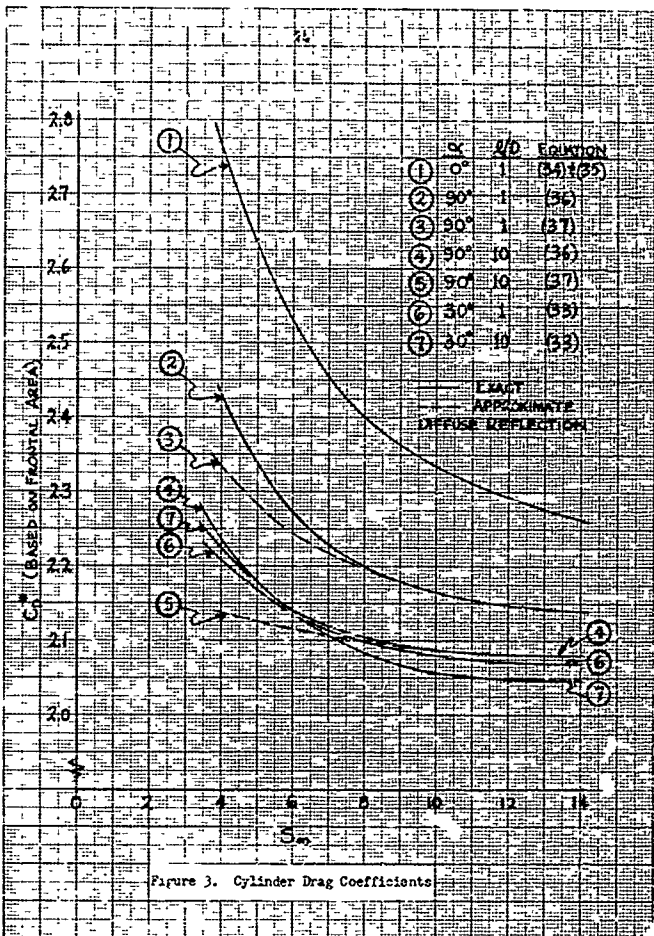
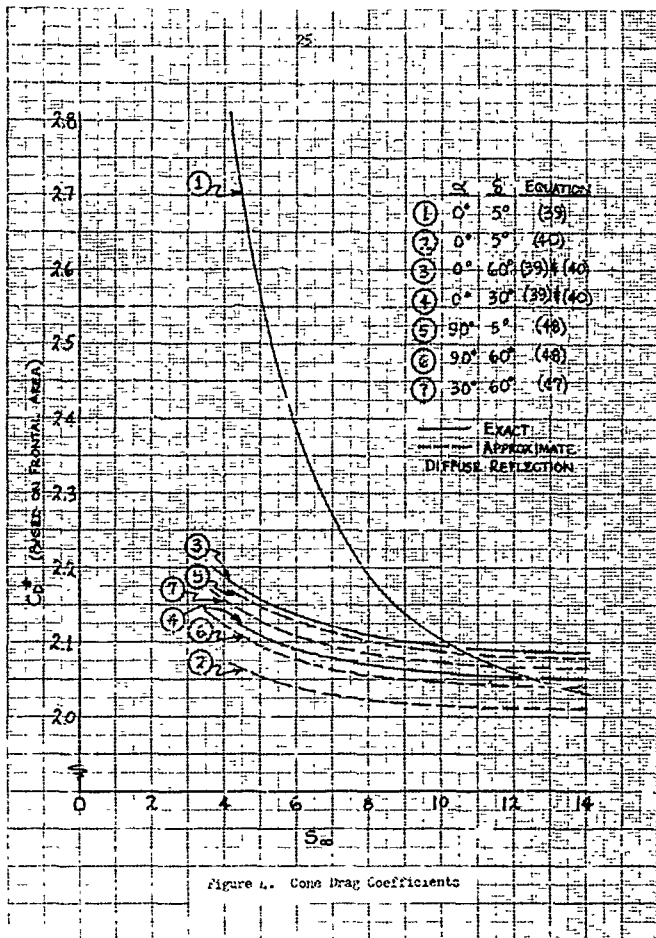
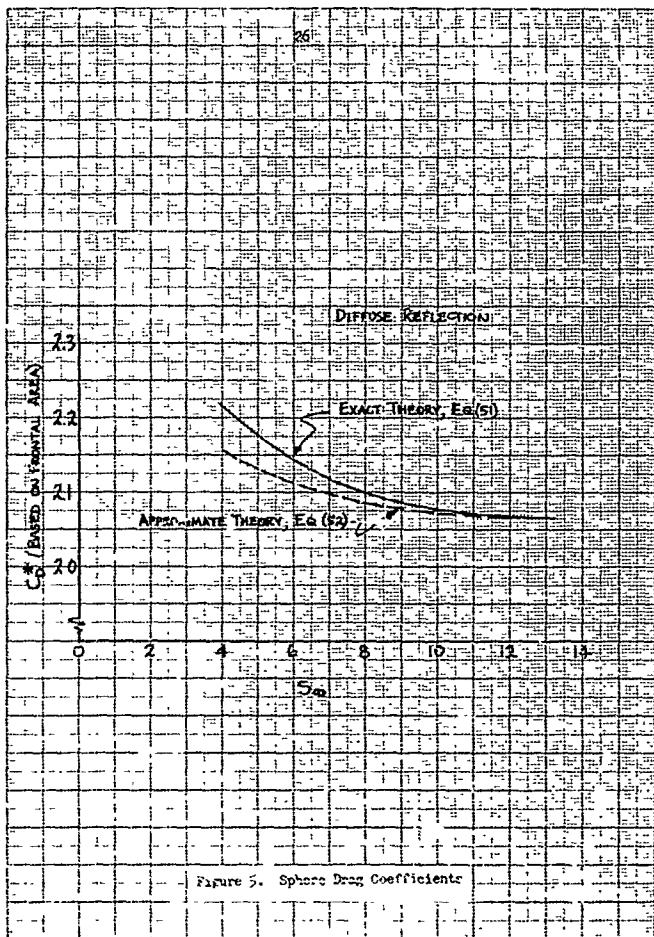
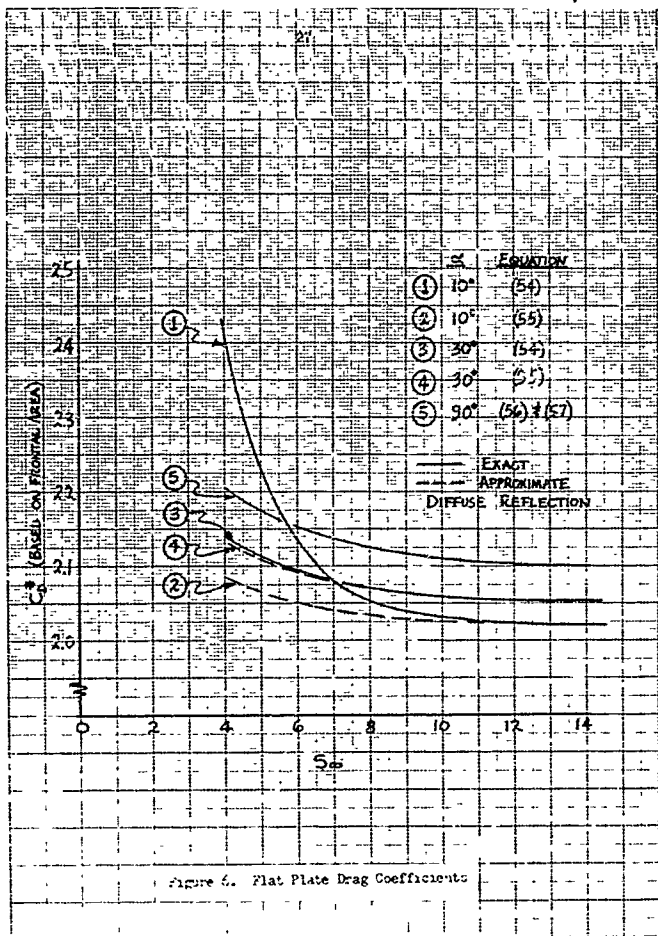


Figure 2. Temperature and Molecular Speed Ratio

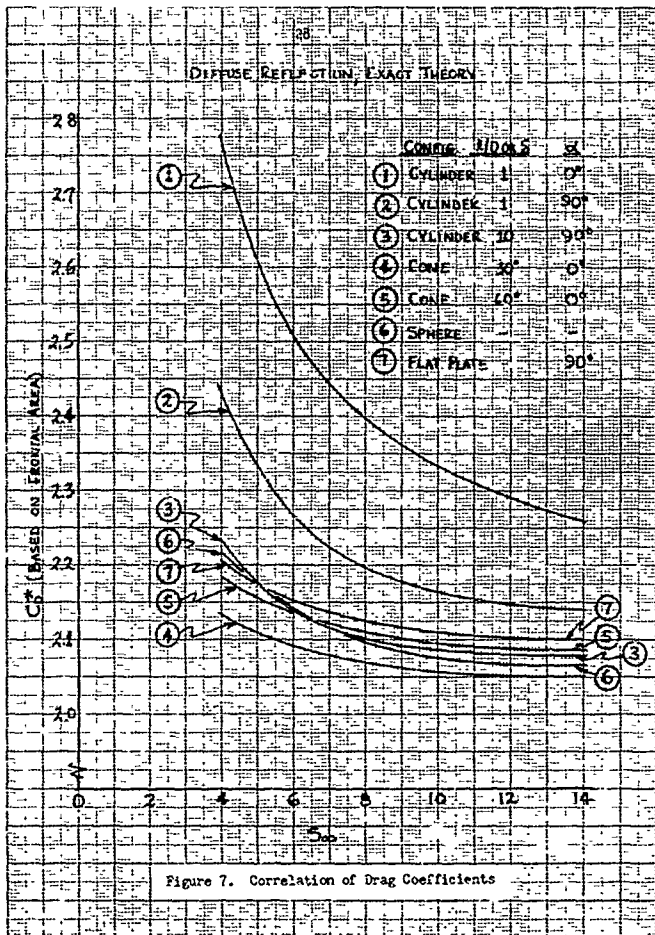








DIFFUSE REFLECTION - EXACT THEORY



2. STATIC STABILITY ANALYSIS3.1 General Considerations

As noted in Volume I of this series of reports, the aerodynamic contribution in the equations of satellite pitching motion may be conventionally represented by the leading terms of a Fourier series. For small angular deviations of the body from equilibrium, it may therefore be shown that the non-dimensional aerodynamic torque (or pitching moment coefficient) may be written approximately as

$$C_{m_q} = C_{m_\alpha} \cdot \alpha + C_{m_q} \left(\frac{q\bar{c}}{2V_\infty} \right) \quad (58)$$

where, in this analysis,

$$C_m \equiv \frac{L_A \gamma}{\frac{1}{2} \rho_\infty V_\infty^2 S_D \bar{c}}$$

$$C_{m_\alpha} \equiv \left[\frac{\partial C_m}{\partial \alpha} \right]_{\substack{\alpha \rightarrow 0 \\ q = 0}} \quad (59)$$

$$C_{m_q} \equiv \left[\frac{\partial C_m}{\partial \left(\frac{q\bar{c}}{2V_\infty} \right)} \right]_{\substack{q \rightarrow 0 \\ \alpha = 0}}$$

The discussions in this section are concerned only with the static pitching moments (i.e., C_m with $q = 0$) and the initial pitching moment slope C_{m_α} . The purpose of the first of these investigations, namely C_m versus a wide range of angle of attack, is to examine the validity of the linear C_m approximation for three simple configurations: the cylinder, sphere and cone. The analysis is subsequently extended to calculations of C_{m_α} for more complex configurations: power law bodies, truncated cones, cone-cylinders and sphere-capped cylinders. Supplemental equations and graphs are presented for the purpose of examining miscellaneous effects of surface temperature and reflection coefficient variations. The final portion of this section is concerned with the optimization of satellite geometry for maximum aerodynamic stability. The possible augmentation effects of gravitational torques, however, are not ignored.

3.2 Aerodynamic Pitching Moment

3.2.1 Introduction

With proper satellite design, numerical results of the motion analysis (Volume I) have shown that the small angle of attack approximation is generally justified. In order to avoid any unforeseen complications, however, it is advisable to examine the pitching characteristics beyond the small angle range. Accordingly, it is the purpose of this section to present curves of pitching moment coefficient versus angle of attack for the basic body shapes (cylinder, sphere and cone). Initial pitching moment slopes for these shapes are also presented along with the slopes for the more sophisticated shapes (power law bodies, truncated cones, hemisphere-cylinders and cone-cylinders).

All coefficients are referenced to the base diameter D and base area $\pi D^2/4$.

3.2.2 Pitching Moment of Basic Body Shapes

3.2.2.1 Cylinder

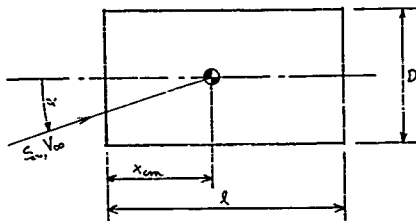


Figure 8. Cylinder Nomenclature

The pitching moment coefficient of a right circular cylinder may be calculated using the exact free molecule flow equations. For a cylinder without end effects, the last of Eqs. (20) integrates to give (Ref. 4)

$$C_{m_{cyl}} = -\frac{\lambda}{D} \left\{ \left[\frac{4}{\pi} (2 - \sigma' + \frac{\sigma}{2}) F(\xi) \sin^2 \alpha + \frac{\sigma' \sqrt{\pi}}{2 S_{\infty}} \sqrt{\frac{T_w}{T_{\infty}}} \sin \alpha \right] \frac{\lambda}{D} \left[1 - 2 \frac{X_{cm}}{\lambda} \right] + \frac{\sigma}{2} \sin 2\alpha \right\} \quad (60)$$

where $\xi \equiv S_{\infty} \sin \alpha$ and $F(\xi)$ is defined by the first of Eqs. (32). The nose contribution may be taken into account by considering a flat-plate normal to the stream. The exact moment contribution of this surface is due only to the tangential stresses and is given by

$$C_{m_{nose}} = \frac{\sigma}{S_{\infty}} \left\{ \frac{\sin \alpha}{\pi} e^{-S_{\infty}^2 \cos^2 \alpha} + \frac{S_{\infty}}{\lambda} \sin 2\alpha \left[1 + \operatorname{erf}(S_{\infty} \cos \alpha) \right] \right\} \frac{X_{cm}}{D} \quad (61)$$

It is noted that the nose contribution is positive and hence destabilizing. The base end effects, which are small, are not included in this analysis since the base will be assumed void for design purposes (see Section 3.4). Combining Eqs. (60) and (61), the total static pitching moment coefficient is

$$C_m = - \left\{ \left[\frac{4}{\pi} (2 - \sigma' + \frac{\sigma}{2}) F(\xi) \sin^2 \alpha + \frac{\sigma' \sqrt{\pi}}{2 S_{\infty}} \sqrt{\frac{T_w}{T_{\infty}}} \sin \alpha \right] \left(\frac{\lambda}{D} \right)^2 + \frac{\sigma}{2} \left(\frac{\lambda}{D} \right) \sin 2\alpha \right\} \left[1 - 2 \frac{X_{cm}}{\lambda} \right] + \frac{\sigma}{2} \left(\frac{\lambda}{D} \right) \left\{ \frac{2 \sin \alpha}{\pi S_{\infty}} e^{-S_{\infty}^2 \cos^2 \alpha} + \sin 2\alpha \left[\operatorname{erf}(S_{\infty} \cos \alpha) - 1 \right] \right\} \quad (62)$$

For diffuse molecular reflection, $\sigma = \sigma' = 1$, and Eq. (62) becomes

$$C_m = - \left(\frac{\lambda}{D} \right) \sin \alpha \left\{ \left[\frac{6}{\pi} F(\xi) \sin \alpha + \frac{\sqrt{\pi}}{2 S_{\infty}} \sqrt{\frac{T_w}{T_{\infty}}} \right] \frac{\lambda}{D} \cos \alpha \right\} \left[1 - 2 \frac{X_{cm}}{\lambda} \right] - \left[\frac{e^{-S_{\infty}^2 \cos^2 \alpha}}{\pi S_{\infty}} + \cos \alpha \left(\operatorname{erf}(S_{\infty} \cos \alpha) - 1 \right) \right] \frac{X_{cm}}{\lambda} \quad (63)$$

Eq. (63) is shown in Figs. 11, 12 and 13 for cylinder fineness ratios of 1, 2 and 5 respectively and for $T_w = T_\infty$. The temperatures are equated to simplify the presentations. The effect of $T_w \neq T_\infty$, however, is discussed in Section 3.3.2.2.

It may be noticed that the last term in Eq. (63) is quite small when $S_\infty \cos \alpha$ is in excess of about 2.0. Then for small angles of attack this term may be neglected. The pitching moment slope at zero angle of attack may be formed by differentiating Eq. (63) with respect to α and passing to the limit $\alpha \rightarrow 0$. Accordingly, one finds,

$$C_{m\alpha} = -\left(\frac{L}{D}\right) \left\{ \frac{3}{4} \frac{1}{\sqrt{\pi}} \left[\frac{1}{S_\infty} + \frac{T_w}{6 S_\infty} \left(\frac{T_w}{T_\infty} \right) \left(\frac{L}{D} \right) \right] + 1 \right\} \left[1 - 2 \frac{x_{cm}}{L} \right] \quad (64)$$

where the last term in Eq. (63) is ignored and where

$$\lim_{\alpha \rightarrow 0} \left\{ \frac{d}{d\alpha} \left[\sin^2 \alpha F\left(\frac{\alpha}{\pi}\right) \right] \right\} = \frac{\sqrt{\pi}}{2 S_\infty} \quad (65)$$

From Eq. (64) the cylinder is seen to be aerodynamically stable for all centers of mass forward of the geometric center. The results of Eq. (64) will be utilized in the cylinder design analysis of Section 3.4.2.1.

3.2.2.2 Sphere

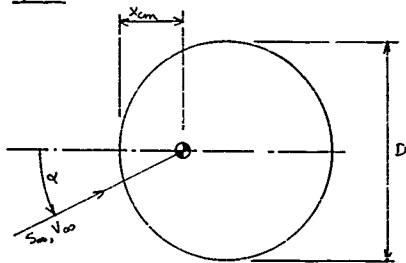


Figure 9. Sphere Nomenclature

The pitching moment coefficient of a sphere is easily calculable since the resultant aerodynamic force (drag) acts through the sphere center. That is,

$$C_m = - \left[\frac{1}{2} - \frac{x_{cm}}{D} \right] C_D \sin \alpha \quad (66)$$

The exact drag coefficient for arbitrary molecular reflection is given by Eq. (49) as

$$C_D = (2 - \Gamma' + \Gamma) Q(S_\infty) + \frac{2\Gamma' \sqrt{\pi}}{3 S_\infty} \sqrt{\frac{T_w}{T_\infty}} \quad (67)$$

where $Q(S_\infty)$ is defined by Eq. (50). Then for diffuse reflection, Eq. (66) becomes upon the substitution of Eqs. (50) and (67)

$$C_m = - \left[\frac{2S_\infty^2 + 1}{2\sqrt{\pi} S_\infty^3} e^{-S_\infty^2} + \frac{4S_\infty^4 + 4S_\infty^2 - 1}{4S_\infty^4} \operatorname{erf}(S_\infty) + \frac{\sqrt{\pi}}{3S_\infty} \sqrt{\frac{T_w}{T_\infty}} \right] \sin \alpha \left[1 - \frac{2x_{cm}}{D} \right] \quad (68)$$

which varies linearly with center of mass location. The normalized version of Eq. (66) is shown in Fig. 11 for $T_w = T_\infty$. Temperature effects are considered in Section 3.3.2.2.

The sphere pitching moment slope at zero angle of attack is

$$C_{m_\alpha} = - \left[\frac{2S_\infty^2 + 1}{2\sqrt{\pi} S_\infty^3} e^{-S_\infty^2} + \frac{4S_\infty^4 + 4S_\infty^2 - 1}{4S_\infty^4} \operatorname{erf}(S_\infty) + \frac{\sqrt{\pi}}{3S_\infty} \sqrt{\frac{T_w}{T_\infty}} \right] \left[1 - \frac{2x_{cm}}{D} \right] \quad (69)$$

which, like the cylinder, is zero for coincident centers of volume and mass.

D.2.2.3 Cone

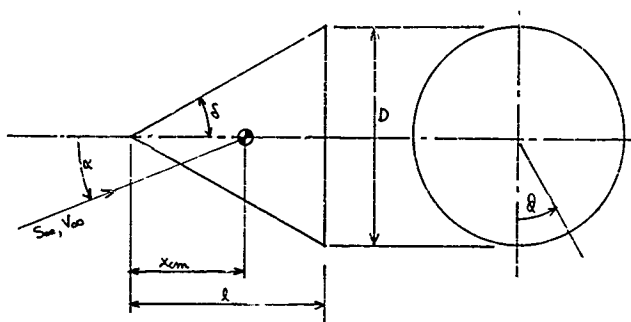


Figure 10. Cone Nomenclature

Unlike the cylinder and the sphere, there appears to be no straight-forward method for obtaining the exact free molecule pitching moment of the cone at angle of attack. Using the last of Eqs. (25), however, approximate pressure and shear coefficients may be integrated with little difficulty. The resulting static pitching moment coefficient may be shown to be (Ref. 4)

$$\begin{aligned}
 C_m \approx & -\frac{1}{2 \tan \delta} \left\{ \left[2(2-\sigma^{-1}) f^*(\zeta) \sin \alpha \cos \alpha + \frac{\sigma^{-1} \sqrt{\pi}}{2 S_{\infty}} \left| \frac{\sqrt{\pi}}{T_{\infty}} \delta^*(\zeta) \right| \frac{\sin \alpha}{\sin \delta} \right. \right. \\
 & \left. \left. + \frac{2-\sigma^{-1}}{S_{\infty}^2} \frac{p^*(\zeta)}{\sin \delta \cos \delta} \right] \left[1 - \frac{3 x_{cm}}{2 l} \cos^2 \delta \right] \right. \\
 & \left. + 3 \sigma \sin \alpha \cos \alpha \left[f^*(\zeta) - \frac{x_{cm}}{l} h^*(\zeta) \right] \right\} \quad (70)
 \end{aligned}$$

where the parameter ξ is defined as $\tan \alpha / \tan \alpha_0$ and

$$f^*(\xi) \equiv \frac{1}{\pi} \left\{ \cos^{-1}(-\xi) + \frac{\xi}{3} \left(1 + \frac{2}{\xi^2} \right) \sqrt{1 - \xi^2} \right\} = \xi^2 [f(\xi) - g(\xi)] \quad (\xi \leq 1.0)$$

$$\equiv 1.0 \quad (\xi \geq 1.0)$$

$$g^*(\xi) \equiv \frac{1}{\pi} \left\{ \cos^{-1}(-\xi) + \xi \sqrt{1 - \xi^2} \right\} = 2\xi^2 [g(\xi) - h(\xi)] \quad (\xi \leq 1.0)$$

$$\equiv 1.0 \quad (\xi \geq 1.0) \quad (71)$$

$$h^*(\xi) \equiv \frac{1}{\pi} \left\{ \cos^{-1}(-\xi) + \frac{1}{\xi} \sqrt{1 - \xi^2} \right\} = h(\xi) \quad (\xi \leq 1.0)$$

$$\equiv 1.0 \quad (\xi \geq 1.0)$$

$$p^*(\xi) \equiv \frac{1}{\pi} \sqrt{1 - \xi^2} \quad (\xi \leq 1.0)$$

$$\equiv 0 \quad (\xi \geq 1.0)$$

The foregoing functions are the result of integrating the pressure and shear over the surface area exposed to the incident molecular stream. The contribution of the "shadow" is neglected in the approximate theory. It is therefore clear that when the angle of attack is less than the cone angle, the entire conical surface "sees" the free stream and the functions assume integer values. Consequently, for diffuse reflection, Eq. (70) is expressible in two parts:

$$C_m \cong -\cot \delta \left\{ \frac{f''}{6S_\infty} \sqrt{\frac{T_w}{T_\infty}} \frac{\sin \alpha}{\sin \delta} \left[1 - \frac{3}{2} \frac{X_{cm}}{l} \cos^2 \delta \right] \right. \\ \left. + \sin \alpha \cos \alpha \left[1 - \frac{X_{cm}}{l} \right] \right\} \quad [\alpha \leq \delta]$$

$$C_m \cong -\cot \delta \left\{ \left[\frac{f''}{6S_\infty} \sqrt{\frac{T_w}{T_\infty}} g^*(\delta) \frac{\sin \alpha}{\sin \delta} + \frac{1}{3S_\infty} \frac{P^*(\delta)}{\sin \delta \cos \delta} \right] \left[1 - \frac{3}{2} \frac{X_{cm}}{l} \cos^2 \delta \right] \right. \\ \left. + \sin \alpha \cos \alpha \left[f^*(\delta) - \frac{X_{cm}}{l} h^*(\delta) \right] \right\} \quad [\alpha \geq \delta]. \quad (72)$$

Eqs. (72) are shown plotted in Figs. 15, 16, and 17 for cone angles of 15° , 30° and 45° respectively and for $T_w = T_\infty$. It may be noticed in these figures that there is a slight discontinuity in the pitching moment slope at the point where α equals δ . These discontinuities are due to the sudden appearance of a shadow ξ as the angle of attack increases beyond the cone angle. If exact free-molecule theory were available for these conditions, however, the shadow area would be properly taken into account, and the discontinuity, if present at all, would be smoothed.

The static pitching moment derivative at zero angle of attack may be found from Eq. (76) or by differentiating the first of Eqs. (72) with respect to α and taking the limit as α approaches zero. The result is,

$$C_{m_\alpha} \cong -\cot \delta \left\{ \frac{f''}{6S_\infty \sin \delta} \sqrt{\frac{T_w}{T_\infty}} \left[1 - \frac{3}{2} \frac{X_{cm}}{l} \cos^2 \delta \right] + \left[1 - \frac{X_{cm}}{l} \right] \right\} \quad (73)$$

which is applicable for $S_\infty \sin \delta$ greater than unity.

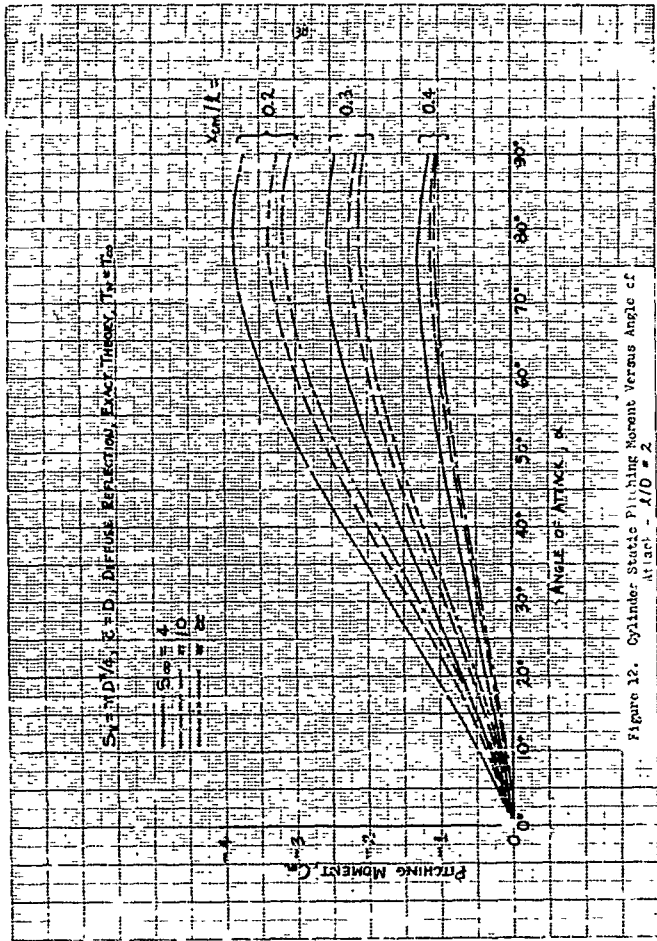


Figure 12. Cylinder Static Pitching Moment Versus Angle of Attack - $L/D = 2$

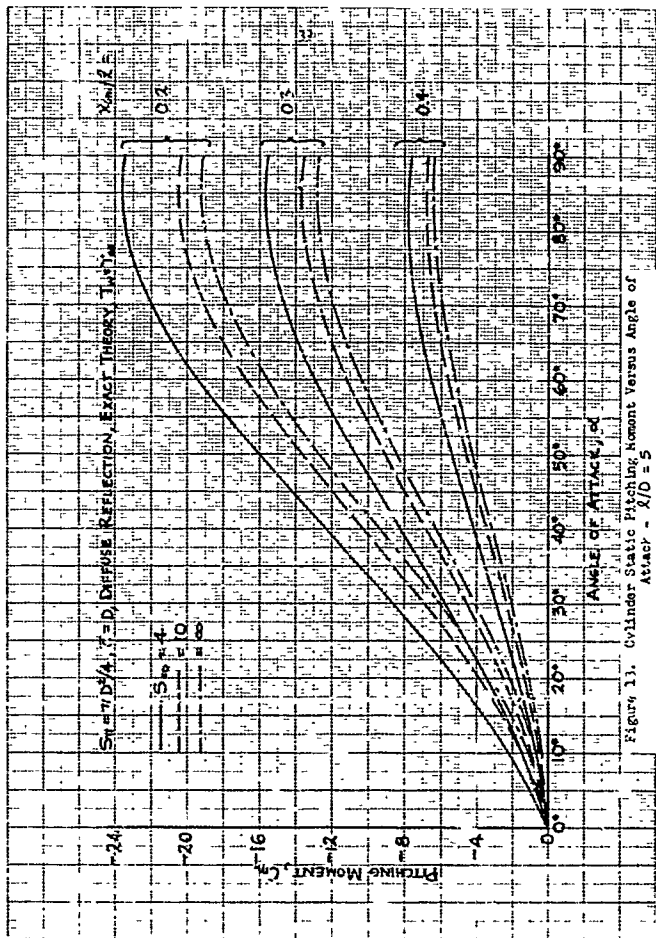


Figure 11. Cylinder Static Pitching Moment Versus Angle of Attack - $X/D = 5$

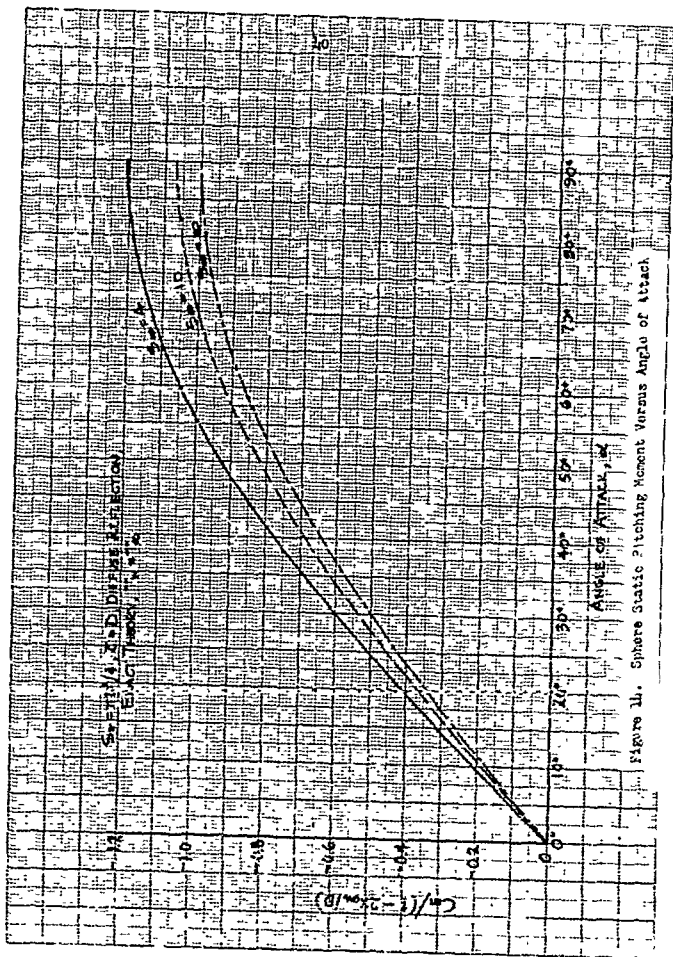
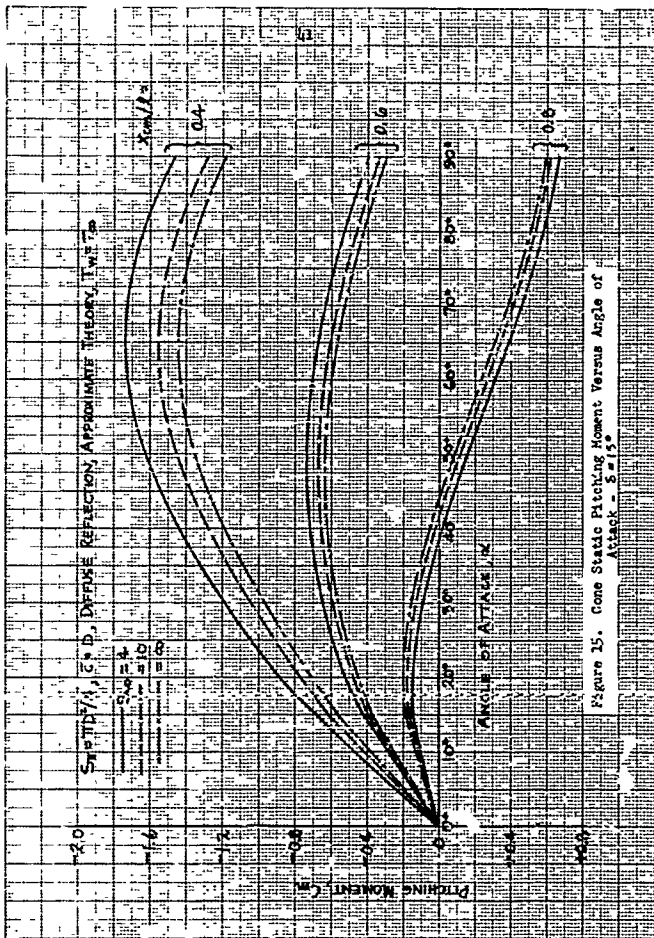
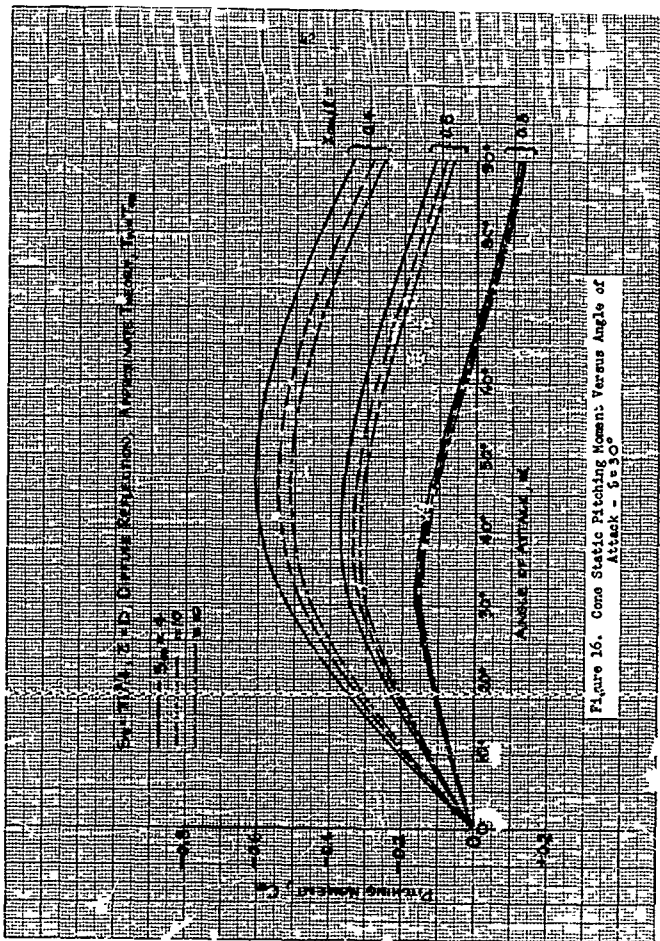


Figure 11. Sphere Static Pitching Moment Versus Angle of Attack





3.2.3 Pitching Moment Slopes of Complex Body Shapes

3.2.3.1 Power Law Body

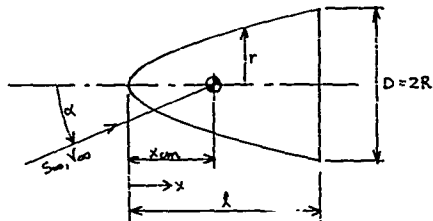


Figure 18. Power Law Body Nomenclature

As the result of the cylinder, sphere and cone stability comparison of the previous section, it seems worthwhile to continue the analysis for somewhat more practical shapes. The power law body is such a shape, and hence, is described below.

A power law body of revolution is described by the well-known formula,

$$\frac{r}{R} = \left(\frac{x}{l}\right)^n \quad (74)$$

where R and l are the maximum body radius and length respectively, and where $0 < n \leq 1$. Now the slope of the pitching moment coefficient, $C_{m\alpha}$, at zero angle of attack for a body of revolution with $r' > 0$ may be determined from Eq. (26) using the approximate free-molecule theory. The result of substituting Eq. (74) and its derivatives in Eq. (26) is

$$\begin{aligned}
 C_{m\alpha} \cong & \frac{\ell}{R^3} \left\{ 2(2-\sigma-\sigma^2)nR^2 \int_0^1 \frac{nR^2 \left(\frac{x}{\ell}\right)^{4n-2} + \left(\frac{x}{\ell}\right)^{2n} - \frac{x_{cm}}{\ell} \left(\frac{x}{\ell}\right)^{2n-1}}{1 + \frac{n^2 R^2}{\lambda^2} \left(\frac{x}{\ell}\right)^{2n-2}} d\left(\frac{x}{\ell}\right) \right. \\
 & + \frac{\sigma' \sqrt{\pi}}{2S_{\infty}} \sqrt{\frac{T_w}{T_{\infty}}} R\ell \int_0^1 \frac{nR^2 \left(\frac{x}{\ell}\right)^{3n-1} + \left(\frac{x}{\ell}\right)^{n+1} - \frac{x_{cm}}{\ell} \left(\frac{x}{\ell}\right)^n}{\left[1 + \frac{n^2 R^2}{\lambda^2} \left(\frac{x}{\ell}\right)^{2n-2}\right]^{1/2}} d\left(\frac{x}{\ell}\right) \\
 & \left. + \sigma R^2 \int_0^1 \left[(2n+1) \left(\frac{x}{\ell}\right)^{2n} - 2n \left(\frac{x_{cm}}{\ell}\right) \left(\frac{x}{\ell}\right)^{2n-1} \right] d\left(\frac{x}{\ell}\right) \right\}. \quad (75)
 \end{aligned}$$

Except for a few special cases, the first two integrals in Eq. (75) have not been evaluated (at present) for a general value of n . For diffuse molecular reflection, however, $\sigma = \sigma' = 1.0$ and the coefficient of the first integral is identically zero. Also, sample calculations have shown, using Fig. 2, that the temperature-dependent term is less than 5% of the dominant, last term. Therefore, if diffuse reflection is assumed, and if the second term is neglected, Eq. (75) becomes

$$C_{m\alpha} \cong -\frac{\ell}{R} \int_0^1 \left[(2n+1) \left(\frac{x}{\ell}\right)^{2n} - 2n \left(\frac{x_{cm}}{\ell}\right) \left(\frac{x}{\ell}\right)^{2n-1} \right] d\left(\frac{x}{\ell}\right).$$

This integral may be evaluated exactly, giving the result,

$$C_{m\alpha} \cong -2 \left(\frac{\ell}{D}\right) \left[1 - \frac{x_{cm}}{\ell} \right] \quad (76)$$

which is independent of n . Consequently, for diffuse reflection, the only effect of the exponent on pitching moment slope is due to the small contribution of the reflected pressure coefficient, as treated in Section 1. Also, it may be seen that Eq. (76) agrees with the leading term of Eq. (72) for the cone ($n=1$).

2.2.3.2 Truncated Cone

The stability analysis of the more complex geometrical shapes continues herein for the case of a cone frustum. The calculations are considerably more complicated for this configuration since the degree of truncation becomes an additional variable. The geometry and nomenclature used for the subsequent calculations are shown below in Figure 19.

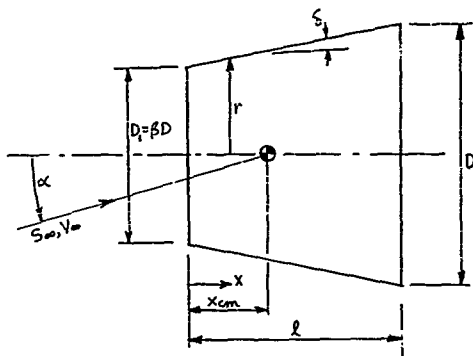


Figure 19. Truncated Cone Nomenclature

The free-molecule pitching moment slope of this shape may be found by combining the separate contributions of the conical surface and the flat nose. Although the exact free-molecule flow theory may be used for the nose portion, it is sufficient (and convenient) to calculate $C_{m\alpha}$ at zero angle of attack using the restrictions that $S_{\infty} > 6$ and $S_{\infty} \sin \alpha > 1$. Then for diffuse molecular reflection, Eq. (20) shows that $C_{m\alpha}$ of the conical portion ($dr/dx \neq 0$) is

$$C_{m_{\alpha, \text{NOSE}}} \cong -2 \frac{l}{D} \left\{ \frac{\sqrt{\pi} \sqrt{T_w/T_{\infty}}}{S_{\infty} \sqrt{(1-\beta)^2 + 4(\frac{l}{D})^2}} \left[\frac{1}{3} \left(\frac{l}{D} \right)^2 (2+\beta) + \frac{1}{6} (1-\beta^3) \right. \right. \\ \left. \left. - \frac{X_{cm}}{l} \left(\frac{l}{D} \right)^2 (1+\beta) \right] + \left[1 - (1-\beta^2) \frac{X_{cm}}{l} \right] \right\} \quad (77)$$

and correspondingly, the nose contribution is

$$C_{m_{\alpha, \text{NOSE}}} \cong 2 \left(\frac{l}{D} \right) \frac{X_{cm}}{l} \beta^2 \quad (78)$$

where β is the ratio of the nose diameter to the base diameter. The total static pitching moment slope is the sum of Eqs. (77) and (78). That is,

$$C_{m_{\alpha, \text{TOTAL}}} \cong -2 \left(\frac{l}{D} \right) \left\{ \frac{\sqrt{\pi} \sqrt{T_w/T_{\infty}}}{S_{\infty} \sqrt{(1-\beta)^2 + 4(\frac{l}{D})^2}} \left[\frac{1}{3} \left(\frac{l}{D} \right)^2 (2+\beta) + \frac{1}{6} (1-\beta^3) \right. \right. \\ \left. \left. - \frac{X_{cm}}{l} \left(\frac{l}{D} \right)^2 (1+\beta) \right] + \left[1 - \frac{X_{cm}}{l} \right] \right\} \quad (79)$$

It is not difficult to show for reasonable configurations with $S_{\infty} \sin \zeta > 2$ that the temperature-dependent term in Eq. (79) is considerably smaller than the last term. Although the difference will be shown later, it is now convenient to neglect the temperature term and write Eq. (79) as

$$C_{m_{\alpha}} \cong -2 \left(\frac{l}{D} \right) \left[1 - \frac{X_{cm}}{l} \right] \quad (80)$$

which is the same equation used in the previous section for power law bodies. As Eq. (80) is presented above, $C_{m_{\alpha}}$ is independent of the diameter ratio β .

3.2.3.5 Hemisphere-Cylinder

The geometry of the hemisphere-cylinder is shown in Fig. 20.

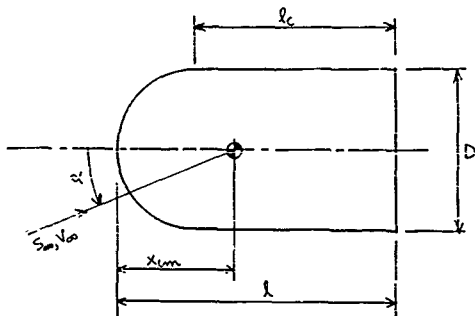


Figure 20. Hemisphere-Cylinder Nomenclature

The pitching moment slope of a hemisphere-cylinder may be found by adding the spherical cap contribution to the cylinder contribution, both of which have been discussed previously. As α approaches zero the value of $C_{m\alpha}$ for the hemisphere is essentially the same as the value for the complete sphere since the contribution of the aft portion of the sphere is negligible. Then from Eq. (69)

$$C_{m\alpha_{HS}} = - \left\{ Q(S_{cm}) + \frac{\pi}{3S_{cm}} \sqrt{\frac{T_w}{T_\infty}} \right\} \left[1 - \frac{2x_{cm}}{D} \right] \quad (81)$$

where $Q(S_{cm})$ is defined by Eq. (50) and where diffuse reflection is assumed. Likewise, $C_{m\alpha}$ for the cylinder, without end effects, may be found by differentiating Eq. (60) with respect to α and passing to the $\alpha=0$ limit. The result is, for $\sigma = \sigma' = 1.0$,

$$C_{m\alpha_{cyl}} = - \frac{l_c}{D} \left\{ \frac{3}{\pi} \left[\frac{1}{S_{cm}} + \frac{\pi}{6S_{cm}} \sqrt{\frac{T_w}{T_\infty}} \right] \frac{l_c}{D} \left[1 - 2 \frac{x_{cm}}{l_c} \right] + \dots \right\} \quad (82)$$

where l_c and x_{cm} are measured from the origin of the cylinder. From Fig. 20 it is seen that

$$\lambda = \lambda_c + D/2$$

$$x_{cm} = x_{cm_c} + D/2$$

These relations may be substituted in Eq. (82) to provide a common reference basis; i.e.,

$$C_{m_{cyl}} = -\left(\frac{1}{D} - \frac{1}{2}\right) \left\{ \frac{3}{\pi} \left[\frac{1}{S_\infty} + \frac{\pi}{6S_\infty} \left| \frac{T_w}{T_\infty} \right| \right] \left[\frac{1}{D} + \frac{1}{2} - 2 \frac{x_{cm}}{D} \right] + 1 \right\} \quad (83)$$

where λ/D is greater than $1/2$. The combination of Eqs. (81) and (83) gives the total pitching moment slope of a hemisphere-cylinder with diffuse reflection:

$$C_{m_x} = -\left\{ X - Y \frac{x_{cm}}{D} \right\} \quad (84)$$

where

$$X \equiv \left(\frac{3}{\pi S_\infty} + \frac{\pi}{2S_\infty} \left| \frac{T_w}{T_\infty} \right| \right) \left(\frac{\lambda}{D} \right)^2 + \left(\frac{\lambda}{D} \right) + \left(\alpha(S_\infty) - \frac{1}{2} - \frac{3}{4\pi S_\infty} + \frac{5\pi}{24S_\infty} \left| \frac{T_w}{T_\infty} \right| \right) \quad (85)$$

$$Y \equiv \left(\frac{6}{\pi S_\infty} + \frac{\pi}{S_\infty} \left| \frac{T_w}{T_\infty} \right| \right) \left(\frac{\lambda}{D} \right) + \left(\alpha(S_\infty) - \frac{3}{\pi S_\infty} + \frac{\pi}{6S_\infty} \left| \frac{T_w}{T_\infty} \right| \right)$$

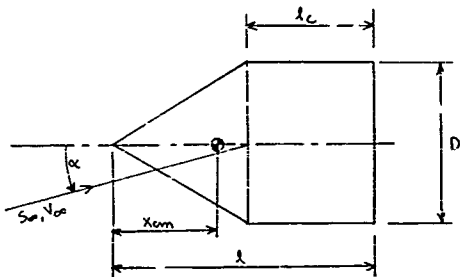
3.2.3.4 Cone-Cylinder

Figure 21. Cone-Cylinder Nomenclature

The static pitching moment slope of the cone-cylinder configuration is easily obtained since both portions have been previously calculated. For diffuse reflection, the approximate free-molecule flow theory gives for the conical portion,

$$C_{m_{\text{cone}}} \cong -\cot\delta \left\{ \frac{\sqrt{\pi}}{6S_m} \left[\frac{T_w}{T_\infty} \left[1 - \frac{3x_{cm}}{D} \sin\delta \cos\delta \right] \right] + \left[1 - 2 \tan\delta \frac{x_{cm}}{D} \right] \right\} \quad (86)$$

which is the same as Eq. (73) except for a slight rearrangement. The $C_{m_{\text{cyl}}}$ due to the cylindrical portion may be written using Eq. (92) and Fig. 21, noting that

$$l = l_c + \left(\frac{D}{2}\right) \cot\delta$$

$$x_{cm} = x_{cm_c} + \left(\frac{D}{2}\right) \cot\delta$$

where l_c and $\langle c_m \rangle_c$ are measured aft from the cylinder shoulder. Thus, Eq. (62) becomes

$$C_{m_{cyl}} = - \left[\frac{l}{D} - \frac{1}{2} \cot \delta \right] \left\{ \frac{3}{\pi} \left[\frac{1}{S_m} + \frac{\pi}{6 S_m} \sqrt{\frac{T_w}{T_a}} \right] \left[\frac{l}{D} \left(1 - 2 \frac{x_{cm}}{l} \right) + \frac{1}{2} \cot \delta \right] + 1 \right\} \quad (87)$$

where l/D is greater than $1/2$. The total cone-cylinder C_{m_x} is the sum of Eqs. (86) and (87):

$$C_{m_x} \cong - \left\{ J \left[\left(1 - 2 \frac{x_{cm}}{l} \right) \left(\frac{l}{D} \right) + \cot \delta \frac{x_{cm}}{l} \left(\frac{l}{D} \right) - \frac{1}{4} \cot^2 \delta \right] \right. \\ \left. + K \left[-3 \cot \delta \cos \delta \frac{x_{cm}}{l} \left(\frac{l}{D} \right) + \frac{\cot \delta}{\sin \delta} \right] + \left[\left(1 - 2 \frac{x_{cm}}{l} \right) \left(\frac{l}{D} \right) + \frac{1}{2} \cot \delta \right] \right\} \quad (88)$$

where

$$J \equiv \frac{3}{\pi S_m} + \frac{\pi}{2 S_m} \sqrt{\frac{T_w}{T_a}} \quad (89)$$

$$K \equiv \frac{\pi}{6 S_m} \sqrt{\frac{T_w}{T_a}}$$

3. Miscellaneous Effects on Stability

3.3.1 Introduction

As stated several times throughout this report, the complexity of free-molecule force and moment calculations is reduced if the surface temperature, T_w , and the tangential and normal momentum coefficients, Γ and Γ' , are assumed constant for a given configuration. Although these assumptions are reasonable for most engineering applications, it is desirable to investigate the magnitude of stability changes caused by surface temperature and reflection coefficient variations. In reality, the reflection coefficients may vary with surface temperature as well as being dependent on surface material and irregularities. For the subsequent calculations, however, it will be assumed that Γ and Γ' are independent of T_w . Moreover, for the temperature investigations, the commonly accepted diffuse values of $\Gamma = \Gamma' = 1.0$ are assigned, while for the reflection coefficient investigations, T_w is assumed to be 550°R and Fig. 2 is assumed applicable.

3.3.2 Effect of Uniform Temperature Level on Stability

In Section 3.2.2 equations for the static pitching moment coefficients were presented for the basic body shapes: the cylinder, sphere, and cone. The accompanying figures, however, were drawn for the special case of $T_w = T_\infty$ (for simplicity only). It is therefore the purpose of this section to present equations and graphs for the incremental pitching moment coefficient due to $T_w \neq T_\infty$. Since the basic equations have been discussed previously, additional elaboration is held to a minimum.

3.3.2.1 Cylinder

From Eq. (63), it is easily shown that

$$C_m - C_{m_{T_w=T_\infty}} \equiv \Delta C_m = -\left(\frac{l}{D}\right)^2 \sin \alpha \frac{\pi}{2S_{ref}} \left[\frac{T_w}{T_\infty} - 1 \right] \left[1 - 2 \frac{x_{cm}}{l} \right]$$

or

$$\frac{S_{ref} \Delta C_m}{\left(\frac{l}{D}\right)^2 \left[1 - 2 \frac{x_{cm}}{l} \right]} = -\frac{\pi}{2} \left[\frac{T_w}{T_\infty} - 1 \right] \sin \alpha \quad (90)$$

Eq. (90) is plotted in Fig. 22 versus angle of attack for several temperature ratios. It may be noticed that for large cylinder fineness ratios, the temperature effect may become significant. Also, it should be pointed out that the lat nose contribution to C_m (shear) is independent of temperature.

3.3.2.2 Sphere

The effect of $T_w \neq T_\infty$ on the sphere C_m is shown to be, from Eq. (68)

$$\frac{S_\infty \Delta C_m}{\left[1 - \frac{3}{2} \frac{x_{cm}}{R}\right]} = -\frac{\sqrt{\pi}}{3} \left[\left| \frac{T_w}{T_\infty} - 1 \right| \right] \sin \alpha \quad (91)$$

which is plotted in Fig. 23. Unlike the cylinder, temperature only slightly affects the sphere pitching moment.

3.3.2.3 Cone

As indicated previously, the cone at angle of attack must be treated in two parts; namely, at $\alpha \leq \delta$ when the cone angle δ , and α greater than δ . Then, from Eq. (72),

$$\begin{aligned} \frac{S_\infty \Delta C_m \sin^2 \delta}{\cos \delta \left[1 - \frac{3}{2} \frac{x_{cm}}{R} \cos^2 \delta\right]} &\approx -\frac{\sqrt{\pi}}{6} \left[\left| \frac{T_w}{T_\infty} - 1 \right| \right] \sin \alpha \quad [\alpha \leq \delta] \\ \frac{S_\infty \Delta C_m \sin^2 \delta}{\cos \delta \left[1 - \frac{3}{2} \frac{x_{cm}}{R} \cos^2 \delta\right]} &\approx -\frac{\sqrt{\pi}}{6} \delta^2(\alpha) \left[\left| \frac{T_w}{T_\infty} - 1 \right| \right] \sin \alpha \quad [\alpha \geq \delta] \end{aligned} \quad (92)$$

where $\delta^2(\alpha)$ is defined by the second of Eqs. (71). Eqs. (92) are shown in Fig. 24 for cone angles of 15° , 30° and 45° . Here again, as for other bodies of revolution with non-zero slopes, the temperature effect on stability is small as long as the fineness ratio is not large. This small increment may be illustrated by plotting the cone total pitching moment slope, $C_{m\alpha}$, versus altitude for various levels of surface temperatures. Such a plot is presented in Fig. 25 using Eq. (73) with a cone angle $\delta = \cos^{-1} \left[\frac{2}{3} \right]$ (an optimum value as shown in Section 3.4.2.3). A circular orbit is assumed so that T_∞ , and hence S_∞ , may be written as functions of altitude using the 1959 ARLW atmosphere (Ref. 7). It is clearly seen from Fig. 25 that surface temperature has a small ($\approx 5\%$) effect on the stability of a typical cone.

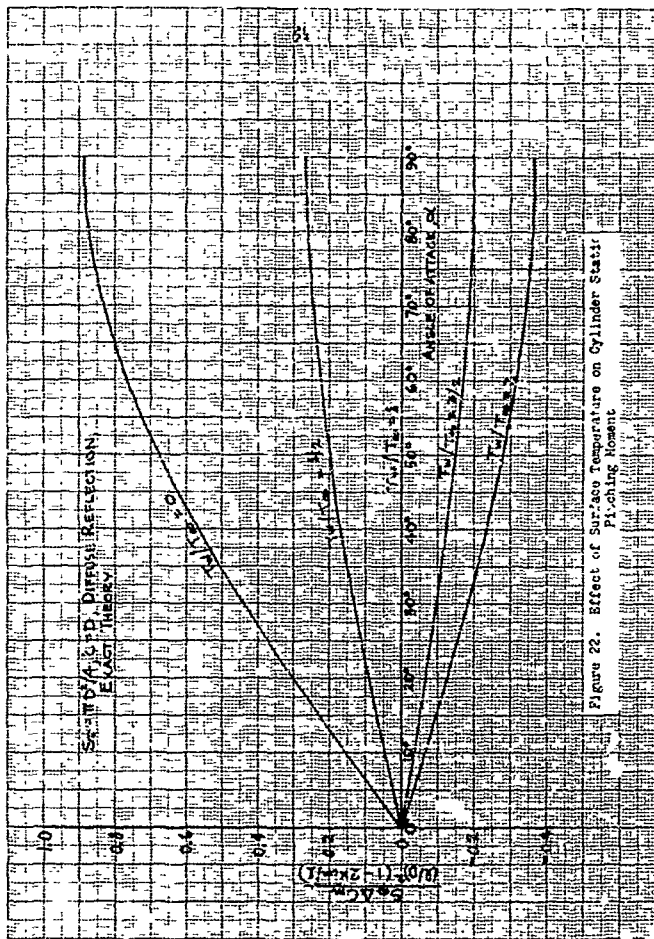


Figure 22. Effect of Surface Temperature on Cylinder Static Pitching Moment

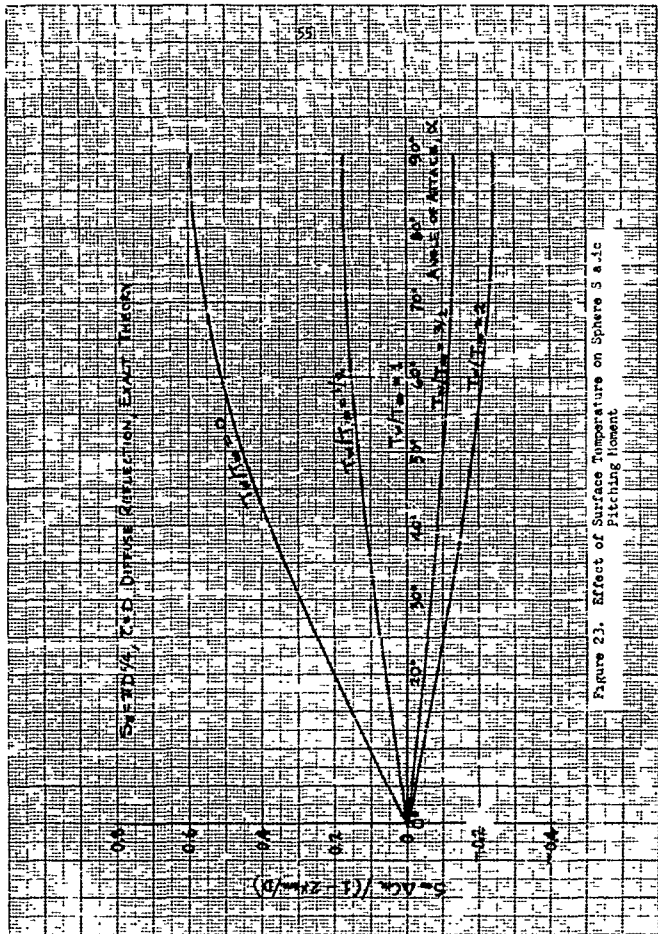


Figure 23. Effect of Surface Temperature on Sphere S a.c Pitching Moment

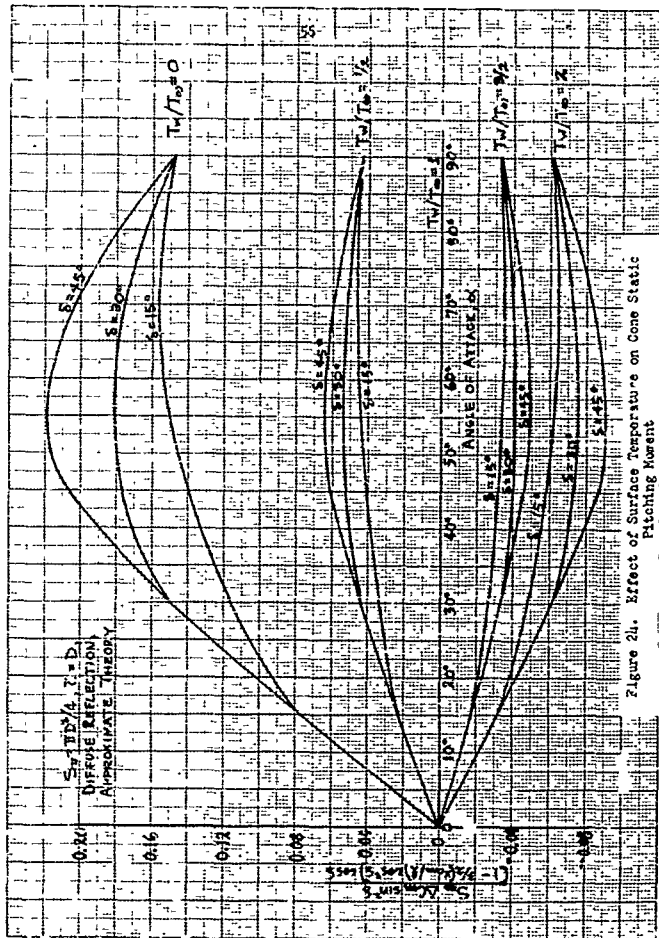


Figure 24. Effect of Surface Temperature on Cone Static Pitching Moment

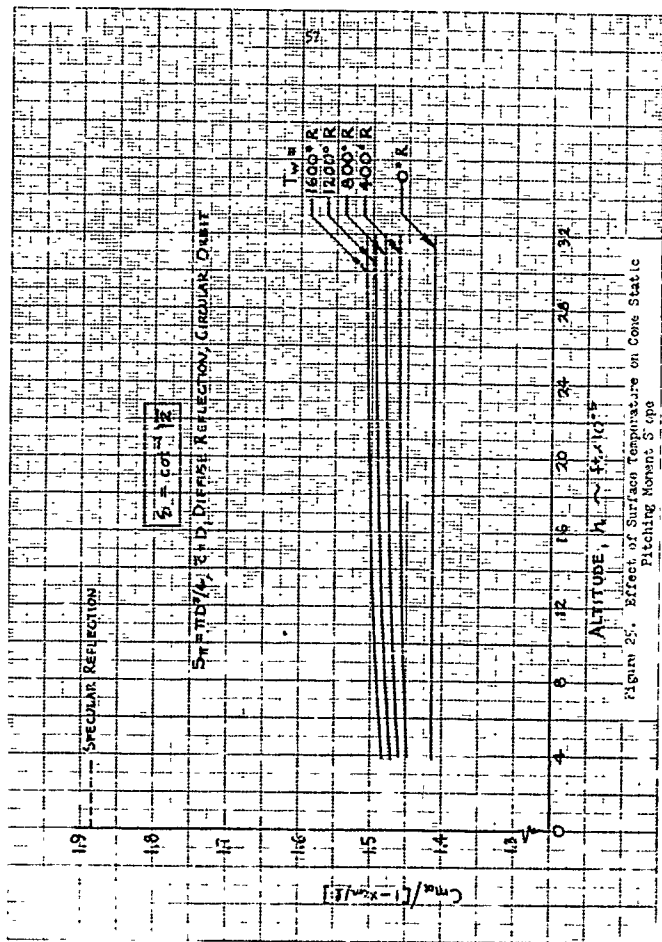


Figure 25. Effect of Surface Temperature on Cone Static Pitching Moment S'_{cp}

3.3.3 Effect of Asymmetric Temperature Variation on Stability

In order to investigate the effects of an asymmetric variation of surface temperature, the basic pitching moment integral, Eq. (20), must be utilized. It may be remembered that for a completely diffuse gas-surface interaction, the only effect of temperature is on the pressure or normal momentum component due to re-emitted molecules (Refs. 1, 3).

The "reflected" pressure coefficient may be written from Eq. (5) (for Maxwellian re-emission),

$$C_{Pr} = \frac{2Pa}{\rho_{\infty} V_{\infty}^2} = \left(\frac{S_M}{S_{ref}} \right) \frac{\sqrt{\pi}}{2S_M} \sqrt{\frac{T_w}{T_{\infty}}} \left[\frac{e^{-S_M^2}}{S_M \sqrt{\pi}} + (1 + \text{erf } S_M) \right] \quad (93)$$

where T_w is regarded, for simplicity, as a fictitious temperature corresponding to a surface from which the molecules reflect with complete thermal accommodation.

Since the shear stress and the "incident" pressure are independent of surface temperature, the last of Eqs. (20) for a body of revolution at zero angle of attack may be written as

$$C_{m_0} = -\frac{1}{S_{ref} \bar{c}} \int_{S_{ref}} C_{Pr} (rr' + x - x_{cm}) r \cos \theta dx d\theta \quad (94)$$

where S_{ref} and \bar{c} are the reference area and length, and where the other symbols are defined in Fig. 26 below.

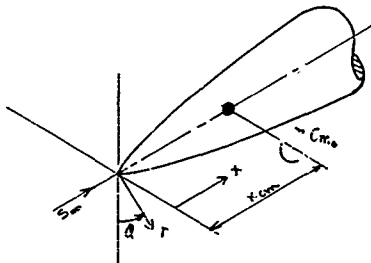


Figure 26. Body of Revolution at Zero Angle of Attack

Now consider a non-spinning satellite orbiting at zero angle of attack with the sun directly overhead. For a body of revolution, the upper half will be in direct sunlight while the bottom half is in a shadow. If the satellite is assumed completely insulated (no internal heat transfer) and if free-molecule convective heat transfer is neglected in comparison to that due to radiation, then the upper and lower portions of the satellite will achieve different temperature levels. The corresponding values of pressure coefficient will likewise be different. Consequently, Eq. (93) may be separated into

$$C_{p_{r_u}} = \left(\frac{S_u}{S_\infty}\right) \frac{\sqrt{\pi}}{2S_\infty} \sqrt{\frac{T_{wu}}{T_\infty}} \left[\frac{e^{-S_u^2}}{S_u \sqrt{\pi}} + (1 + \operatorname{erf} S_u) \right]$$

and

(95)

$$C_{p_{r_l}} = \left(\frac{S_l}{S_\infty}\right) \frac{\sqrt{\pi}}{2S_\infty} \sqrt{\frac{T_{wl}}{T_\infty}} \left[\frac{e^{-S_l^2}}{S_l \sqrt{\pi}} + (1 + \operatorname{erf} S_l) \right]$$

where the subscripts u and l refer to the upper and lower surfaces.

For a right circular cylinder, Eqs. (93) and (95) simplify considerably since S_N and $r' = dr/dx$ are zero. Hence,

$$C_{m_{o_{cyl}}} = -\frac{4}{\pi D^2} \left[\int_0^k \int_0^{\pi/2} \frac{1}{2S_\infty^2} \sqrt{\frac{T_{wu}}{T_\infty}} (x - x_{cm}) \cos \theta \, d\theta \, dx \right. \\ \left. + \int_0^k \int_{\pi/2}^\pi \frac{1}{2S_\infty^2} \sqrt{\frac{T_{wl}}{T_\infty}} (x - x_{cm}) \cos \theta \, d\theta \, dx \right] \quad (96)$$

$$C_{m_{o_{cyl}}} = \frac{(kD)^2}{\pi S_\infty^2} \left[\sqrt{\frac{T_{wu}}{T_\infty}} - \sqrt{\frac{T_{wl}}{T_\infty}} \right] \left[1 - \frac{x_{cm}}{k} \right]$$

where, as usual, $S_\infty = \pi D^2/4$ and $\bar{z} = D$

As another example, consider a right circular cone at zero angle of attack. For this case, $S_{N1} = S_{\infty} \sin \delta$ and for reasonably large S_N (say 3.0), the approximate "reflected" pressure coefficient is sufficiently accurate. Then from Eq. (15) or Eqs. (95),

$$C_{Pr_u} \cong \frac{\sqrt{\pi}}{S_{\infty}} \sin \delta \sqrt{\frac{T_{W_u}}{T_{\infty}}} \quad (97)$$

$$C_{Pr_l} \cong \frac{\sqrt{\pi}}{S_{\infty}} \sin \delta \sqrt{\frac{T_{W_l}}{T_{\infty}}}$$

which when substituted in Eq. (94) yields

$$C_{m_{cone}} \cong \frac{-8 \tan \delta \sin \delta}{\sqrt{\pi} D^2 S_{\infty}} \left[\int_0^{\delta} \int_0^{2\pi} \sqrt{\frac{T_{W_l}}{T_{\infty}}} (x \sec^2 \delta - x_{cm}) x \cos \theta d\theta dx \right. \\ \left. + \int_0^{\delta} \int_{\pi/2}^{\pi} \sqrt{\frac{T_{W_u}}{T_{\infty}}} (x \sec^2 \delta - x_{cm}) x \cos \theta d\theta dx \right] \quad (98)$$

$$C_{m_{cone}} \cong \frac{1}{3\sqrt{\pi} S_{\infty} \sin \delta} \left[\sqrt{\frac{T_{W_u}}{T_{\infty}}} - \sqrt{\frac{T_{W_l}}{T_{\infty}}} \right] \left[1 - \frac{3}{2} \frac{x_{cm}}{l} \cos^2 \delta \right].$$

Now that the zero angle of attack pitching moments have been formulated for two simple satellite shapes, the effect of large temperature differences on the equilibrium angle of attack may be determined. For the case at hand (sun-satellite-Earth system), radiation heat transfer techniques are available (Ref. 10) for approximating the upper and lower skin temperatures. For example, assume the following average temperature levels:

$$T_{W_u} \cong 940^{\circ}R \quad (99)$$

$$T_{W_l} \cong 513^{\circ}R$$

and let

$$\left. \begin{aligned} T_{\infty} &= 2500^{\circ}R \\ S_{\infty} &= 74 \end{aligned} \right\} (\text{alt} \approx 10^6 \text{ ft}) \quad (100)$$

where the large surface temperature difference is obviously conservative¹ due to the negligence of heat transfer within the vehicle. Furthermore, for small angles of attack, the static pitching moment coefficient is expressible as

$$C_m = C_{m_0} + C_{m_d} \alpha$$

which for equilibrium conditions ($C_m = 0$) may be rewritten as

$$\alpha_e = - \frac{C_{m_0}}{C_{m_d}} \quad (102)$$

The pitching moment slope, C_{m_d} , has been determined for the cylinder and cone in Sections 3.2.2.1 and 3.2.2.3 respectively for the case of constant surface temperature. These equations, however, are easily modified to include the temperature difference. Consequently for the cylinder, Eq. (64) and Eq. (96) combine to give

$$\alpha_{e_{cyl}} = \frac{\left(\frac{\lambda l_0}{\pi S_{\infty}}\right)^2 \left[\sqrt{\frac{T_{tw}}{T_{\infty}}} - \sqrt{\frac{T_{wl}}{T_{\infty}}} \right] \left[1 - Z \frac{X_{cm}}{l} \right]}{\left\{ \frac{3}{\pi} \left[\frac{1}{S_{\infty}} + \frac{\pi}{12 S_{\infty}} \left(\sqrt{\frac{T_{tw}}{T_{\infty}}} + \sqrt{\frac{T_{wl}}{T_{\infty}}} \right) \right] \left(\frac{\lambda l_0}{D} \right) + \frac{l}{D} \right\} \left[1 - Z \frac{X_{cm}}{l} \right]} \quad (102)$$

$$\alpha_{e_{cyl}} \approx \frac{0.00093 \left(\frac{\lambda l_0}{D} \right)}{0.292 \left(\frac{\lambda l_0}{D} \right) + 1} \quad (\text{radians})$$

¹Recently published results (Ref. 11) of the Discoverer program have indicated that the upper and lower temperatures are quite low and not much different from one another. In some cases, these temperatures were below freezing. It must be remembered, however, that the actual equilibrium temperatures achieved are strongly dependent upon the emissive and absorptive properties of the surface.

where the values of Eqs. (99) and (100) have been used. It is apparent from Eq. (102) that the equilibrium angle is very small, as expected, for a cylinder with a large temperature difference between the upper and lower surfaces. It must be remembered, however, that the temperature effect on reflection coefficients has not been considered in this analysis.

The cone equilibrium angle may now be found in a similar manner. Using Eq. (73) and Eq. (98), Eq. (101) becomes

$$\alpha_{e\text{ CONE}} \cong \frac{\left[\sqrt{\frac{T_{\text{WU}}}{T_{\infty}}} - \sqrt{\frac{T_{\text{WL}}}{T_{\infty}}} \right] \left[1 - \frac{3}{2} \frac{x_{\text{cm}}}{l} \cos^2 \delta \right]}{\left(\pi S_{\infty} \cos \delta \right) \left\{ 3 \left[1 - \frac{x_{\text{cm}}}{l} \right] + \frac{\sqrt{\pi}}{4 S_{\infty} \sin \delta} \left[\sqrt{\frac{T_{\text{WU}}}{T_{\infty}}} + \sqrt{\frac{T_{\text{WL}}}{T_{\infty}}} \right] \left[1 - \frac{3}{2} \frac{x_{\text{cm}}}{l} \cos^2 \delta \right] \right\}} \quad (103)$$

$$\alpha_{e\text{ CONE}} \cong \frac{0.0122 \left[1 - \frac{3}{2} \frac{x_{\text{cm}}}{l} \cos^2 \delta \right]}{\cos \delta \left\{ 3 \left[1 - \frac{x_{\text{cm}}}{l} \right] + \frac{0.0637}{\sin \delta} \left[1 - \frac{3}{2} \frac{x_{\text{cm}}}{l} \cos^2 \delta \right] \right\}}$$

where, as before, Eqs. (99) and (100) are used. For a representative x_{cm}/l of 2/3 (for simplicity), Eq. (103) is

$$\alpha_{e\text{ CONE}} \cong \frac{0.0122 \sin \delta}{\cos \delta + 0.0637 \cos \delta} \quad (104)$$

which is very small for reasonable cone angles.

Although this analysis is obviously incomplete, it may be qualitatively concluded that temperature differences between opposite sides of a satellite have little effect on the aerodynamic pressure difference, and hence, little effect on the equilibrium angle of attack. It should be remembered, however, that although solar radiation was considered herein, the effect of solar photon pressure on satellite pitching moments was not included. If desired, Appendix A may be used to calculate the additional moment contribution due to solar pressure. A brief check, however, has shown that this contribution (for a cylinder at 1 million feet) is smaller than the aerodynamic C_{m_0} due to temperature variations.

3.3.1 Effect of Longitudinal Temperature Distribution on Stability

It may be recalled from previous discussions that the surface temperature of a vehicle in free-molecule flow affects the surface pressure (through the reflected molecules), and hence, aerodynamic

stability of the vehicle. It was shown that for large, conservative temperature differences between the upper and lower surfaces, the effect on zero-lift pitching moment and corresponding equilibrium pitch angle is very small. Another temperature effect to be considered is the influence of a longitudinal temperature distribution on the pitch characteristics of a satellite. This distribution may be the result of (say) conduction due to certain "hot spots" within the vehicle, free-molecule convection, and/or solar radiation. If all these modes are considered, either separately or together, the resulting temperature distribution becomes a complicated function of numerous variables; i.e., surface material, free-stream conditions, surface orientation angle with respect to the sun, etc. For example, if a radiation heat balance is considered alone, the temperature ratio T_w/T_∞ depends on the fourth root of a function of the angle between a surface element and the sun. The square root of the temperature ratio, as used in the aerodynamic pressure equation, then depends on the eighth root of the sun angle function.

The laborious details of a heat transfer analysis do not seem justified for the rather general cases considered herein. It will, therefore, be assumed that an average temperature distribution may be represented by a simple, axisymmetric, power law expression for the purpose of weighing the effects of temperature variations on the aerodynamic pitching moments. For example, let

$$\sqrt{\frac{T_w}{T_\infty}} = \sqrt{\Theta} \left[1 + \frac{x}{l} \right]^\delta \quad (105)$$

where Θ is some reference temperature ratio, x/l is the non-dimensional body length measured from the nose, and the exponent δ is a constant. Now for a body of revolution, the temperature contribution to the initial pitching moment slope, C_{m_α} , may be found from Eq. (25) as

$$\Delta C_{m_\alpha} = -\frac{8}{D^2} \int_0^l \frac{r' \sqrt{\pi}}{2\sqrt{\pi} \sqrt{1+r'^2}} \sqrt{\frac{T_w}{T_\infty}} (rr' + x - x_{cm}) r' dx' \quad (106)$$

where the reference area and length are $\pi D^2/4$ and D respectively. Now for a right circular cone, $r = x \tan \xi$, and on substitution of Eq. (105) into Eq. (106) and subsequent integration yield

$$\Delta C_{m_{\alpha}} = \frac{\sigma' \cos^2 \theta \sqrt{\pi} \sqrt{\theta}}{6 S_{00} \sin \delta} \left\{ \left[1 + \frac{3\lambda}{4} + \frac{3\lambda(\lambda-1)}{5(2!)} + \frac{3\lambda(\lambda-1)(\lambda-2)}{6(3!)} + \dots \right] - \frac{\chi_{\text{temp}} \cos^2 \delta}{\lambda} \left[\frac{3}{2} + \lambda + \frac{3\lambda(\lambda-1)}{4(2!)} + \frac{3\lambda(\lambda-1)(\lambda-2)}{5(3!)} + \dots \right] \right\} \quad (107)$$

Since realistic values of λ cannot be far different from zero (say $-1 < \lambda < 1$), and since the two series in Eq. (107) tend to cancel each other, it may be seen that the constant temperature ($\lambda = 0$) increment of pitching moment slope, which is small when compared with the total pitching slope, is not altered appreciably by the example temperature distribution. As an illustration, Fig. 27 presents a plot of total $C_{m_{\alpha}}$ versus the exponent λ . The $\lambda = 0$ conditions are noted on the figure.

Other examples may be performed yielding the same general result, i.e., the effect of temperature variations over the surface of a satellite in free-molecule flow do not significantly affect the aerodynamic forces and moments as long as the reflection coefficients σ and σ' are assumed invariant with temperature. The effect of variations in σ and σ' will be considered in the next section.

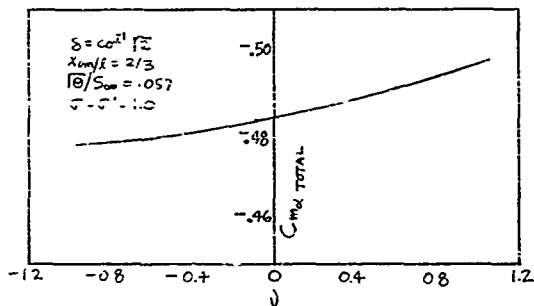


Figure 27. Effect of Longitudinal Temperature Distribution on Cone Pitching Moment Slope

3.3.5 Effect of Asymmetric Reflection Coefficient Variations on Stability

As mentioned before, the effects of variations of the surface reflection coefficients σ and σ' , are analyzed for the special case of constant surface temperature; in particular, for $T_w = 550^\circ R$. For the present problem, it will be assumed that the upper and lower portions of a body of revolution have different values of the reflection coefficients σ and σ' . The resulting difference between the upper and lower shear and pressure forces will then produce changes in the pitching moment. The magnitude of this asymmetric loading may then be analyzed by calculating the equilibrium angle attack, which is, to the first order and for small angles, defined by Eq. (101).

Using the approximate free molecule theory (Ref. 4), it may be shown that the static pitching moment coefficient for a convex body of revolution is

$$C_m \cong -\frac{1}{4\pi Z} \int_0^k \int_0^{2\pi} \left[\left\{ \frac{2(z-\sigma-\sigma')}{1+r'^2} \right\} (r' \cos \alpha + \sin \alpha \cos \beta) \right]^2 \\ + \frac{r' \sqrt{\pi} \sqrt{T_w/T_\infty}}{S_m \sqrt{1+r'^2}} \left\{ r' \cos \alpha + \sin \alpha \cos \beta \right\} + \frac{z-\sigma'}{S_a} \left\{ (rr' + x - x_{cm}) \cos \beta \right\} \\ + 2\sigma' \left\{ r' \cos \alpha + \sin \alpha \cos \beta \right\} \left\{ r \cos \alpha \cos \beta + (x - x_{cm}) \sin \alpha \right\} \right] r d\beta dx \quad (108)$$

which is the same as the last of Eqs. (25) except that σ and σ' are now assumed dependent on the azimuth angle β .

Now if σ and σ' are assigned different values for the upper and lower surfaces, Eq. (108) becomes, for zero angle of attack,

$$C_{m_0} \cong -\frac{Z}{S_m \pi} \int_0^k \left[\left\{ \frac{-2(\sigma_k - \sigma_u + \frac{\sigma_k'}{2} - \frac{\sigma_u'}{2})}{1+r'^2} r'^2 + \frac{(\sigma_k' - \sigma_u') \sqrt{\pi}}{S_m} \sqrt{\frac{T_w}{T_\infty}} \frac{r'}{|1+r'^2|} \right. \right. \\ \left. \left. - \frac{(\sigma_k' - \sigma_u')}{S_m} \right\} (rr' + x - x_{cm}) + 2(\sigma_k - \sigma_u) rr' \right] r dx \quad (109)$$

likewise, the axial pitching moment slope may be found by differentiating Eq. (108) with respect to α , and taking the limit as α approaches zero. The result is,

$$C_{m\alpha} \equiv \frac{-2\pi}{S_{\pi}Z} \int_0^2 \left\{ \frac{(4 - \sigma_x - \sigma_u - \sigma_x' - \sigma_u')}{1+r^2} \right. \\ \left. + \frac{(\sigma_x' + \sigma_u') \sqrt{\pi}}{4\sqrt{1+r^2}} \frac{\sqrt{T_w}}{S_{\alpha} T_{\alpha}} \right\} (rr' + x - x_{cm}) \\ + (\sigma_x + \sigma_u) \left\{ \frac{r}{2} + r'(x - x_{cm}) \right\} r dx \quad (110)$$

For a right circular cone, $r = x \tan \delta$, $S_{\pi} = \pi D^2/4$, $Z = D$ and Eqs. (109) and (110) integrate to yield,

$$C_{m\alpha}_{cone} \equiv \frac{2}{3\pi} \left\{ \Delta\delta + \Delta\sigma' - \frac{\Delta\sigma' \sqrt{\pi}}{2S_{\alpha} \sin \delta} \frac{\sqrt{T_w}}{T_{\alpha}} + \frac{\Delta\sigma'}{2(S_{\alpha} \sin \delta)^2} \right\} \left(1 - \frac{3}{2} \frac{x_{cm}}{l} \cos^2 \delta \right) - \Delta\delta^2 \quad (111)$$

$$(m_{\alpha}_{cone} \equiv \frac{-\cot \delta}{3} \left[\left\{ 2(2 - \sigma_a - \sigma_a') + \frac{\sigma_a' \sqrt{\pi}}{2S_{\alpha} \sin \delta} \frac{\sqrt{T_w}}{T_{\alpha}} \right\} \left(1 - \frac{3}{2} \frac{x_{cm}}{l} \cos^2 \delta \right) \right. \\ \left. + 3\sigma_a \left(1 - \frac{x_{cm}}{l} \right) \right] \quad (112)$$

where

$$\Delta\sigma \equiv \sigma_x - \sigma_u$$

$$\Delta\sigma' \equiv \sigma_x' - \sigma_u'$$

$$\sigma_a \equiv (\sigma_x + \sigma_u)/2$$

$$\sigma_a' \equiv (\sigma_x' + \sigma_u')/2$$

The const. equilibrium angle of attack may now be found by substituting Eqs. (111) and (112) into Eq. (101); i.e.,

$$\alpha_{e, \text{cone}} \cong \frac{2 \tan \delta}{\pi} \left[\frac{\left\{ \Delta \sigma + \Delta \sigma' - \frac{\Delta \sigma' \sqrt{r}}{2 S_m \sin \delta} \left| \frac{\sqrt{T_m}}{T_m} + \frac{\Delta \sigma'}{2 (S_m \sin \delta)^2} \right\} \left(1 - \frac{\pi}{2} \frac{x_{cm}}{k} \cos^2 \delta \right) - \Delta \delta \right]}{\left\{ 2(2 - \sigma_a - \sigma_a') + \frac{\sigma_a' \sqrt{r}}{2 S_m \sin \delta} \left| \frac{\sqrt{T_m}}{T_m} \right\} \left(1 - \frac{\pi}{2} \frac{x_{cm}}{k} \cos^2 \delta \right) + 3 \sigma_a \left(1 - \frac{x_{cm}}{k} \right) \right]} \cdot \quad (113)$$

For purposes of representing an extreme case, let the lower surface reflect in a complete specular fashion, $\sigma_l = \sigma_l' = 0$, while the upper surface reflects in a complete diffuse way, $\sigma_u = \sigma_u' = 1.0$. Then $\Delta \sigma = \Delta \sigma' = -1.0$ and $\sigma_a = \sigma_a' = 1/2$. Furthermore, let $S_m = 74$, $\sqrt{r}/S_m \sqrt{T_m} = 0.063$ (from Fig. 2), $\tan \delta = 1/\sqrt{2}$ and $x_{cm}/k = 2/3$. With these values, Eq. (113) reduces to

$$\alpha_{e, \text{cone}} \cong \frac{2 \tan \delta}{\pi} \left[\frac{-25 \sin^2 \delta + .0558 \sin \delta + .989}{2 \sin^2 \delta + .0279 \sin \delta + .500} \right] \quad (114)$$

$$\alpha_{e, \text{cone}} \cong .156 \text{ radian} \cong 78^\circ$$

The value of Eq. (114) obviously represents an improbable condition. Other more practical reflection coefficient and geometry combinations, however, may result in equilibrium angles of attack which may significantly affect the orientation of a satellite. Body shapes other than the cone may, of course, be analyzed for the effects of non-uniform reflection coefficients. In particular, the cylinder is very sensitive to asymmetric loadings, especially if the ends produce a large C_{m0} .

Numerous other problems may be devised which involve variations of surface temperature and reflection coefficients. Only a few of the more extreme (and simple) cases have been discussed. For example, it has been assumed that σ and σ' are independent of surface temperature, while in reality, it is suspected that a certain dependence between the reflection phenomena and surface temperature exists.

3.3.6 Effect of Non-Diffuse Reflection Coefficients - Stability

In this section, the pitching moment slope $C_{m\alpha}$ is investigated for the case of constant surface temperature (550°R) with uniform, but unequal, values of the tangential and normal momentum exchange coefficients, σ and σ' .

Since the diffuse ($\sigma = \sigma' = 1$) values of $C_{m\alpha}$ have been presented for several configurations in Section 3.2, it is now convenient to use the ratio, $C_{m\alpha}/C_{m\alpha D}$, where, in general, $C_{m\alpha}$ is for $\sigma \neq \sigma' \neq 1$, and where $C_{m\alpha D}$ is for $\sigma = \sigma' = 1$. The examples chosen for illustration are the cylinder, sphere and cone.

3.3.6.1 Cylinder

From Eqs. (62) and (64) it is easily shown that the cylinder $C_{m\alpha}$ ratio is

$$\frac{C_{m\alpha}}{C_{m\alpha D}} = \frac{\left[\frac{4 - 2\sigma' + \sigma}{\sqrt{\pi} S_{\infty}} + \frac{\sigma' \sqrt{\pi}}{2S_{\infty}} \left| \frac{\sqrt{T_w}}{T_{\infty}} \right| \left(\frac{L}{D} \right) \right] + \sigma}{\left[\frac{3}{\sqrt{\pi} S_{\infty}} + \frac{\sqrt{\pi}}{2S_{\infty}} \left| \frac{\sqrt{T_w}}{T_{\infty}} \right| \left(\frac{L}{D} \right) \right] + 1} \quad (115)$$

which is independent of the center of mass location. Now if the approximations $\sqrt{T_w}/S_{\infty} \sqrt{T_{\infty}} \approx 0.063$ and $S_{\infty} \approx 7.4$ are used, and if a representative fineness ratio of 1.08 (an optimum value, as shown later) is assumed, then Eq. (115) may be written approximately as

$$\frac{C_{m\alpha}}{C_{m\alpha D}} \approx \frac{0.330 + 1.082\sigma - 0.131\sigma'}{1.281} \quad (116)$$

where other practical choices of S_{∞} , T_w and L/D do not appreciably affect the numerical results. Eq. (116) is shown plotted in Fig. 28 versus the tangential reflection coefficient σ with the normal reflection coefficient σ' as a parameter. The ratio σ'/σ could also be used as an effective parameter. If a reasonable lower limit, say 0.5, is assigned to σ and σ' , it may be seen that a deviation as much as 18% in $C_{m\alpha}$ could be incurred. As expected, the cylinder $C_{m\alpha}$ is strongly affected by the shear term, and hence, decreases substantially with decreasing σ .

3.3.6.2 Sphere

Section 2.4 may be used to find the $C_{m\alpha}$ for the sphere since $C_{m\alpha}$ for this configuration is directly proportional to the drag coefficient. Then from Eqs. (49) and (51), $C_{m\alpha}/C_{m\alpha D}$ may be written exactly as

$$\frac{C_{m\alpha}}{C_{m\alpha D}} = \frac{C_D}{C_{D_0}} = \frac{(2-\sigma-\sigma') Q(S_\alpha) + \frac{2\sigma'\sqrt{\pi} \sqrt{T_w}}{3S_\alpha} \sqrt{\frac{T_w}{T_\infty}}}{2 Q(S_\alpha) + \frac{2\sqrt{\pi} \sqrt{T_w}}{3S_\alpha} \sqrt{\frac{T_w}{T_\infty}}} \quad (117)$$

where from Eq. (50),

$$Q(S_\alpha) \equiv \frac{2S_\alpha^2+1}{2\sqrt{\pi} S_\alpha^3} e^{-S_\alpha^2} + \frac{4S_\alpha^4+4S_\alpha^2-1}{4S_\alpha^4} \operatorname{erf}(S_\alpha)$$

Now if the usual assumptions of $S_\alpha \approx 7.4$ and $\sqrt{T_w}/S_\alpha \sqrt{T_\infty} \approx 0.063$ are used, then

$$\frac{C_{m\alpha}}{C_{m\alpha D}} \approx \frac{2036 - 1.018\sigma - 0.944\sigma'}{2110} \quad (118)$$

which is graphically presented in Fig. 29. The sphere is seen to be different from the cylinder in that σ and σ' have nearly equal and opposite effects on $C_{m\alpha}$. That is, decreasing σ tends to decrease stability, while decreasing σ' tends to increase stability by nearly the same amount. If a lower limit of 0.8 is assigned to the reflection coefficients, the maximum deviation in $C_{m\alpha}$ is again seen to be approximately 18%. For $\sigma = \sigma'$, however, the deviation is very small. In fact, the completely specular $C_{m\alpha}(\sigma = \sigma' = 0)$ is nearly 70.5% of $C_{m\alpha D}$.

3.3.6.3 Cone

For semi-vertex angles greater than (say) 10° , the cone pitching moment slope at zero angle of attack has been written approximately by Eq. (73) for diffuse reflection and by Eq. (112) for general values of the reflection coefficients. The quotient of Eq. (73) into Eq. (112) is

$$\frac{C_{m\alpha}}{C_{m\alpha D}} \approx \frac{\left[2(2-\sigma-\sigma') + \frac{\sigma'\sqrt{\pi} \sqrt{T_w/T_\infty}}{2S_\alpha \sin \delta} \right] \left[1 - \frac{3}{2} \frac{X_{\text{conc}}}{l} u^{-1} \right] + 3\sigma \left[1 - \frac{X_{\text{conc}}}{l} \right]}{\left[\frac{\sqrt{\pi} \sqrt{T_w/T_\infty}}{2S_\alpha \sin \delta} \right] \left[1 - \frac{3}{2} \frac{X_{\text{conc}} \cos^2 \delta}{l} \right] + 3 \left[1 - \frac{X_{\text{conc}}}{l} \right]} \quad (119)$$

Now if β is chosen as $\cos^{-1} \sqrt{2}$, then $\cos^2 \beta = 2/3$, and the center of mass terms conveniently cancel. Eq. (119) then reduces to

$$\frac{C_{m\alpha}}{C_{m\alpha 0}} \cong \frac{4 + \sigma - 1.902 \sigma'}{3.098} \quad (120)$$

where $\sqrt{T_w / S_m \sqrt{T_\infty}}$ is again assumed 0.063. Eq. (120) is shown plotted in Fig. 3. Unlike the cylinder and the sphere, the cone is seen to be affected more by the pressure forces than by the shear forces (at least for the low fineness ratio cone selected here). An 18% maximum deviation between $C_{m\alpha}$ at $\sigma = 1.0$, $\sigma' = 0.8$ and vice versa, is again (by coincidence) evident. The cone $C_{m\alpha}$ for $\sigma = \sigma' = 0.8$, however, is increased by only 6%. From Eq. (120) the specular $C_{m\alpha}$ is approximately 30% higher than the diffuse $C_{m\alpha}$.

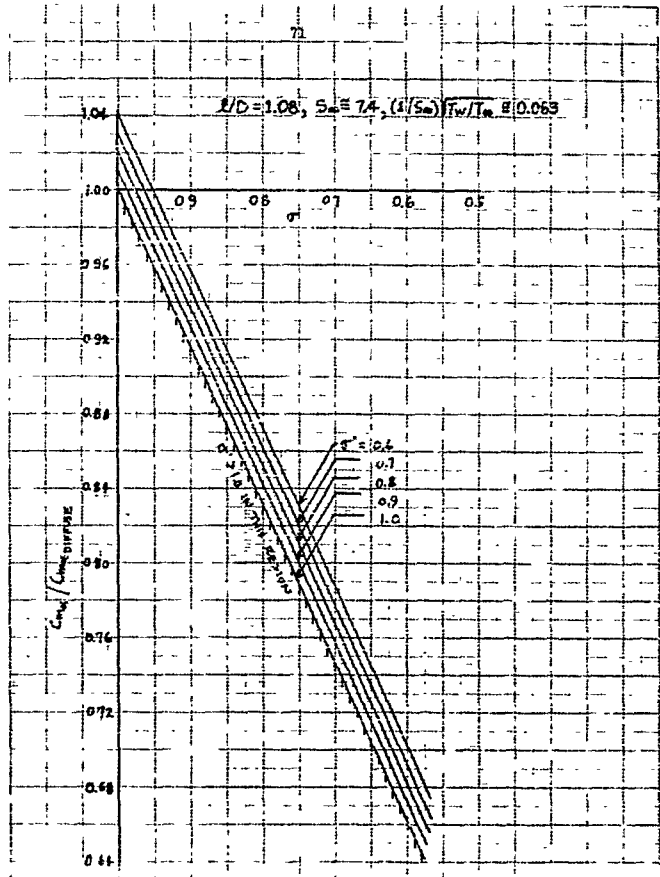


Fig. 4. Effect of $\sigma \neq 90^\circ$ on Cylinder C_{m0}

$$S_{\infty} = 1.4 \left(\frac{1}{5\sigma} \right) \left(\frac{1}{1.1\sigma} \right) = 0.063$$

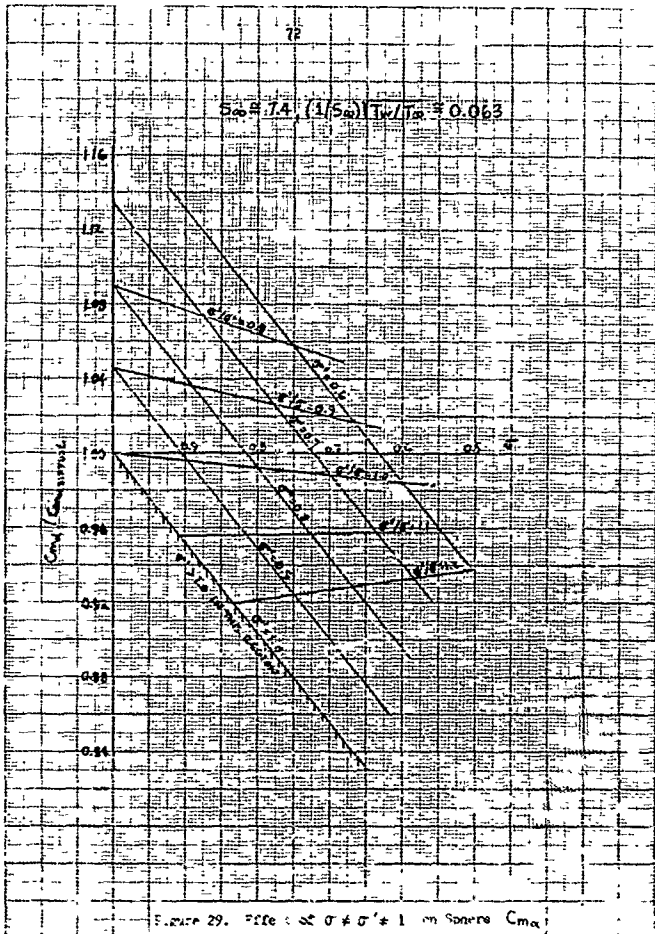
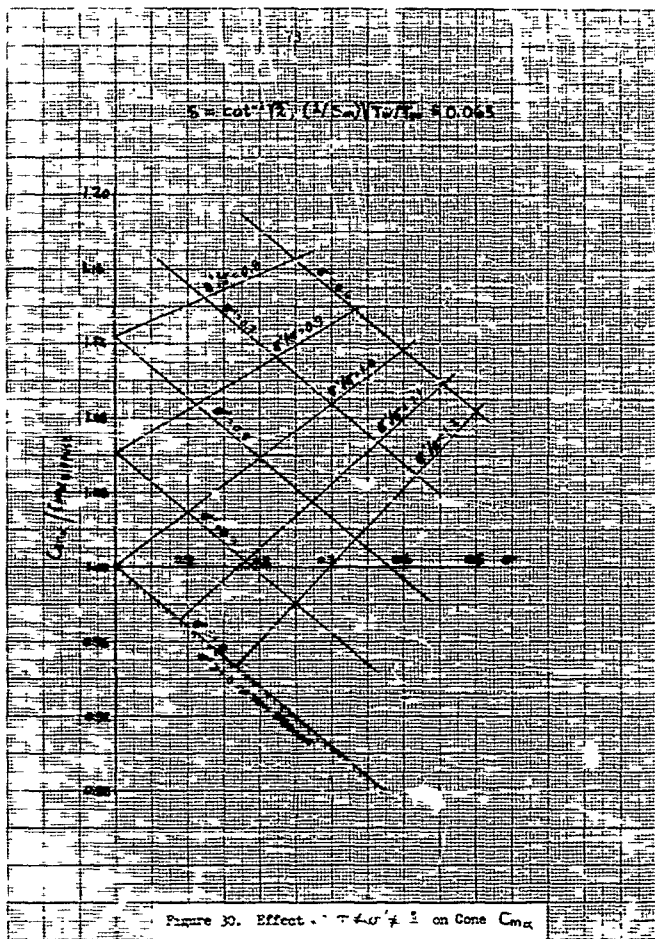


Figure 29. Plot of S_{∞} vs C_{max} for $\sigma = 1$ on Sphere C_{max}



3.4 Optimum Shapes

3.4.1 Review and Introduction

In Volume I of this series of reports it is emphasized that successful aerodynamic stabilization of axisymmetric, rear-Earth satellites depends upon the magnitude (and sign, of course) of the aerodynamic stability parameter \mathcal{O}_p^* . This parameter is defined as

$$\mathcal{O}_p^* \equiv \Gamma \frac{\rho_k r_p^2}{2} \left(\frac{V_k}{V} \right)^2 \quad (121)$$

where

$$\Gamma \equiv \frac{-C_{M_x} S \pi \bar{c}}{\bar{I}} \quad (122)$$

ρ_k = atmospheric density at semi-latus rectum

r_p = perigee radius

V_k/V = relative-to-inertial velocity ratio

\bar{I} = principal moment of inertia about the y body-fixed axis.

It is also noted in Volume I that \mathcal{O}_p^* is used in combination with the gravity torque parameter M , which is defined as

$$M \equiv \frac{\bar{I}_x - \bar{I}}{\bar{I}} \quad (123)$$

where \bar{I}_x is the principal moment of inertia about the x body axis. In particular, for circular orbits it is shown that the dominant stability term (and "spring constant") is $\mathcal{O}_p^* + \beta M$.

If aerodynamic stabilization is to be feasible, then the question now becomes one of determining the attainable range of \mathcal{O}_p^* for any realistic satellite shape. For a specified orbit, \mathcal{O}_p^* becomes a function of Γ only, and hence, the problem may be restated as being one of determining the optimum proportions of a given general shape (cylinder, cone, etc.) which make the stability parameter, Γ , a maximum.

For the configurations considered henceforth, favorable center of mass locations are obtained by concentrating a homogeneous payload in the forward portion of the satellite. The aft portions of the models are assumed to be rigid, but massless, shells or skirts. It is obvious that these assumptions are not realistic, but it is hoped that the design analyses to follow will serve as guidelines for the more sophisticated cases of aerodynamically stabilized satellites.

Although many optimization procedures are available, the technique used herein is to differentiate Γ while holding payload mass (or weight) and center of mass constant. Now if the payload density is specified, then the payload volume is also known. Consequently it is convenient to non-dimensionalize Eq. (122) by multiplying both sides by the payload mass, m , while dividing both sides by the payload volume to the one-third power, $v^{1/3}$; i.e.,

$$\Gamma \frac{m}{v^{1/3}} = \frac{-C_{M0} \pi \bar{D}^3 m}{4 \bar{I} v^{1/3}} \quad (124)$$

where the right hand side is independent of m since \bar{I} is a linear function of mass. Accordingly, Eq. (124) is a function of satellite external geometry and the center of mass location. For purposes of comparing several configurations, however, the center of mass location may be conveniently written in terms of volume ratio; i.e., the ratio of payload volume to total satellite volume, including the skirt.

Since optimum geometry is to be determined from the maximization of $\Gamma(m/v^{1/3})$ and since the center of mass is specified, the gravitational parameter M is calculable and is presented in the following analyses of the various configurations. Also, it should be noted that the maximization of Γ tends to minimize \bar{I} , thereby tending to maximize M .

The body shapes chosen for the following design studies are the same as treated in Section 3.2. The basic body shapes - cylinder, sphere and cone - are analyzed separately and critically compared. The maximum Γ 's of the power law body and the truncated cone are shown to be not much different from those for the pointed cone and consequently, these bodies are not extensively compared. The hemispherical-cylinder and conical-cylinder are compared with the basic bodies which, when taken together, make these composite configurations.

1.4.5 Basic Body Shapes

1.4.5.1 Cylinder

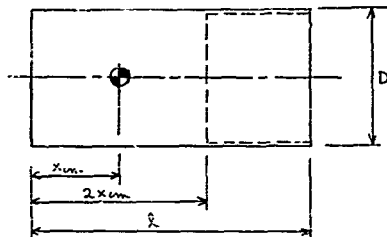


Figure 31. Cylinder Nomenclature

Neglecting the contribution of the skirt of the vehicle to its moment of inertia about the y axis, \bar{I} is found to be

$$\bar{I} = \frac{mD^2}{16} \left\{ 1 + \frac{16}{3} \left(\frac{x_{cm}}{D} \right)^2 \right\} \quad (125)$$

and for later use, the moment of inertia about the x axis is

$$\bar{I}_x = \frac{mD^2}{8} \quad (126)$$

For a cylindrical homogeneous payload

$$x_{cm}/l = 1/2 \quad \text{where} \quad (127)$$

where, of course,

$$\nu = \frac{\pi D^3 \lambda}{4} \left(\frac{\nu}{\nu_r} \right)$$

$$\frac{\nu^{3/2}}{D} = \left[\left(\frac{\nu}{\nu_r} \right) \frac{\pi \lambda}{4 D} \right]^{3/2}. \quad (128)$$

Then by using the foregoing equations for \bar{I} , x_{cm}/λ and ν and Eq. (6b) for $C_{m, \lambda}$, Eq. (12b) becomes,

$$\Gamma \frac{m}{\nu^{3/2}} = \frac{\left(16\pi \frac{\lambda}{D} \right)^{3/2} \left\{ \frac{3}{2S_{\infty}} \left[\frac{r}{T_w} \right] \frac{\lambda}{D} + 1 \right\} \left[1 - \nu/\nu_r \right]}{\left[1 + \frac{4}{3} \left(\frac{\nu}{\nu_r} \right)^2 \left(\frac{\lambda}{D} \right)^2 \right] \left(\frac{\nu}{\nu_r} \right)^{3/2}}. \quad (129)$$

Differentiating Eq. (129) with respect to λ/D and setting equal to zero yields

$$6 + 15 \left[\frac{3}{2S_{\infty}} + \frac{\pi}{2S_{\infty}} \left[\frac{T_w}{T_w} \right] \right] \left(\frac{\lambda}{D} \right)_{opt} - 16 \left(\frac{\nu}{\nu_r} \right)^2 \left(\frac{\lambda}{D} \right)_{opt}^2 - 4 \left[\frac{3}{2S_{\infty}} + \frac{\pi}{2S_{\infty}} \left[\frac{T_w}{T_w} \right] \right] \left(\frac{\nu}{\nu_r} \right)^3 \left(\frac{\lambda}{D} \right)_{opt}^3 = 0. \quad (130)$$

For orbits of interest, the two bracketed terms in Eq. () are less than unity, and using Fig. 2 for circular orbits and $T_w = 550^\circ R$, the magnitude of these terms are found to be nearly 1/3. Eq. (130) therefore becomes approximately,

$$6 + 5 \left(\frac{\lambda}{D} \right)_{opt} - 16 \left(\frac{\nu}{\nu_r} \right)^2 \left(\frac{\lambda}{D} \right)_{opt}^2 - \frac{4}{3} \left(\frac{\nu}{\nu_r} \right)^3 \left(\frac{\lambda}{D} \right)_{opt}^3 = 0 \quad (131)$$

which, for volume ratios of 1/4, 1/2, 3/4 and 1, has the graphical solutions:

$$\nu/\nu_r = 1/4 : (\lambda/D)_{opt} \cong 4.56 \quad (132)$$

$$\nu/\nu_r = 1/2 : (\lambda/D)_{opt} \cong 1.80$$

$$r/\sqrt{r} = 3/4 : (\lambda/D)_{OPT} \cong 1.08$$

$$r/\sqrt{r} = 1 : (\lambda/D)_{OPT} \cong 0.76 \quad (132) \\ \text{(cont.)}$$

Substituting the foregoing results into Eq. (129) gives the maximum values of $\Gamma(m/\sqrt{v_s})$. Moreover, if the payload density is specified, Γ_{MAX} may be found as a function of payload mass or weight. The following table summarizes these results for the case of $m/\sqrt{r} = 1/2 \text{ slug}/\sqrt{\text{ft}}^3$. Also shown are the values of the gravitational parameter, $m_1 \cong (\bar{r}_e/\bar{r}) - 1$ which correspond to the optimum fineness ratios. \bar{r} has the dimensions of ft/slug. Also, the payload weight W is evaluated at sea level for a mean acceleration of gravity of $32.2 \text{ ft}/\text{sec}^2$.

Table 1. Cylinder Summary

r/\sqrt{r}	$(\lambda/D)_{OPT}$	$(\Gamma \frac{m}{\sqrt{v_s}})_{MAX}$	$(\Gamma m^{3/2})_{MAX}$	$(\Gamma W^{3/2})_{MAX}$	M
1/4	4.56	41.1	51.7	522	-0.269
1/2	1.80	7.7	12.3	124	-0.036
3/4	1.08	2.86	3.61	35.4	+0.070
1	0.76	0	0	0	+0.133

The results shown in Table 1 (except for $r/\sqrt{r} = 1.0$) are presented as plots of Γ versus payload weight in Figs. 35, 36, and 37. The significant features of these results are discussed in Section 3.4.2.1.

¹The payload density of $1/2 \text{ slug}/\text{ft}^3$ represents a reasonable average of U.S. satellite payloads launched to date.

3.4.2.2 Sphere

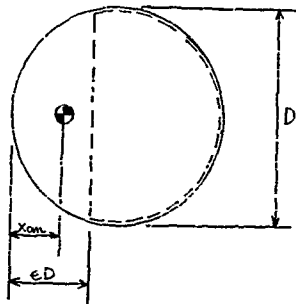


Figure 32. Sphere Nomenclature

Since the "fineness ratio" of a sphere is obviously unity, there is no need to maximize the stability parameter Γ for a given volume ratio. In order to form $\Gamma(m/r^{1/2})$ and Γ , however, it is necessary to determine the pitching moment of inertia, \bar{I} . A laborious but elementary integration yields for this quantity,

$$\bar{I} = \frac{3}{2} \frac{mD^2 \epsilon}{(3-2\epsilon)^2} \left\{ 1 - \frac{11}{6} \epsilon + \frac{6}{5} \epsilon^2 - \frac{3}{10} \epsilon^3 \right\} \quad (133)$$

where the mass of the spherical shell aft of the payload is neglected. For a homogeneous spherical segment,

$$\frac{x_{cm}}{D} = \frac{2\epsilon - \frac{3}{2} \epsilon^2}{3-2\epsilon} \quad (134)$$

The following geometrical relationships are also useful.

$$r/r_T = \epsilon^2 (3 - 2\epsilon)$$

$$\frac{r^{1/3}}{D} = \left[\frac{\pi(r)}{6(r_T)} \right]^{1/3} \quad (135)$$

Moreover, the moment of inertia about the X axis is,

$$\bar{I}_x = \frac{mD^2\epsilon}{(3-2\epsilon)} \left\{ 1 - \frac{3}{2}\epsilon + \frac{3}{5}\epsilon^2 \right\} \quad (136)$$

which when combined with Eq. (133) leads to

$$M \equiv \frac{\bar{I}_x}{\bar{I}} - 1 = \frac{1 - \frac{5}{2}\epsilon + 2\epsilon^2 - \frac{1}{2}\epsilon^3}{1 - \frac{11}{6}\epsilon + \frac{6}{5}\epsilon^2 - \frac{3}{10}\epsilon^3} \quad (137)$$

Substituting Eq. (69) for $C_{m\alpha}$ and Eq. (133) for \bar{I} into Eq. (124) yields

$$\frac{r}{r^{1/3}} = \frac{\left[2Q(\epsilon_m) + \frac{2\pi}{3S_\alpha} \left| \frac{r}{r_m} \right| \right] \left(\frac{1}{2} - \frac{x_{cm}}{D} \right) \left(\frac{\pi}{6} \right)^{2/3}}{\left(\frac{r}{r_T} \right)^{1/3} \frac{\epsilon}{(3-2\epsilon)^2} \left(1 - \frac{11}{6}\epsilon + \frac{6}{5}\epsilon^2 - \frac{3}{10}\epsilon^3 \right)} \quad (138)$$

where the geometrical terms are all functions of r/r_T since $x_{cm}/D = f(\epsilon) = f(r/r_T)$. The term in the brackets may be estimated using Eq. (50) and Fig. 2, and consequently has a value near 2.14. Although Eq. (138) may be written in terms of r/r_T , the lengthy expression is quite cumbersome.

It is more feasible to construct plots of x_{cm}/D and r/r_T versus the depth ratio ϵ . Accordingly, these curves are shown in Fig. 3) along with variation of the gravitational parameter M . It is noted that for all possible values of ϵ , $M \geq 0$ and hence the gravitational torques always augment the aerodynamic torques in the case of a "loaded" sphere.

Table 2 presents a summary of the aerodynamic parameters developed above. Here again, the payload density is assumed to be $1/2$ slug/ft³. Discussion of the results and comparisons with the cylinder and cone are noted in Section 3.4.2.4 and Figs. 35, 36 and 37.

Table 2. Sphere Stowary

γ/γ_T	ϵ	x_{cm}/D	$\Gamma^m/\gamma^{1/3}$	$\Gamma^m/3$	$\Gamma^1 W^{2/3}$	M
1/4	.326	.205	21.9	27.6	279	.740
1/2	.500	.3125	7.40	9.32	94.1	.542
3/4	.674	.399	2.95	3.72	37.5	.327
1	1.0	.500	0	0	0	0

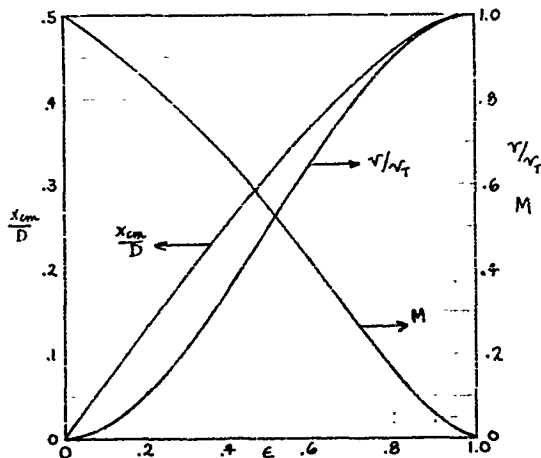


Figure 33. Sphere Inertia and Volume Characteristics

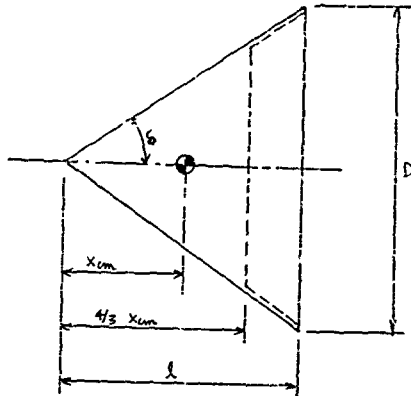
3.4.2.3 Cone

Figure 34. Cone Nomenclature

For the conical configuration shown in Fig. 34, the moment of inertia about the pitch (or yaw) axis is found to be

$$\bar{I} = \frac{4}{15} m l^2 \left(\frac{x_{cm}}{l} \right)^2 \left[\frac{1}{4} + \tan^2 \alpha \right] = \frac{m D^2}{60} \left(\frac{x_{cm}}{l} \right)^2 (4 + \cot^2 \alpha) \quad (139)$$

where the mass of the skirt is, as before, neglected. Likewise, for a homogeneous payload,

$$\frac{x_{cm}}{l} = \frac{3}{4} \left(\frac{v}{v_T} \right)^{1/3} \quad (140)$$

$$v = \frac{\pi D^3}{24} \cot \alpha \left(\frac{v}{v_T} \right)$$

$$\frac{v^{1/3}}{D} = \left[\frac{\pi \cot \alpha}{24} \left(\frac{v}{v_T} \right) \right]^{1/3}$$

Furthermore it is easy to show that

$$\bar{I}_x = \frac{2}{15} m D^2 \left(\frac{x_{cm}}{l} \right)^2$$

which leads to

$$M = \frac{4 - \cot^2 \delta}{4 + \cot^2 \delta} \quad (141)$$

Following the procedure used for the cylinder and sphere, Eqs. (73), (139), and (140) may be substituted into Eq. (124); i.e.,

$$\Gamma \frac{m}{r^{1/2}} = \frac{640 \left(\frac{\pi}{24} \cot^2 \delta \right)^{2/3}}{3 \left(\frac{r}{r_T} \right) (4 + \cot^2 \delta)} \left\{ 3 \left[1 - \frac{3}{4} \left(\frac{r}{r_T} \right)^{1/3} \right] \right. \\ \left. + \frac{\sqrt{\pi} \sqrt{\Gamma_m / T_m}}{2 \Sigma_m \sin \delta} \left[1 - \frac{9}{8} \left(\frac{r}{r_T} \right)^{1/3} \cos^2 \delta \right] \right\} \quad (142)$$

The question now becomes one of determining the optimum cone angle δ which renders Eq. (142) maximum for a given volume ratio. The temperature-dependent term in Eq. (142) obviously complicates the maximization process. As may be seen in Fig. 25, however, this term is small when compared with the first term, and consequently, contributes very little in the determination of an optimum cone angle. Then, by neglecting the temperature term and differentiating Eq. (142) with respect to δ , and setting equal to zero yields,

$$2 \left(\frac{\delta}{D} \right)_{opt} = \cot \delta_{opt} = \sqrt{2} \quad (143)$$

which is independent of volume ratio. The substitution of Eq. (143) into Eq. (142) gives the maximum (nearly) value of $\Gamma m / r^{1/2}$; i.e.,

$$\left(\Gamma m/r^{1/2}\right)_{\max} \cong \frac{11.55 \left[3 + \frac{\sqrt{3}\pi}{2 S_m} \sqrt{\frac{I_w}{T_m}} \right] \left[1 - \frac{3}{4} \left(\frac{r}{r_T} \right)^{1/2} \right]}{\frac{r}{r_T}} \quad (144)$$

Using Fig. 2 for a representative value of $(1/S_m) \sqrt{I_w/T_m}$, Eq. (144) reduces to

$$\left(\Gamma m/r^{1/2}\right)_{\max} \cong 35.8 \left[1 - \frac{3}{4} \left(\frac{r}{r_T} \right)^{1/2} \right] / \left(\frac{r}{r_T} \right) \quad (145)$$

Furthermore, the optimum cone angle, Eq. (143), may be substituted in Eq. (141) to give

$$M \cong 1/2 \quad (146)$$

which is positive and stabilizing. The foregoing results are summarized in Table 3 and Figs. 35 through 39 for volume ratios of 1/4, 1/2, 3/4 and 1 and for the case of $m/r = 1/2 \text{ slug/ft}^2$.

Table 3. Cone Summary

r/r_T	δ_{OPT}	x_{cm}/l	$(\Gamma r/v^{1/2})_{\max}$	$(\Gamma m^{3/2})_{\max}$	$(\Gamma W^{3/2})_{\max}$	M
1/4	35.3°	0.473	75.5	95.2	964	0.333
1/2	35.3°	0.595	29.0	36.5	362	0.333
3/4	35.3°	0.681	15.25	19.2	194	0.333
1	35.3°	0.750	8.95	11.3	114	0.333

3.4.2.4 Comparison of Basic Body Shapes

Now that the stability parameters of three basic satellite shapes have been calculated, it is desirable to analyze the advantages and disadvantages of each configuration from the point-of-view of maximizing stability for a specified payload condition. The principle used in the

preceding sections is to optimize Γ while holding the payload volume (or mass) constant, and then observe the variation of this maximum as the center of mass and payload weight of each configuration are varied. In other words, the question may be asked, "Which configuration has the most aerodynamic stability for a given payload weight and center of mass?" This form of optimization, however, does not completely solve the problem in that maximum Γ for a specified payload volume (or mass) and center of mass also specifies the diameter of the satellite. Consequently, the preferred configuration from a stability viewpoint may have a prohibitively large diameter.

The results of the stability analyses of the three basic body shapes are shown plotted in Figs. 35 through 38 for the four volume ratios. Since fully loaded homogeneous cylinders and sphere are neutrally stable, only the cone appears in Fig. 38 for $r/\sqrt{V} = 1.0$. Also shown are integer values of satellite diameter along each maximum Γ line. In Figs. 36 and 37, values of Γ for constant diameter are shown to illustrate the deviation from the optimum Γ . These curves clearly show the difference between maximum Γ for constant diameter and maximum Γ for constant mass (except for sphere). It may be seen from Figs. 35, 36 and 37 that the cone has the most aerodynamic stability for a given payload weight, while the sphere has the least or nearly the least. The cone, however, also has the largest diameter for a given payload weight. For example, consider $r/\sqrt{V} = 1/2$ and a weight of 300 lbs. (Fig. 36). The optimum cone is about 6 feet in diameter while the cylinder is only 3 ft. The sphere, which has the least stability, requires a 4 ft. diameter.

Now suppose there is a requirement that the satellite be no larger than 3 ft. in diameter. Then at these conditions ($W = 300$ lbs., $r/\sqrt{V} = 1/2$, $D = 3$ ft.) the cylinder now appears the most stable. In fact, the 2 ft. cylinder is better than the 3 ft. cone. At $r/\sqrt{V} = 3/4$ and $W = 300$ lbs. (Fig. 37) the optimum cone has a diameter near 5 ft., while the cylinder is still near 3 ft. The sphere, which is slightly more stable than the cylinder for this volume ratio, is about 3-1/2 ft. in diameter. If a 3 ft. minimum diameter must be held for the $r/\sqrt{V} = 3/4$ case, however, the cone has the most stability. If the length of the satellite is no problem, this example may be carried still further. That is, for $r/\sqrt{V} = 1/4$ (Fig. 35) the 300 lb. payload may be carried by a cylindrical satellite of less than 3 ft diameter. Furthermore, the value of Γ for this case is considerably higher, as expected, than for the other cases with higher volume ratios.

A few words are appropriate about the combined stability due to aerodynamic and gravitational effects; more specifically, the quantities Q_p^* and $3M$. Because of the basic difference between Q_p^* and $3M$, a combination of these parameters is impractical to optimize analytically. Q_p^* , however, is a function of Γ and the orbit conditions, and therefore, maximum Γ maximizes Q_p^* for a given orbit. Furthermore, it is

desirable to keep M positive (low fineness ratio) to augment the aerodynamic stability. In the examples above, or in Figs. 35, 36 and 37, both the sphere and optimum cone have positive values of M , while for the optimum cylinder, M is near zero or negative. Consequently, before one selects a satellite shape based on maximum aerodynamic stability, the effects of gravitational torques should be considered. As shown before, the balance between aerodynamic and gravitational effects depends on the orbit conditions as well as the satellite shape, and that maximum aerodynamic stability certainly does not necessarily prevent unstable motions at all near-Earth orbit conditions. These latter observations are particularly true at higher altitudes where the values of ρ^* may become small, owing to the decreased atmospheric density.

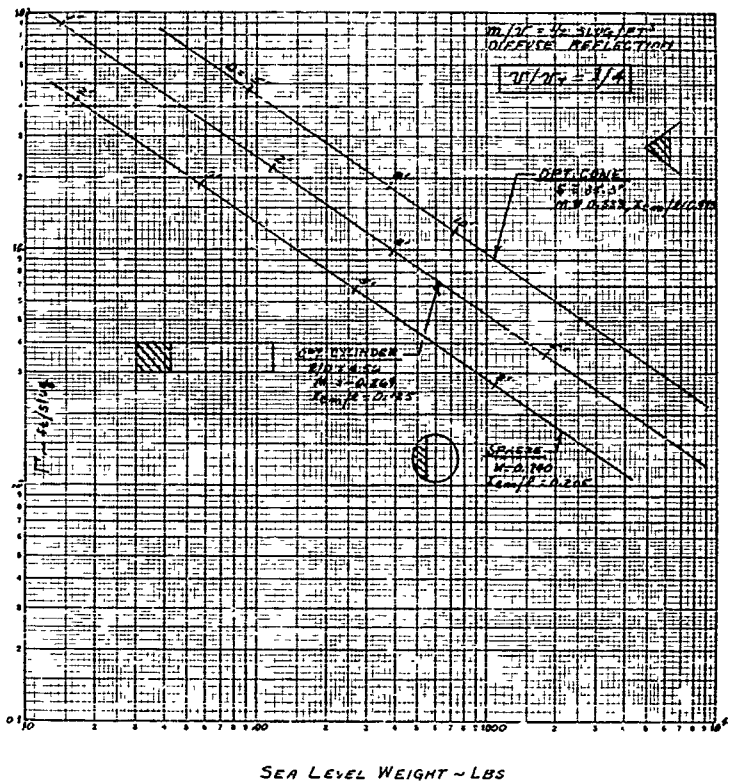
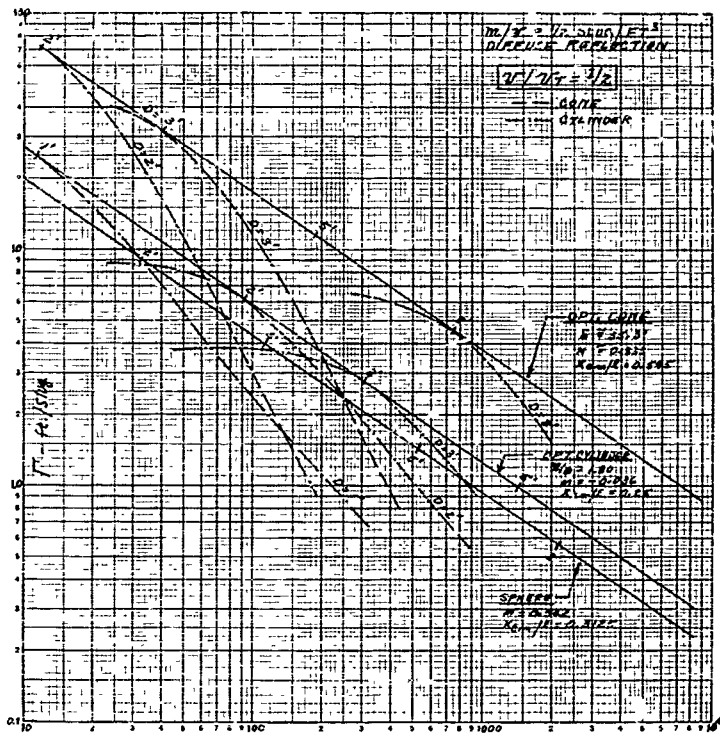


Figure 35. Comparison of Basic Body Shapes - $\sqrt{V/C} = 1/4$

Figure 36. Comparison of Basic Body Shapes - $m/V = 1/2$

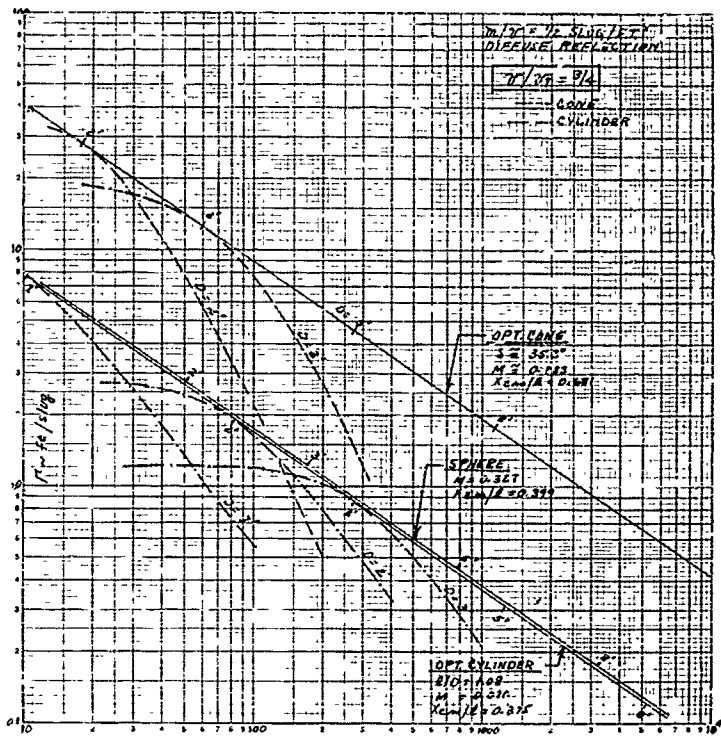
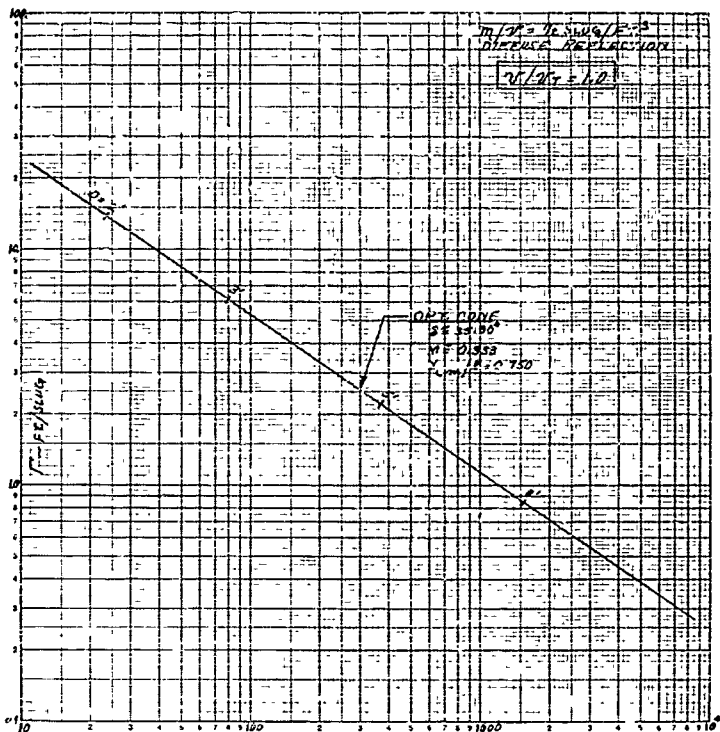


Figure 37. Comparison of Basic Body Shapes - $\sqrt{V_e} = 3/4$



SEA LEVEL WEIGHT ~ 75.

Figure 38. Comparison of Body Shapes - $\rho/\rho_f = 1$

3.4.3 Complex Body Shapes

3.4.3.1 Power Law Body

Following the analyses of previous body shapes, the static stability parameter $\Gamma_m/r^{3/2}$ as well as Γ and M will be examined for the power law body. As before, the body will be assumed composed of a hollow, massless skirt with a homogeneous payload as shown in Fig. 39.

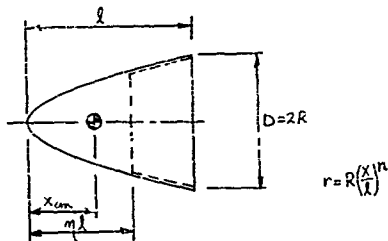


Figure 39. Power Law Body Nomenclature

The moments of inertia of a power law body may be determined as

$$\bar{I} = mD^2 \eta^2 \frac{(2n+1)}{4} \left[\frac{\eta^{2n-2}}{4(4n+1)} + \frac{(\ell/D)^2}{(2n+3)(n+1)^2} \right]$$

$$\bar{I}_x = \frac{mD^2 \eta^{2n} (2n+1)}{8(4n+1)} \quad (247)$$

$$M \equiv \frac{\bar{I}_x - \bar{I}}{\bar{I}} = \frac{(2n+3)(n+1)^2 \eta^{2n-2} - 4(4n+1)(\ell/D)^2}{(2n+3)(n+1)^2 \eta^{2n-2} + 4(4n+1)(\ell/D)^2}$$

and the pertinent geometric relationships are

$$\frac{\kappa \omega}{\xi} = \frac{2n+1}{2n+2} \eta$$

$$\frac{\gamma}{\gamma_T} = \gamma^{2n+1}$$

$$\gamma_T = \frac{\pi D^2 \xi}{4(2n+1)} \quad (148)$$

$$\frac{\gamma^{1/3}}{D} = \left[\left(\frac{\gamma}{\gamma_T} \right) \frac{\pi}{4(2n+1)} \left(\frac{\xi}{D} \right) \right]^{1/3}$$

Using the approximate pitching moment slope, Eq. (16), in which the temperature dependent term is neglected, the aerodynamic stability parameter $\Gamma_m / \gamma^{1/3}$ in terms of volume and mass parameters is

$$\Gamma_m / \gamma^{1/3} \cong \frac{16 \left[\frac{\pi}{4} \frac{1}{(2n+1)} \frac{\xi}{D} \right]^{2/3} \left[2(n+1) - (2n+1) \left(\frac{\gamma}{\gamma_T} \right)^{1/3} \right]^{1/3} (4n+1)(2n+3)(n+1)}{\left(\frac{\gamma}{\gamma_T} \right)^{2n+1} \left[\left(\frac{\gamma}{\gamma_T} \right)^{2n-2} (2n+3)(n+1)^2 + 4(4n+1) \left(\frac{\xi}{D} \right)^2 \right]} \quad (149)$$

The optimum fineness ratio for maximum stability for a given payload volume or mass may be found by differentiating Eq. (149) with respect to ξ/D and setting equal to zero. This operation yields

$$\left(\xi/D \right)_{opt} \cong \left(\frac{n+1}{2} \right) \left(\frac{\gamma}{\gamma_T} \right)^{\frac{n-1}{2n+1}} \sqrt{\frac{2n+3}{2(4n+1)}} \quad (150)$$

and when this equation is substituted into the last of Eqs. (147), the inertia parameter M becomes

$$M \approx 1/3 \quad (151)$$

which is independent of body curvature and volume ratio.

Substituting Eq. (150) into Eq. (149) gives the approximate maximum values of $\Gamma m/r^{1/3}$ for given payload volume or mass. Plots of Eq. (149), using Eqs. (148), are shown in Fig. 40. It may be seen that the value of the exponent has little effect on maximum stability for given volume ratio. It should be remembered, however, that although the curves in Fig. 40 may be extrapolated to $n=0$ (cylinder), they become invalid at $n=0$; i.e., Eq. (140) applies only for $0 < n \leq 1$. The exact cylinder values for $(\Gamma m/r^{1/3})_{\max}$ are shown on the ordinate. The difference between the extrapolated values and exact cylinder values is due to a discontinuous shift of force center as a decreasing ($n \rightarrow 0$) power law body suddenly becomes a flat-faced cylinder. Also shown are the more accurate values of $(\Gamma m/r^{1/3})_{\max}$ for the $n=1$ (cone) and $n=1/2$ bodies; i.e., including the temperature term in the solution of Eq. (75).

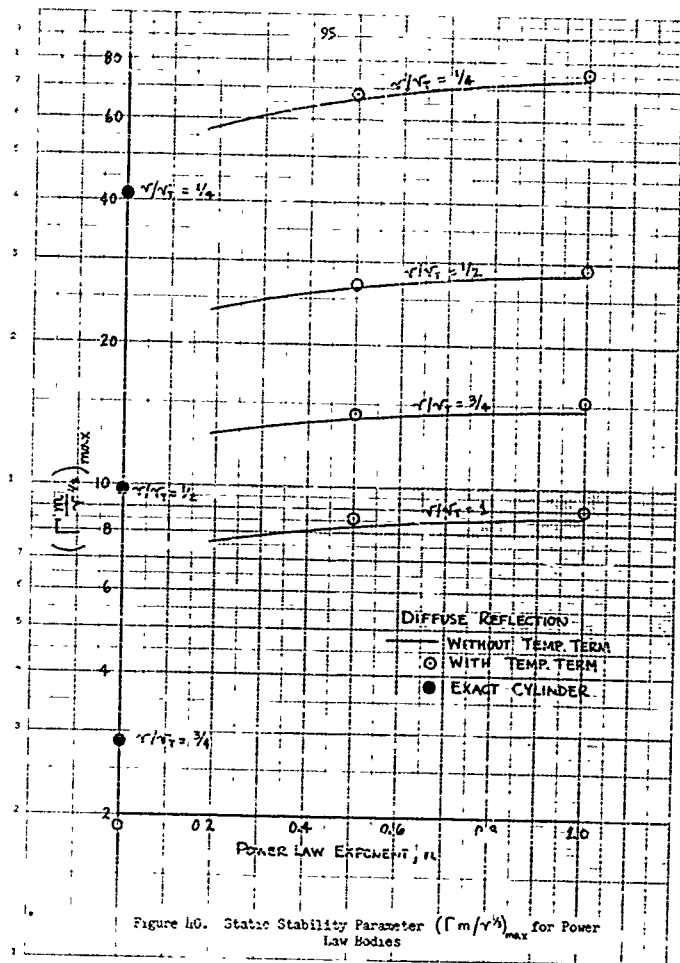
It also appears from Fig. 40 that the value of n which gives maximum $\Gamma m/r^{1/3}$ is something greater than unity. Since n greater than unity represents a body with a concave surface, these configurations cannot logically be treated using conventional free-molecule theory. That is, the basic assumption of free-molecule theory, as applied to gasdynamic calculations, is that the incident momentum flux is not disturbed by the presence of the body. Regardless of this difficulty, however, the "flatness" of the curves in Fig. 40 indicates that the optimum body probably does not have much more stability than the cone ($n=1$).

Table 4 shows the various maximum stability parameters along with $(H/D)_{\text{opt}}$, and x_{cm}/l as calculated from Eqs. (14c), (149) and (150). W is the sea level weight, $m/r = 1/2 \text{ slug/ft}^3$, and Γ is in ft/slug . From Eq. (151) the inertia parameter M is approximately $1/3$ for all power law bodies.

Table L. Power Law Body Summary

n	r/\sqrt{r}	$(\Delta D)_{OPT}$	X_{cm}/k	$(\Gamma m/r^{3/2})_{MAX}$	$(\Gamma m^{2/3})_{MAX}$	$(\Gamma W^{2/3})_{MAX}$
1/4	1/4	1.17	.238	59.0	74.4	752
	1/2	.927	.365	24.1	30.4	302
	3/4	.675	.495	13.05	16.45	166
	1	.585	.600	7.77	9.80	99
1/2	1/4	.866	.333	66.1	83.2	842
	1/2	.728	.471	26.2	33.0	334
	3/4	.659	.578	13.9	17.5	177
	1	.612	.667	8.26	10.4	105
3/4	1/4	.753	.410	70.2	88.5	891
	1/2	.704	.541	28.0	35.3	357
	3/4	.675	.636	14.5	18.2	184
	1	.656	.714	8.51	10.7	109
1	1/4	.707	.473	73.0	92.0	928
	1/2	.707	.595	28.1	35.4	358
	3/4	.707	.681	14.65	18.5	187
	1	.707	.750	8.66	10.9	110

It may be noticed that the values for $n=1$ (cone) in Table L are slightly ($\approx 4\%$) less than the cone values shown in Section 3.4.2.3. This difference is again due to the negligence of the temperature dependent term in Eq. (75) for $C_{m\alpha}$.



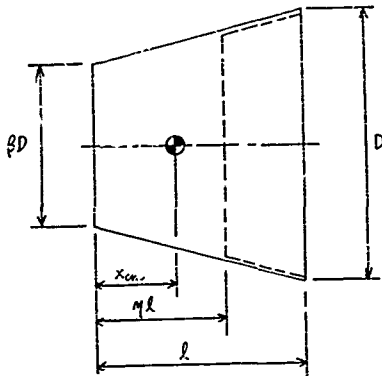
3.b.3.2 Truncated Cone

Figure 42. Truncated Cone Nomenclature

For the case of a "loaded" truncated cone, the pitch and roll moments of inertia about the center of mass are functions of the diameter ratio, β , as well as the payload length ratio, η . Consequently it is not difficult to show that

$$\bar{I} = \frac{3mD^2}{80} \left\{ \frac{C + B(l/D)^2}{3\beta^2 + 3\eta\beta(1-\beta) + \eta^2(1-\beta)^2} \right\} \quad (152)$$

$$\bar{I}_x = \frac{3mD^2}{40} \left\{ \frac{C}{3\beta^2 + 3\eta\beta(1-\beta) + \eta^2(1-\beta)^2} \right\}$$

$$M = \frac{C - B(l/D)^2}{C + B(l/D)^2}$$

where

$$C \equiv \eta^4(1-\beta)^4 + 5\eta^3\beta(1-\beta)^3 + 10\eta^2\beta^2(1-\beta)^2 + 10\eta\beta^3(1-\beta) + 5\beta^4$$

$$B \equiv 20\eta^2 \left\{ \frac{4}{5}\eta^2(1-\beta)^2 + 5\eta\beta(1-\beta) + \frac{4}{3}\beta^2 \right. \\ \left. - \left(\frac{x_{cm}}{l}\right)^2 \frac{1}{\eta^2} \left[\frac{4}{3}\eta^2(1-\beta)^2 + 4\eta\beta(1-\beta) + 4\beta^2 \right] \right\} \quad (153)$$

and where

$$\frac{x_{cm}}{l} = \frac{3}{4}\eta \left[\frac{\eta^2(1-\beta)^2 + \frac{8}{3}\eta\beta(1-\beta) + 2\beta^2}{\eta^2(1-\beta)^2 + 3\eta\beta(1-\beta) + 3\beta^2} \right] \quad (154)$$

Likewise, the other geometrical properties may be expressed as

$$\frac{V}{V_T} = \eta \left[\frac{\eta^2(1-\beta)^2 + 3\eta\beta(1-\beta) + 3\beta^2}{1 + \beta + \beta^2} \right]$$

$$r_T = \frac{\pi l D^2}{12} \left[1 + (\beta + \beta^2) \right] \quad (156)$$

$$\frac{r^{1/3}}{D} = \left\{ \frac{\pi}{12} \frac{l}{D} \eta \left[\eta^2(1-\beta)^2 + 3\eta\beta(1-\beta) + 3\beta^2 \right] \right\}^{1/3}$$

The first of Eqs. (156) may be solved for η in terms of β and the volume ratio; i.e.,

$$\eta = \frac{1}{1-\beta} \left\{ \left[\beta^3 + \frac{r}{r_T} (1-\beta^3) \right]^{1/3} - \beta \right\} \quad (157)$$

Eqs. (154) and (157) may be used, if desired, for rewriting the equations for $C_{m\alpha}$ and $\bar{\Gamma}$ in terms of β , λ/D , and τ/τ_T . The resulting expressions, however, are unwieldy for rapid numerical calculations. Therefore, the stability parameter Γ^* , as defined before, will now be written using only Eqs. (80), (152) and (156). The resulting combination yields

$$\Gamma^* \frac{m}{r^{3/2}} \cong \frac{160 \left[\frac{\pi \lambda}{16AD} \left(\frac{\tau}{\tau_T} \right) (1 + \beta + \beta^2) \right]^{3/2} \left[1 - \frac{\lambda_{cm}}{L} \right]}{\eta \left[C + B \left(\beta/D \right)^2 \right]} \quad (158)$$

For given volume and diameter ratios, the approximate optimum fineness ratio, λ/D , which gives maximum stability, may be found by differentiating Eq. (158) with respect to λ/D , setting equal to zero, and solving for λ/D . The resulting expression is

$$\left(\lambda/D \right)_{OPT} \cong \sqrt{\frac{1}{2} \frac{C}{B}} \quad (159)$$

Furthermore, Eq. (152) combines with the last of Eqs. (152) to give the optimum value of the inertia parameter M ; i.e.,

$$M \cong 1/3 \quad (160)$$

which is the same as for pointed cones and power law bodies. The maximum value of $\Gamma^* m/r^{3/2}$ may now be found by substituting Eq. (159) into Eq. (158). As mentioned above, C , B , λ_{cm}/L , and η are only functions of diameter ratio β and volume ratio τ/τ_T ; and hence, the maximum $\Gamma^* m/r^{3/2}$ depends only on these ratios.

Fig. 42 presents plots of Eq. (158) using Eq. (159) for various values of the volume ratio. As in the case of power-law bodies, the curves are not extended to the cylinder abscissa ($\beta = 1.0$) since the equations for $C_{m\alpha}$ used herein are invalid for cylinders. The exact cylinder values for $(\Gamma^* m/r^{3/2})_{MAX}$, however, are shown on the ordinate. Moreover, representative values of the more exact $(\Gamma^* m/r^{3/2})_{MAX}$ are also shown using $C_{m\alpha}$ from Eq. (79) with $S_{\alpha} \cong 7$ and $(1/S_{\alpha}) \bar{\Gamma}_{max}/\bar{\Gamma}_{\alpha} \cong .065$ from Fig. 2. It may be seen that the approximation of Eq. (80) is in very little error. It also appears from Fig. 42 that maximum $\Gamma^* m/r^{3/2}$ occurs for configurations with non-zero diameter ratios, which is, in fact,

significant and useful development. Then for a specified payload volume or mass requirement, the pointed, conical satellite does not represent the most stable configuration as originally suspected. The blunted cone also represents a more useful shape from the viewpoint of re-entry, payload packaging, and/or antenna design.

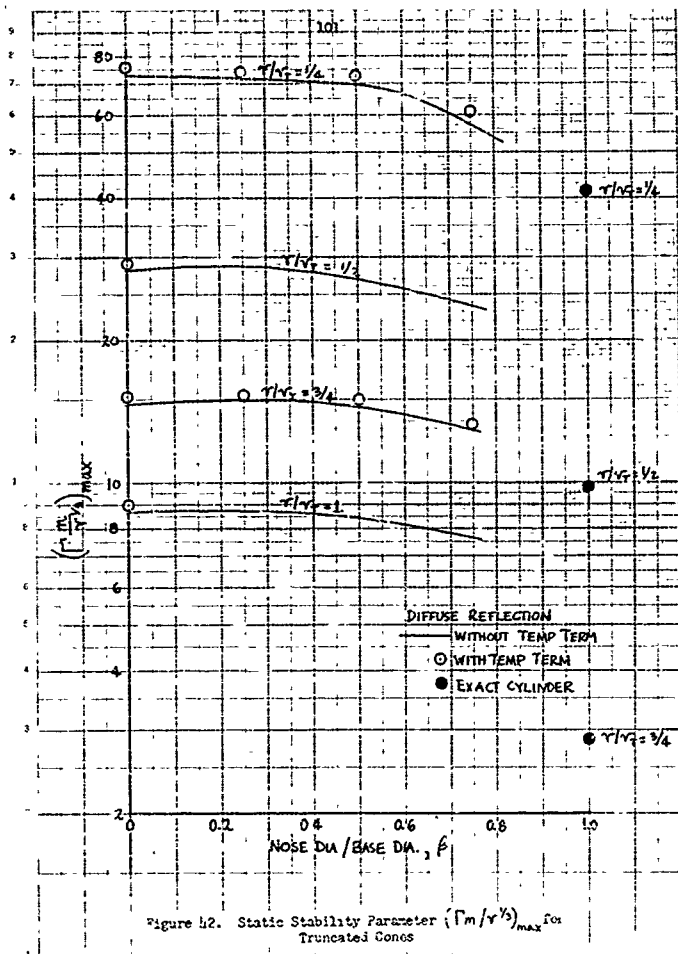
The results of the stability analysis of the truncated cone are summarized in Table 5. Here again, the payload density is taken as $1/2$ slug/ft³.

Table 5. Truncated Cone Summary

β	r/r_T	$(L/D)_{OPT}$	x_{cm}/L	$(\Gamma_m/r^2)_{max}$	$(\Gamma_m^{3/2})_{max}$	$(\Gamma W^{3/2})_{max}$
0	1/4	.707	.473	73.0	92.0	950
	1/2	.707	.595	28.1	35.4	358
	3/4	.707	.581	14.65	18.5	187
	1	.707	.750	6.66	10.9	110
1/4	1/4	.660	.338	71.4	90.0	911
	1/2	.600	.480	28.8	36.3	367
	3/4	.576	.590	14.8	18.65	189
	1	.568	.673	8.69	10.95	111
1/2	1/4	.952	.222	69.2	87.2	882
	1/2	.670	.380	27.0	34.0	344
	3/4	.580	.502	14.5	18.3	185
	1	.528	.607	8.41	10.6	107
3/4	1/4	1.55	.160	57.0	71.8	726
	1/2	.890	.302	23.6	29.7	301
	3/4	.665	.420	12.95	16.5	165
	1	.552	.548	7.64	9.64	97.2

It should be re-emphasized that the pointed cone values are slightly less than the cone values in Table 5 due to the omission of the temperature term in Eq. (19) for $C_{m\alpha}$.

Before concluding this section it should be noted that there is a definite similarity between the results of the power law body and the truncated cone. In particular if β is replaced by $i-n$ (n equals exponent), the first two terms of Taylor expansions of the body profiles about the point $x/l = 1$ are identical. This similarity may be noted by comparing the values of $(\Gamma m/\nu^{1/2})_{max}$ for a given ν/ν_T in Figs. 10 and 12.



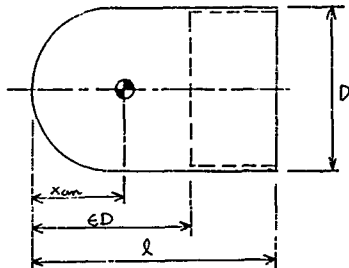
3.4.3.3 Hemisphere-Cylinder

Figure 43. Hemisphere-Cylinder Nomenclature

As in the problem of determining the pitching moment slope, the calculation of the inertia and geometrical characteristics of the hemisphere-cylinder is considerably more complicated than for the basic shapes. The parameters shown below are written for the two conditions of the payload fineness ratio ϵ greater than and less than $1/2$. Since the skirt is assumed massless, the sphere equations of Section 3.4.2.2 may be utilized for $\epsilon \leq 1/2$. Consequently, it is not difficult to show that

$$\bar{I} = \frac{\frac{3}{2} m D^2 \epsilon}{(3-2\epsilon)^2} \left\{ 1 - \frac{11}{6} \epsilon + \frac{6}{5} \epsilon^2 - \frac{3}{10} \epsilon^3 \right\} \quad [\epsilon \leq 1/2] \quad (162)$$

$$\bar{I} = \frac{m D^2}{320(\epsilon-1)^2} \left\{ 31 - 336\epsilon + 960\epsilon^2 - 640\epsilon^3 + 960\epsilon^4 \right\} \quad [\epsilon \geq 1/2]$$

and

$$\bar{I}_x = \frac{mD^3 \epsilon}{(3-2\epsilon)} \left\{ 1 - \frac{3}{2}\epsilon + \frac{3}{5}\epsilon^2 \right\} \quad [\epsilon \leq 1/2]$$

$$\bar{I}_x = \frac{mD^3}{4(6\epsilon-1)} \left\{ 3\epsilon - \frac{1}{10} \right\} \quad [\epsilon \geq 1/2] \quad (162)$$

which may be combined to give

$$M = \frac{1 - \frac{5}{2}\epsilon + 2\epsilon^2 - \frac{1}{2}\epsilon^3}{1 - \frac{11}{6}\epsilon + \frac{6}{5}\epsilon^2 - \frac{3}{10}\epsilon^3} \quad [\epsilon \leq 1/2]$$

$$M = \frac{25 - 240\epsilon + 480\epsilon^2 + 640\epsilon^3 - 960\epsilon^4}{31 - 336\epsilon + 960\epsilon^2 - 640\epsilon^3 + 960\epsilon^4} \quad [\epsilon \geq 1/2]. \quad (163)$$

The results of the sphere analysis lead to

$$\frac{x_{cm}}{D} = \frac{\epsilon(4-3\epsilon)}{2(3-2\epsilon)} \quad [\epsilon \leq 1/2]$$

$$\frac{x_{cm}}{D} = \frac{24\epsilon^2 - 1}{8(6\epsilon - 1)} \quad [\epsilon \geq 1/2]. \quad (164)$$

The total fineness ratio and payload volume may also be written in terms of the payload fineness ratio; i.e.,

$$\frac{l}{D} = \frac{\frac{2}{3}\epsilon^2(3-2\epsilon)}{\sqrt{r/r_T}} + \frac{1}{6} \quad \left[\begin{array}{l} \lambda/D \geq 1/2 \\ \epsilon \leq 1/2 \end{array} \right]$$

$$\frac{l}{D} = \frac{\epsilon - 1/6}{\sqrt{r/r_T}} + \frac{1}{6} \quad \left[\begin{array}{l} \lambda/D \geq 1/2 \\ \epsilon \geq 1/2 \end{array} \right] \quad (165)$$

and

$$r = \frac{\pi D^3}{6} \epsilon^2 (3-2\epsilon) \quad [\epsilon \leq 1/2]$$

$$r = \frac{\pi D^3}{24} (6\epsilon - 1) \quad [\epsilon \geq 1/2]. \quad (166)$$

The stability parameter Γ and its alternate forms may now be formulated using Eq. (81) for C_{max} and the foregoing Eqs. (161), (164) and (166). If desired Eqs. (165) may be solved for ϵ in terms of λ/D and r/r_T and then substituted in the equations for \bar{I} , κ_{om}/D and r . As in the cases of the sphere and truncated cone, however, the resulting expressions do not necessarily simplify the problem. Consequently, $\Gamma_m/r^{1/3}$ is written here as,

$$\Gamma_m/r^{1/3} = \frac{\left[\frac{\pi}{6} \epsilon^2 (3-2\epsilon) \right]^{2/3} \left[X(3-2\epsilon) - Y\epsilon(2-\frac{3}{2}\epsilon) \right]}{\epsilon^3 \left[1 - \frac{11}{6}\epsilon + \frac{6}{5}\epsilon^2 - \frac{3}{10}\epsilon^3 \right]} \quad [\epsilon \leq 1/2]$$

$$(167)$$

$$\Gamma_m/r^{1/3} = \frac{240 \left[\frac{\pi}{24} (6\epsilon - 1) \right]^{2/3} \left[8X(6\epsilon - 1) - Y(24\epsilon^2 - 1) \right]}{31 - 336\epsilon + 540\epsilon^2 - 640\epsilon^3 + 960\epsilon^4} \quad [\epsilon \geq 1/2]$$

where X and Y are defined by Eqs. (85). If S_{∞} and $(V/S_{\infty})\sqrt{\Gamma/\Gamma_0}$ are represented by the typical values in Fig. 2, then X and Y are approximately

$$\begin{aligned} X &\approx 0.340(l/D)^2 + (l/c) \cdot 0.481 \\ Y &\approx 0.680(l/c) + 1.793 \end{aligned} \quad (168)$$

where it is understood that l/D is always greater than $1/2$. Moreover, it should be re-emphasized that ϵ , in Eqs. (167), is a function of l/D and r/r_T . For reference, the solutions of Eqs. (165) are

$$\begin{aligned} \epsilon &= \cos \left\{ \cos^{-1} \left[1 - 3 \left(\frac{r}{r_T} \right) \left(\frac{l}{D} - \frac{1}{2} \right) \right] + 240^\circ \right\} + \frac{1}{2} \quad \left[\epsilon \leq \frac{1}{2} \right] \\ \epsilon &= \frac{r}{r_T} \left(\frac{l}{D} - \frac{1}{2} \right) + \frac{1}{2} \quad \left[\epsilon \geq \frac{1}{2} \right]. \end{aligned} \quad (169)$$

Because of the obvious difficulties involved in differentiating Eqs. (167) with respect to l/D , setting equal to zero, and solving for $(l/D)_{OPT}$, no attempt has been made to analytically determine the maximum value of $\Gamma m/r^2$ for hemisphere-cylinders with total fineness ratios greater than $1/2$. The stability parameter Γ , however, may be plotted against payload weight for constant values of m/r , r/r_T and either l/D or D . Constant l/D curves are presented in Figs. 44, 45 and 46 for the usual $m/r = 1/2$ and r/r_T equal $1/4$, $1/2$ and $3/4$. The examples chosen are the limiting case of $l/D = 1/2$ which is a hemisphere, and $l/D = 3/4$ which is equivalent to the complete sphere with the same payload volume ratio. Curves of constant diameter ($= 2$ feet) are also shown in Figs. 44, 45, and 46 for the three volume ratios. Since l/D varies along the constant diameter curves, a graphical solution for maximum $\Gamma m/r^2$, and hence $(l/D)_{OPT}$, may be possible. Such a solution is shown in Fig. 44 for $r/r_T = 1/4$ in which the optimum fineness ratio appears to be near 4.5. The corresponding optimums for the other volume ratios, $1/2$ and $3/4$, are not apparent.

Included in the comparisons of the hemisphere-cylinders are a basic sphere and optimum flat-faced cylinder. Of the configurations shown, it is clearly seen that the limiting case of the hemisphere ($l/D = 1/2$) is the most stable. This configuration, however, is probably impractical since the diameter requirement, as noted in the figures, is the largest. The optimum hemisphere-cylinder (Fig. 44 only) is seen to be only slightly better than the optimum flat-faced cylinder. It is also

noted that the equivalent hemisphere-cylinder ($\sqrt{b^3}$ same as for sphere) has a much higher value of I^* than the corresponding sphere. This is expected, however, since the back surface of the sphere contributes essentially nothing to the stability. Furthermore, it is evident that the sphere with $r/\sqrt{r} = 1/4$ (Fig. 44) and the hemisphere with $r/\sqrt{r} = 1/2$ (Fig. 45) have the same stability (ϵ is the same for both configurations.)

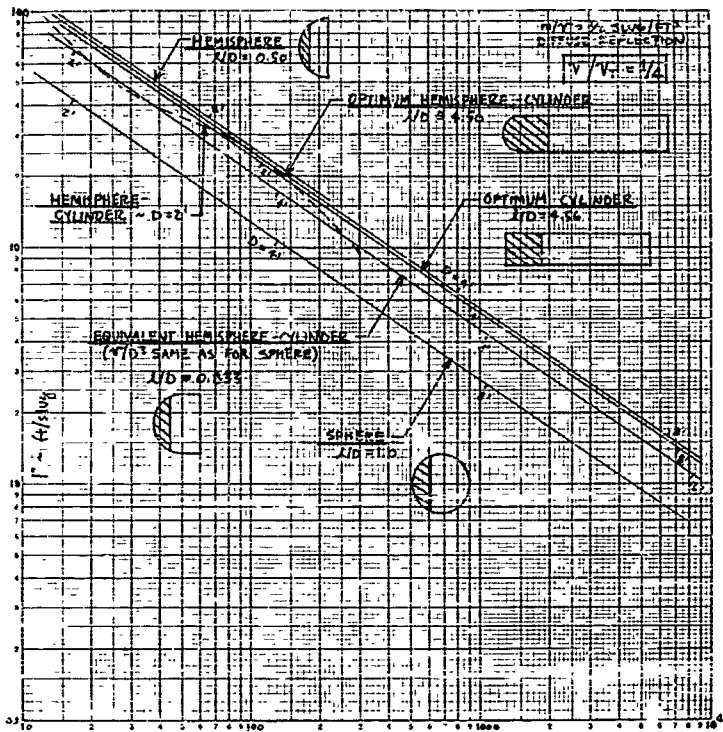


Figure 14. Comparison of Hemisphere-Cylinder Configurations - $\sqrt{V_T} = \sqrt{L}$.

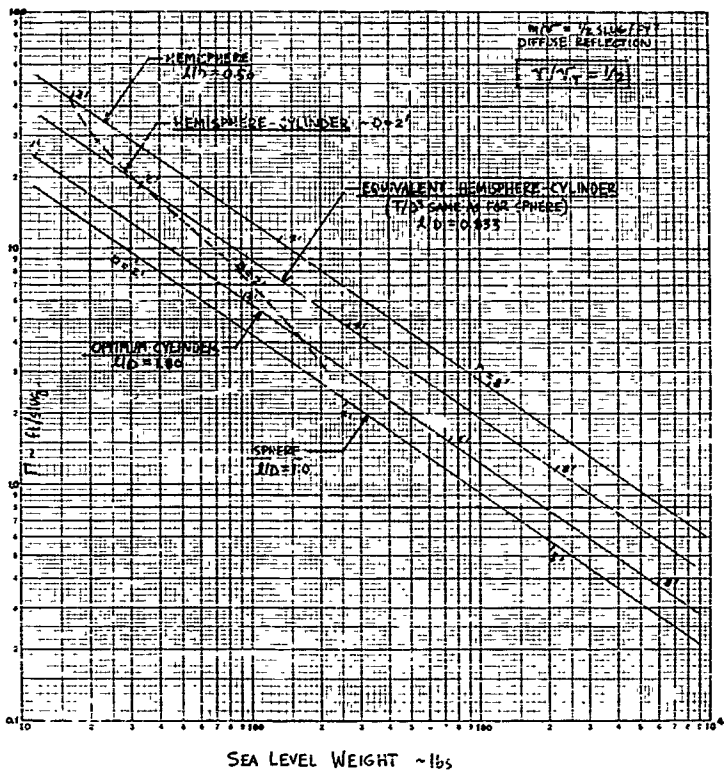


Figure 45. Comparison of Hemisphere-Cylinder Configurations - $r/r = 1/2$

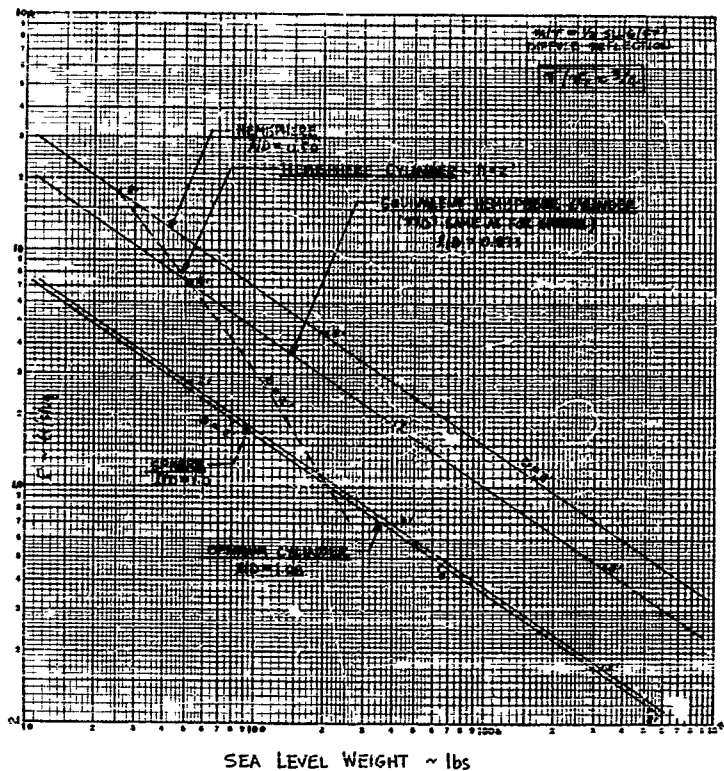


Figure 16. Comparison of Hemisphere-Cylinder Configurations - $r/r_c = 3/4$

3.4.3.4 Cone-Cylinder

The cone-cylinder analysis will be limited to the case where the cone is completely filled with payload and the cylinder is empty. The geometry of this configuration is shown in Fig. 47.

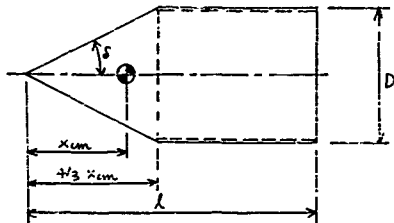


Figure 47. Cone-Cylinder Nomenclature

The principal moment of inertia about the y axis is easily found using Eq. (159) of the cone analysis; i.e.,

$$\bar{I} = \frac{mD^2}{80} \left[3 + \frac{16}{3} \left(\frac{X_{cm}}{l} \right)^2 \left(\frac{l}{D} \right)^2 \right] \quad (170)$$

and likewise \bar{I}_x is evaluated as

$$\bar{I}_x = \frac{3}{40} mD^2. \quad (171)$$

Eqs. (170) and (171) combine to give

$$M \equiv \frac{\bar{I}_x}{\bar{I}} - 1 = \frac{3 - \frac{16}{3} \left(\frac{X_{cm}}{l} \right)^2 \left(\frac{l}{D} \right)^2}{3 + \frac{16}{3} \left(\frac{X_{cm}}{l} \right)^2 \left(\frac{l}{D} \right)^2}. \quad (172)$$

For the homogeneous conical payload sketched in Fig. 47,

$$\begin{aligned} \frac{x_{cm}}{\ell} &= \frac{g(\sqrt{v_T})}{4 + 8(\sqrt{v_T})} \\ \cot \delta &= \frac{8(x_{cm}/\ell)(\ell/D)}{3} \\ \frac{r^{1/2}}{D} &= \left[\frac{\pi(x_{cm}/\ell)(\ell/D)}{9} \right]^{1/3} = \left[\frac{\pi(\ell/D)(\sqrt{v_T})}{4 + 8(\sqrt{v_T})} \right]^{1/3}. \end{aligned} \quad (173)$$

Using the cone-cylinder C_{max} from Eq. (28) and the equations above, Eq. (124) for $\Gamma_{m/r}^{1/3}$ may be expressed as

$$\begin{aligned} \Gamma_{m/r}^{1/3} &= \frac{180 \left[\frac{\pi(\ell/D)(\sqrt{v_T})}{4 + 8(\sqrt{v_T})} \right]^{1/3}}{\frac{x_{cm}}{\ell} \left[3 + \frac{16}{3} \left(\frac{x_{cm}}{\ell} \right) \left(\frac{\ell}{D} \right)^2 \right]} \left\{ 1 - \frac{2 x_{cm}}{\ell} + J \left[1 - 2 \frac{x_{cm}}{\ell} + \frac{8}{9} \left(\frac{x_{cm}}{\ell} \right)^2 \left(\frac{\ell}{D} \right)^2 \right] \right. \\ &\quad \left. + K \frac{8}{3} \frac{x_{cm}}{\ell} \frac{1 - \frac{8}{9} \left(\frac{x_{cm}}{\ell} \right)^2 \left(\frac{\ell}{D} \right)^2}{\sqrt{1 + \frac{64}{9} \left(\frac{x_{cm}}{\ell} \right)^2 \left(\frac{\ell}{D} \right)^2}} \right\} \end{aligned} \quad (174)$$

where J and K are defined by Eqs. (29). The first of Eqs. (173), of course, may be utilized to make Eq. (174) independent of x_{cm}/ℓ .

As in the case of the hemisphere-cylinder, the maximization of Eq. (174) by analytical methods is not practical. It is possible, however, to plot Γ versus payload weight (say) for constant values of m/\sqrt{v} , $\sqrt{v/v_T}$ and D . The optimum fineness ratio may be found by drawing a constant ℓ/D line tangent to the constant diameter curve. The optimum ℓ/D line then represents the cone-cylinder configuration which has the maximum Γ for a specified payload weight and volume ratio. This graphical optimization procedure is illustrated in Figs. 48, 49 and 50 for a payload density,

of $1/2$ slug/ft³; volume ratios of $1/4$, $1/2$ and $3/4$; and a diameter of 2 feet. Also plotted in these figures are the equivalent curves for the optimum cone and the optimum cylinder. It should be remembered that the cone-cylinder configuration used in these comparisons is composed of a fully loaded cone and a massless, cylindrical skirt. When $v/v_T = 1/4$, it is seen from Fig. 48 that the optimum cone-cylinder has the lowest value of Γ for a given weight; however, when $v/v_T = 1/2$ or $3/4$ the optimum cone-cylinder has a higher value of Γ than the optimum cylinder. It is also seen from these figures that for a given diameter and volume ratio, there is a range of sea-level weights for which the cone-cylinder has the highest value of Γ of the three configurations shown. For $v/v_T = 1.0$, the cone and cone-cylinder are obviously coincident.

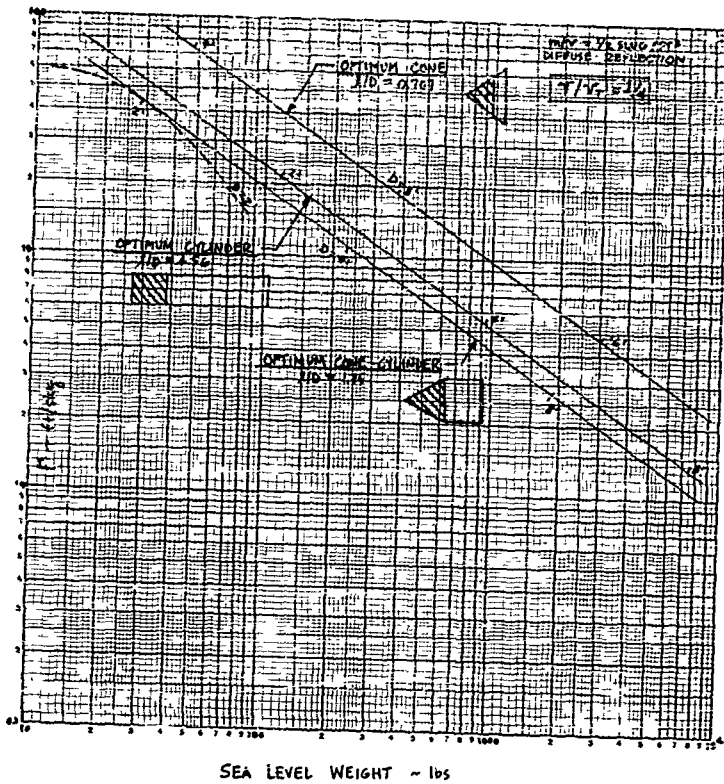


Figure 48. Comparison of Cone-Cylinder Configurations - $\sqrt{V_c} = 1/4$

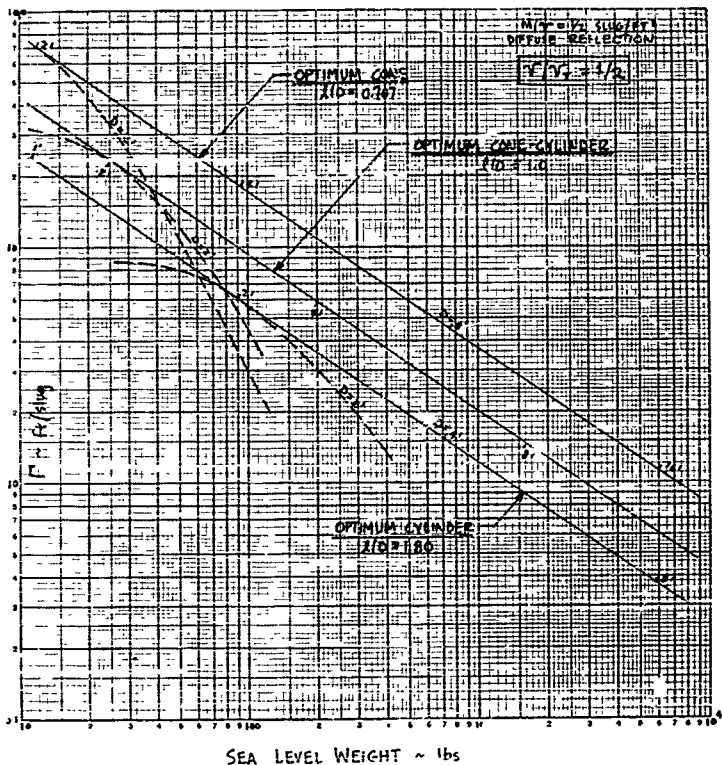


Figure 29. Comparison of Cone-Cylinder Configurations - $V/V_c = 1/2$

4. DYNAMIC STABILITY ANALYSIS

4.1 General Considerations

In Volume I of this series of reports, it is argued that the aerodynamic damping-in-pitch of near-Earth satellites produces, for all practical purposes, a negligible effect on the satellite's oscillatory motion. Even if the damping-in-pitch derivative $C_{m\dot{q}}$ is considerably larger than its static counterpart $C_{m\alpha}$, the non-dimensional pitch rate $\dot{q} \bar{c} / 2 V_\infty$, which multiplies $C_{m\dot{q}}$, is an extremely small quantity when compared with the expected angle of attack. This is more clearly illustrated by a simple comparison of the damping parameter \mathcal{Q}_p^* with the static moment parameter \mathcal{G}_p^* . Accordingly, from Volume I, in which the satellite orientation angles and rates are expressed in terms of the orbit parameters,

$$\mathcal{Q}_p^* \equiv \Gamma_q \frac{\rho_0 \Gamma_p}{8} \frac{V_R}{V} \quad (175)$$

where

$$\Gamma_q \equiv -\frac{C_{m\dot{q}} S_n \bar{c}^2}{I} \quad \left[\frac{\text{ft}^2}{\text{slug}} \right] \quad (176)$$

and, from Eq. (122),

$$\mathcal{G}_p^* \equiv \Gamma \frac{\rho_0 r_p^2}{2} \left(\frac{V_R}{V} \right)^2 \quad (122)$$

where

$$\Gamma \equiv \frac{C_{m\alpha} S_n \bar{c}}{I} \quad \left[\frac{\text{ft}}{\text{slug}} \right] \quad (123)$$

By inspection of Eqs. (175) and (122), it is seen that if Γ_q and Γ are of the same order (as will be shown), then \mathcal{Q}_p^* and \mathcal{G}_p^* differ in magnitude by at least the order of \bar{c}/r_p ; i.e., the ratio of the satellite reference dimension to the perigee radius, which for reasonable satellites (with dimensions of at most 10^2 ft.) is of order 10^{-5} , a very small number.

Although the results of the numerical analysis in Volume I adequately show the insignificance of the aerodynamic damping insofar as the satellite's angular motion is concerned, it is the purpose of this section, in

part, to justify the original hypothesis that Γ_q is not significantly larger than Γ . Although this investigation was at first seen superficially, there are applications in which aerodynamic damping-in-pitch may conceivably be a useful input; e.g., the design of a sensitive active stabilization system. Accordingly, the analyses to follow investigate the variations of the damping-in-pitch derivative, C_{mq} , throughout the acute angle of attack range for the three basic body shapes: the cylinder, sphere and cone. The purpose of the angle of attack variation is to determine if there are any large discrepancies between C_{mq} at angle of attack and the usual definition of C_{mq} ; i.e., in Eq. (176), C_{mq} is defined as, for simplicity,

$$C_{mq} \equiv \left[\frac{\partial C_m}{\partial \left(\frac{qE}{2V_\infty} \right)} \right]_{q \rightarrow 0} \quad (177)$$

$$\alpha = 0$$

4.2 Damping-in-Pitch of Basic Body Shapes

4.2.1 Introduction

Due to the complicated nature of the integrals, the damping-in-pitch derivative C_{mq} is calculated using the approximate theory of Ref. 4. Consequently, it may be shown that the evaluation of C_{mq} as q approaches zero incurs very little error since for diffuse reflection, the approximate theory yields a linear variation of C_m with q . In addition, the various Γ_q 's are calculated using optimum body geometry as determined from the static stability analyses. Due to the generally second-order importance of aerodynamic damping as pertaining to this study, the optimization of body geometry for maximum aerodynamic damping does not seem justified.

Diffuse reflection ($\sigma = \sigma' = 1$) is assumed, and as before, the reference area and length are $\pi D^2/4$ and D respectively.

4.2.2 Cylinder

The damping-in-pitch derivative for a cylinder, without end effects and for diffuse reflection, may be evaluated using the approximate free-molecule flow theory (Ref. 4 or 6). Then, from Eq. (27),

$$C_{mq}_{cyl} \equiv - \left(\frac{A}{D} \right)^2 \left[\frac{16}{3\pi} \sin \alpha + \frac{2}{3} \frac{\sqrt{\pi}}{5\alpha} \sqrt{\frac{14}{\pi}} \right] \left[1 - 3 \frac{X_{cm}}{L} + 3 \left(\frac{X_{cm}}{L} \right)^2 \right] \quad (178)$$

$$- \left(\frac{A}{D} \right)^2 \left[1 - 2 \frac{X_{cm}}{L} \right] \cos \alpha$$

where the cylinder geometry is defined in Fig. 31. Likewise, the contribution of the flat-faced nose portion may be formed as

$$C_{m_{g,nose}} \cong -4 \left(\frac{L}{D} \right)^2 \left(\frac{x_{cm}}{L} \right)^2 \cos \alpha \quad (179)$$

Since there is assumed to be no interaction between the two surfaces, Eqs. (178) and (179) may be added to give

$$C_{m_g} \cong - \left(\frac{L}{D} \right)^3 \left[\frac{16}{3\pi} \sin^2 \alpha + \frac{2\sqrt{\pi}}{3S_{ref}} \sqrt{\frac{T_w}{T_\infty}} \right] \left[1 - 3 \frac{x_{cm}}{L} + 3 \left(\frac{x_{cm}}{L} \right)^2 \right] - \left(\frac{L}{D} \right)^2 \cos \alpha \left[1 - 2 \frac{x_{cm}}{L} + 4 \left(\frac{x_{cm}}{L} \right)^2 \right] \quad (180)$$

Eq. (180) is presented for the simple case of $T_w = T_\infty$ in Figs. 51, 52 and 53 for cylinder fineness ratios of 1, 2 and 5 respectively. The associated temperature correction term is seen to be, from Eq. (180),

$$\Delta C_{m_g} \equiv C_{m_g} - C_{m_g}|_{T_w=T_\infty} \cong - \left(\frac{L}{D} \right)^3 \frac{2\sqrt{\pi}}{3S_{ref}} \left[\sqrt{\frac{T_w}{T_\infty}} - 1 \right] \left[1 - 3 \frac{x_{cm}}{L} + 3 \left(\frac{x_{cm}}{L} \right)^2 \right]$$

or

$$\frac{S_{ref} \Delta C_{m_g}}{\left(\frac{L}{D} \right)^3 \left[1 - 3 \frac{x_{cm}}{L} + 3 \left(\frac{x_{cm}}{L} \right)^2 \right]} \cong - \frac{2\sqrt{\pi}}{3} \left[\sqrt{\frac{T_w}{T_\infty}} - 1 \right] \quad (181)$$

which is independent of angle of attack, and is shown in Fig. 54 for a wide range of temperature ratios.

Unlike the case of static pitching moment slope, the non-linear variation of C_{m_g} with center of mass location is clearly evident. It may also be noted from Figs. 51, 52 and 53 that C_{m_g} becomes more negative (more damping) as angle of attack initially increases.

For purposes of evaluating Γ_q of the cylinder, Eq. (160) for the zero angle of attack case reduces to²

$$C_{m_y}_{\alpha=0} \cong -\frac{2\sqrt{\pi}}{3S_{oa}} \left[\frac{\sqrt{I_w}}{I_{oa}} \left(\frac{l}{D} \right)^3 \left[1 - 3 \frac{X_{com}}{l} + 3 \left(\frac{X_{com}}{l} \right)^2 \right] - \left(\frac{l}{D} \right)^2 \left[1 - 2 \frac{X_{com}}{l} + 4 \left(\frac{X_{com}}{l} \right)^2 \right] \right]. \quad (182)$$

The darping-in-pitch parameter, Γ_q , may now be formed using Eq. (182) and Eq. (125) for the pitch moment of inertia. Hence,

$$\Gamma_q \cong \frac{-C_{m_y} \pi D^4}{4 I} \cong \frac{\pi 4 D^2 \left(\frac{l}{D} \right)^3 \left\{ \frac{2\sqrt{\pi}}{3S_{oa}} \left[\frac{\sqrt{I_w}}{I_{oa}} \left(\frac{l}{D} \right)^3 \left[1 - 3 \frac{X_{com}}{l} + 3 \left(\frac{X_{com}}{l} \right)^2 \right] + \left[1 - 2 \frac{X_{com}}{l} + 4 \left(\frac{X_{com}}{l} \right)^2 \right] \right\}}{m \left\{ 1 + \frac{16}{3} \left(\frac{X_{com}}{l} \right)^2 \left(\frac{l}{D} \right)^2 \right\}} \right\} \quad (183)$$

or for the case of an off-center, homogeneous payload, Eq. (183) may be written in terms of payload volume ratio and weight using Eq. (127) and the assumption that $m/\gamma = 1/2 \text{ slug/ft}^3$; i.e.,

$$\Gamma_q \cong \frac{74.6}{W V_p} \left(\frac{l}{D} \right)^3 \left\{ \frac{2\sqrt{\pi}}{3S_{oa}} \left[\frac{\sqrt{I_w}}{I_{oa}} \left(\frac{l}{D} \right)^3 \left[1 - \frac{3}{2} \frac{X}{l} + \frac{3}{4} \left(\frac{X}{l} \right)^2 \right] + \left[1 - \frac{X}{l} + \left(\frac{X}{l} \right)^2 \right] \right\} \right. \\ \left. \left[\frac{1}{D} \left(\frac{X}{l} \right)^2 \right]^{3/2} \left\{ 1 + \frac{4}{3} \left(\frac{X}{l} \right)^2 \left(\frac{l}{D} \right)^2 \right\} \right\}. \quad (184)$$

²It is realized that the "shadow" area on a cylinder may have a significant contribution to C_{m_y} for α near zero. For the practical case of low l/D and high ω , however, this contribution does not alter Eq. (182) appreciably.

For a sample calculation, let r/v_T equal $1/2$ and $3/4$, and let the respective fineness ratios be 1.80 and 1.08 , as taken from table 1. Then Eq. (184) becomes for $(1/s_m) (\bar{T}_w/\bar{T}_\infty) \cong .065$,

$$\begin{aligned} \bar{T}_1 &\cong \frac{101}{W^{1/3}} & [r/v_T = 1/2, k/D = 1.80] \\ \bar{T}_1 &\cong \frac{447}{W^{1/3}} & [r/v_T = 3/4, k/D = 1.08] \end{aligned} \quad (185)$$

Plots of Eqs. (185) are presented in Figs. 61 and 62 along with similar variations of \bar{T}_1 for the sphere and cone. Discussion of these figures is reserved for Section 4.2.5.

4.2.3 Sphere

The approximate damping-in-pitch derivative of a sphere may be found by integrating Eq. (27) over the front (or windward) hemisphere. For diffuse reflection, the result is readily found to be

$$C_{m_i} \cong -\frac{2}{3} \left[\frac{\sqrt{\pi}}{2.5_m} \sqrt{\frac{\bar{T}_w}{\bar{T}_\infty}} \left(1 - \frac{2x_{cm}}{D}\right) + \cos \alpha \right] \left(1 - \frac{2x_{cm}}{D}\right). \quad (186)$$

Eq. (186) is shown in Fig. 55 for $T_w = T_\infty$. The normalized temperature correction term, which is

$$\frac{S_{\infty} \Delta C_{m_i}}{\left[1 - 2 \frac{x_{cm}}{D}\right]^2} \cong -\frac{\sqrt{\pi}}{3} \left[\sqrt{\frac{\bar{T}_w}{\bar{T}_\infty}} - 1 \right] \quad (187)$$

is plotted in Fig. 56. Unlike the cylinder, the sphere damping is seen to decrease with increasing angle of attack.

Evaluating Eq. (186) at zero angle of attack leads to the usual definition of C_{m_i} ,

$$C_{m_i}_{\alpha=0} \cong -\frac{2}{3} \left[\frac{\sqrt{\pi}}{2.5_m} \sqrt{\frac{\bar{T}_w}{\bar{T}_\infty}} \left(1 - 2 \frac{x_{cm}}{D}\right) + 1 \right] \left(1 - 2 \frac{x_{cm}}{D}\right). \quad (188)$$

For the case of a "loaded" sphere with a homogeneous payload, the substitution of Eq. (138) and Eq. (133) into Eq. (176) results in an expression for the sphere Γ_1 ; i.e.,

$$\Gamma_1 \cong \frac{\pi D^3 (3-2\epsilon)^2 \left[\frac{3\epsilon}{250} \sqrt{\frac{W}{T_{\infty}}} \left(i-2\frac{r_{cm}}{D} \right) + \left(1-2\frac{\lambda_{cm}}{D} \right) \right]}{9m\epsilon \left[1 - \frac{11}{6}\epsilon + \frac{6}{5}\epsilon^2 - \frac{3}{10}\epsilon^3 \right]} \quad (189)$$

The center of mass may be written in terms of depth ratio ϵ , and the diameter may be expressed as a function of payload weight for a specified payload density. Then by using Eqs. (134) and (135) and $r_1/r = 1/2 \sin \theta / \sin \theta$, Eq. (189) becomes

$$\Gamma_1 \cong \frac{815(i-\epsilon)^2 \left[\frac{3\epsilon}{250} \sqrt{\frac{W}{T_{\infty}}} (i-\epsilon)^2 + 3-2\epsilon \right]}{W^{1/3} \epsilon^{1/3} (3-2\epsilon)^{2/3} \left[1 - \frac{11}{6}\epsilon + \frac{6}{5}\epsilon^2 - \frac{3}{10}\epsilon^3 \right]} \quad (190)$$

where ϵ is a function of the payload volume ratio from the first of Eqs. (135) or Fig. 33. For the sample volume ratios of 1/2 and 3/4, the sphere Γ_1 is approximately

$$\begin{aligned} \Gamma_1 &\cong \frac{38^2}{W^{1/2}} & \left[r/r_T = 1/2 \right] \\ \Gamma_1 &\cong \frac{12.1}{W^{1/2}} & \left[r_1/r_T = 3/4 \right] \end{aligned} \quad (191)$$

where $(1/50) \sqrt{W/T_{\infty}}$ is taken to be .065. The foregoing expressions for Γ_1 are plotted in Figs. 61 and 62. A discussion of these results is in Section 4.2.5.

4.2.4 Cone

Following the example of cone static pitching moment, the damping-in-pitch derivative $C_{m\dot{\alpha}}$ may be estimated using the same approximate theory. Then, for diffuse reflection, the integration of Eq. (27) yields

$$C_{m\beta} \equiv \frac{-1}{4 \sin^3 \delta} \left\{ \left[\sin \delta \cos \alpha + \frac{\sqrt{\pi}}{2S_{\alpha}} \sqrt{\frac{T_w}{T_a}} \right] m^*(\zeta) + 2 \cos \delta \sin \alpha \left[\beta^*(\zeta) \right] \right\} \left[1 - \frac{4}{3} \frac{X_{com}}{\ell} \cos^2 \delta \right] \\ - \frac{4}{3} \frac{X_{com}}{\ell} \cos^2 \delta \left[1 - \frac{3}{2} \frac{X_{com}}{\ell} \cos^2 \delta \right] \left\{ \frac{\sqrt{\pi}}{2S_{\alpha}} \sqrt{\frac{T_w}{T_a}} m^*(\zeta) + \frac{2 \sin \alpha}{\cos \delta} \beta^*(\zeta) \right\} \quad (192)$$

where $\zeta \equiv \tan \delta / \tan \alpha$, as before, and

$$m^*(\zeta) \equiv \frac{1}{\pi} \left\{ \cos^{-1}(-\zeta) - \zeta \sqrt{1-\zeta^2} \right\} \quad [\zeta \leq 10] \\ \equiv 10 \quad [\zeta \geq 10] \\ \beta^*(\zeta) \equiv \frac{1}{\pi} \sqrt{1-\zeta^2} \quad [\zeta \leq 10] \\ \equiv 0 \quad [\zeta \geq 10] \quad (193)$$

Consequently, for $\alpha \leq \delta$, Eq. (192) simplifies to

$$C_{m\beta} \equiv \frac{-1}{4 \sin^3 \delta} \left\{ \left[\sin \delta \cos \alpha + \frac{\sqrt{\pi}}{2S_{\alpha}} \sqrt{\frac{T_w}{T_a}} \right] \left[1 - \frac{4}{3} \frac{X_{com}}{\ell} \cos^2 \delta \right] \right. \\ \left. - \frac{4}{3} \frac{X_{com}}{\ell} \cos^2 \delta \left[1 - \frac{3}{2} \frac{X_{com}}{\ell} \cos^2 \delta \right] \frac{\sqrt{\pi}}{2S_{\alpha}} \sqrt{\frac{T_w}{T_a}} \right\} \quad (194)$$

and for α identically equal to zero,

$$C_{m_{\alpha \geq 0}} \equiv -\frac{1}{4s\alpha^3 S} \left\{ \left[\sin \delta + \frac{\sqrt{\pi}}{2S\alpha} \sqrt{\frac{\Gamma_w}{\Gamma_a}} \right] \left[1 - \frac{4}{3} \frac{X_{cm}}{l} \cos^2 \delta \right] - \frac{4}{3} \frac{X_{cm}}{l} \cos^2 \delta \left[\frac{\sqrt{\pi}}{2S\alpha} \sqrt{\frac{\Gamma_w}{\Gamma_a}} \right] \left[1 - \frac{2}{3} \frac{X_{cm}}{l} \cos^2 \delta \right] \right\}. \quad (195)$$

Due to the assumptions inherent in the approximate theory, a plot of Eq. (192) for the entire angle of attack range will show a sharp break in the curve of $C_{m_{\alpha}}$ versus α at the points where $\alpha = S$. These breaks are due to the rather abrupt variation of both $m^*(\epsilon)$ and $p^*(\epsilon)$ as α becomes slightly greater than S ; i.e., as the shadow area becomes finite. Although the assumption of negligible shadow contribution is known to be fairly accurate for the calculation of cone lift, drag and static pitching moment, an attempt is made herein to smooth the variation of $C_{m_{\alpha}}$ with α by considering the effects of the shadow. This refinement is accomplished by first assuming an average normal component of molecular speed ratio over the shadow; and then substituting this quantity (assumed constant) into the exact expression for $C_{m_{\alpha}}$ (derivative of the third of Eqs. 20); and finally integrating over the shadow portion. The resulting incremental $C_{m_{\alpha}}$ due to the shadow is then added to Eq. (192) for the range $\alpha \geq S$. Without elaboration, the result is written as

$$C_{m_{\alpha}} \equiv -\frac{1}{4s\alpha^3 S} \left\{ \frac{e^{-S\alpha}}{\sqrt{\pi} S\alpha} \left[1 - m^*(\epsilon) \right] + \frac{1}{2} \left[\sin \delta \cos \alpha + \frac{\sqrt{\pi}}{2S\alpha} \sqrt{\frac{\Gamma_w}{\Gamma_a}} \right] \left[(1 + \text{erf } S_{N\alpha}) + (1 - \text{erf } S_{N\alpha}) m^*(\epsilon) \right] + p^*(\epsilon) \sin \alpha \cos \delta \left(1 - \text{erf } S_{N\alpha} \right) \right\} \left[1 - \frac{4}{3} \frac{X_{cm}}{l} \cos^2 \delta \right] - \frac{4}{3} \frac{X_{cm}}{l} \cos^2 \delta \left[1 - \frac{2}{3} \frac{X_{cm}}{l} \cos^2 \delta \right] \left\{ \frac{e^{-S\alpha}}{\sqrt{\pi} S\alpha} \left[1 - m^*(\epsilon) \right] + \frac{\sqrt{\pi}}{4S\alpha} \sqrt{\frac{\Gamma_w}{\Gamma_a}} \left[(1 + \text{erf } S_{N\alpha}) + (1 - \text{erf } S_{N\alpha}) m^*(\epsilon) \right] + \frac{p^*(\epsilon) \sin \alpha}{2 \cos \delta} (1 - \text{erf } S_{N\alpha}) \right\} \quad (196)$$

$$[\alpha \geq S]$$

where

$$S_{NAS} \equiv [S_{AVERAGE}]_{SHADOW} = \frac{2 \int_{\theta_m}^{\pi} S_w d\theta}{2 \int_{\theta_m}^{\pi} d\theta} \quad (197)$$

$$S_{NAS} = \frac{S_w \sin \delta \cos \alpha [1 - h(\epsilon)]}{1 - p(\epsilon)}$$

In Eq. (197), S_w is expressed by Eq. (22), $h(\epsilon)$ by Eq. (41) and $p(\epsilon)$ by Eq. (42). Also, the shadow angle θ_m is equal to $\cos^{-1}(-\epsilon) = \pi p(\epsilon)$.

The final cone C_{mg} equations - Eq. (194) for $\alpha \leq \delta$ and Eq. (196) for $\alpha \geq \delta$ - are plotted in Figs. 57, 58 and 59 for cone angles of 15° , 30° and 45° respectively. As before, T_w is set equal to T_∞ for simplicity. Fig. 60 presents the corresponding variation of ΔC_{mg} (normalized) due to T_w different from T_∞ . The equations for these curves are

$$\frac{S_w \Delta C_{mg} \sin^3 \delta}{\left[1 - \frac{8}{3} \frac{\chi_{cm}}{k} \cos^2 \delta + 2 \left(\frac{\chi_{cm}}{k}\right)^2 \cos^4 \delta\right]} \approx -\frac{\sqrt{\pi}}{8} \left[\sqrt{\frac{T_w}{T_\infty}} - 1 \right] \quad [\alpha \leq \delta] \quad (198)$$

$$\frac{S_w \Delta C_{mg} \sin^3 \delta}{\left[1 - \frac{8}{3} \frac{\chi_{cm}}{k} \cos^2 \delta + 2 \left(\frac{\chi_{cm}}{k}\right)^2 \cos^4 \delta\right]} \approx -\frac{\sqrt{\pi}}{16} \left[\sqrt{\frac{T_w}{T_\infty}} - 1 \right] \left[(\text{Hertf}_{S_{NAS}}) + (1 - \text{ert}_{S_{NAS}}) r^{\alpha/\delta} \right] \quad [\alpha \geq \delta]$$

It may be seen in Figs. 57 through 60 that the breaks in the curves at $\alpha = \delta$ are still evident, especially in Fig. 60, and for $S_w = \infty$ in Figs. 57 through 59. The use of the shadow correction, however, definitely improves the smoothness of the C_{mg} curves at the lower speed ratios.

Now that $C_{m\dot{\alpha}}$ has been formulated, the damping-in-pitch parameter Γ_q may be written using Eq. (195) and Eq. (139). Accordingly, Eq. (176) becomes

$$\Gamma_q \cong \frac{15\pi D^2}{4m \sin^2 \left(\frac{\alpha_{\text{max}}}{L} \right) (4 + \cot^2 \delta)} \left\{ \left[\sin \delta + \frac{\pi}{2S_{\text{av}}} \left| \frac{\overline{T_w}}{\overline{T_a}} \right| \left[1 - \frac{4}{3} \frac{\alpha_{\text{max}}}{L} \cos^2 \delta \right] \right] \right. \\ \left. - \frac{2}{3} \frac{\alpha_{\text{max}}}{L} \cos^2 \delta \frac{\pi}{S_{\text{av}}} \left| \frac{\overline{T_w}}{\overline{T_a}} \right| \left[1 - \frac{3}{4} \frac{\alpha_{\text{max}}}{L} \cos^2 \delta \right] \right\}. \quad (199)$$

Using the optimum cone angle, $\delta = \cot^{-1} \sqrt{2}$, from Section 3.4.2.3, and the relation, $\alpha_{\text{max}}/L = (3/4)(\nu/\nu_T)^{2/3}$, Eq. (199) may be expressed in terms of the payload volume ratio. Hence,

$$\Gamma_q \cong \frac{262}{W^{1/3} \left(\frac{\alpha}{\nu_T} \right)^{2/3}} \left\{ \left[\frac{1}{\sqrt{3}} + \frac{\pi}{2S_{\text{av}}} \left| \frac{\overline{T_w}}{\overline{T_a}} \right| \left[1 - \frac{2}{3} \left(\frac{\alpha}{\nu_T} \right)^{2/3} \right] \right] \right. \\ \left. - \frac{2}{4} \left(\frac{\alpha}{\nu_T} \right)^{2/3} \frac{\pi}{S_{\text{av}}} \left| \frac{\overline{T_w}}{\overline{T_a}} \right| \left[1 - \frac{3}{4} \left(\frac{\alpha}{\nu_T} \right)^{2/3} \right] \right\} \quad (200)$$

where $m/r = 1/2 \text{ slug/ft}^3$. For the present examples, the substitution of $\nu/\nu_T = 1/2$ and $3/4$ into Eq. (200) yields

$$\Gamma_q \cong \frac{191}{W^{1/3}} \quad \left[\nu/\nu_T = 1/2 \right] \\ \Gamma_q \cong \frac{92.7}{W^{1/3}} \quad \left[\nu/\nu_T = 3/4 \right] \quad (201)$$

Plots of Eqs. (201) are shown in Figs. 61 and 62 along with the corresponding cylinder and sphere expressions.

4.2.5 Comparison of Basic Body Shapes

As noted previously, Figs. 61 and 62 present plots of the dynamic stability parameter Γ_d versus satellite payload weight for the special cases where the "loaded" configurations have payload volume ratios of 1/2 and 3/4. The payload is assumed homogeneous with a mass density of 1/2 slug/ft³. The figures clearly indicate, as expected, that the cone has more aerodynamic damping than either the cylinder or sphere; at least for the optimum geometry (for maximum Γ) assumed for these examples. By comparing Figs. 61 and 62 with Figs. 36 and 37, it is also noticed, as hypothesized previously, that Γ_d is of the same order of magnitude as the static parameter Γ , especially at the lower weights. Consequently, it may be concluded that since Γ_d is not significantly larger than Γ (say by a factor of 10⁴), the assertion in Volume I of essentially negligible aerodynamic damping may be regarded as fully substantiated.

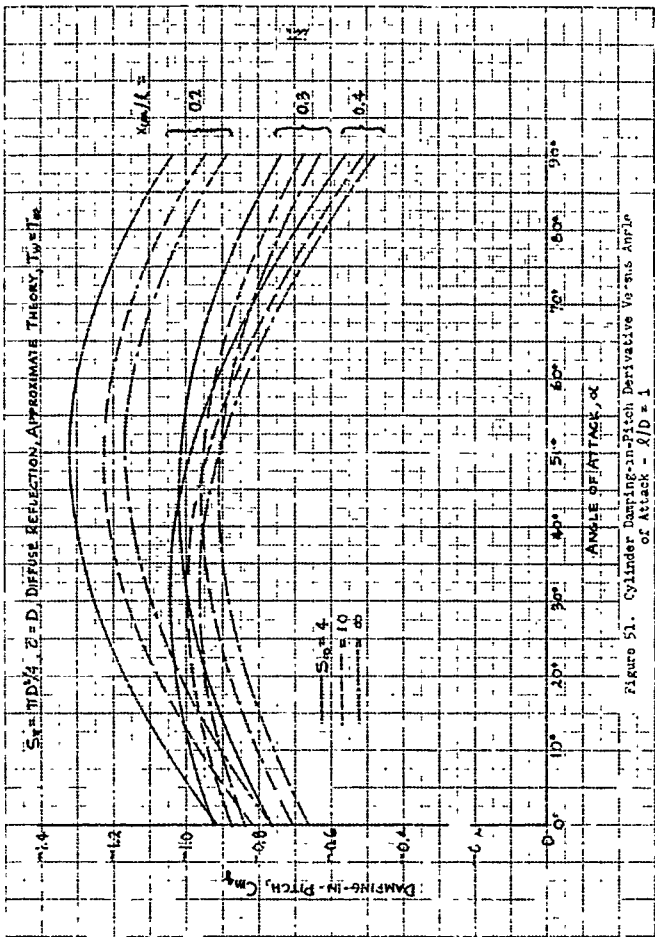


Figure 51. Cylinder Damping-in-Pitch Derivative Versus Angle of Attack - $D/D = 1$

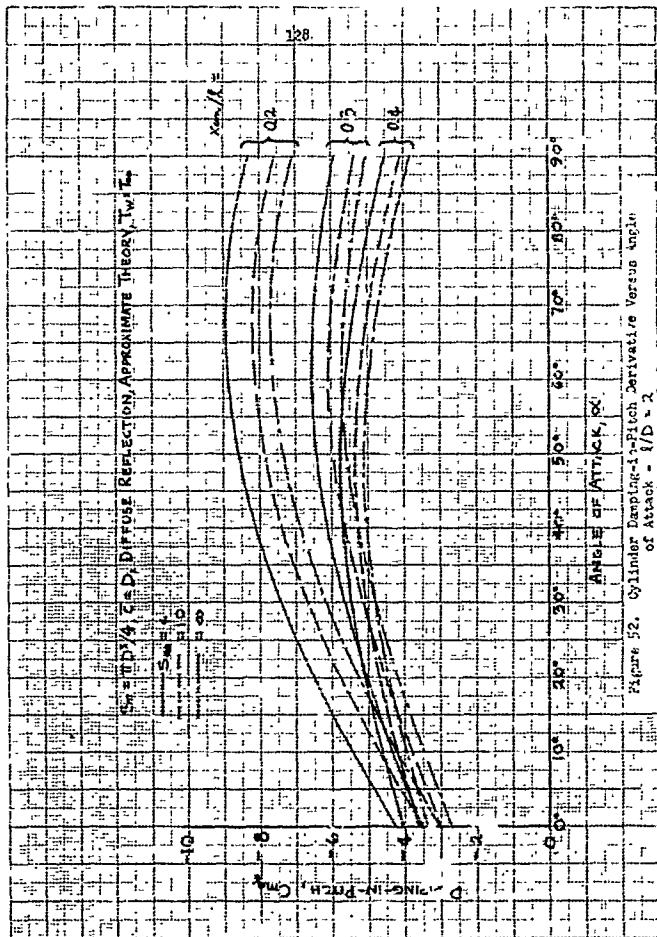


Figure 52. Cylinder Dipping-in-Pitch Derivative Versus Angle of Attack - $1/D = 2$.

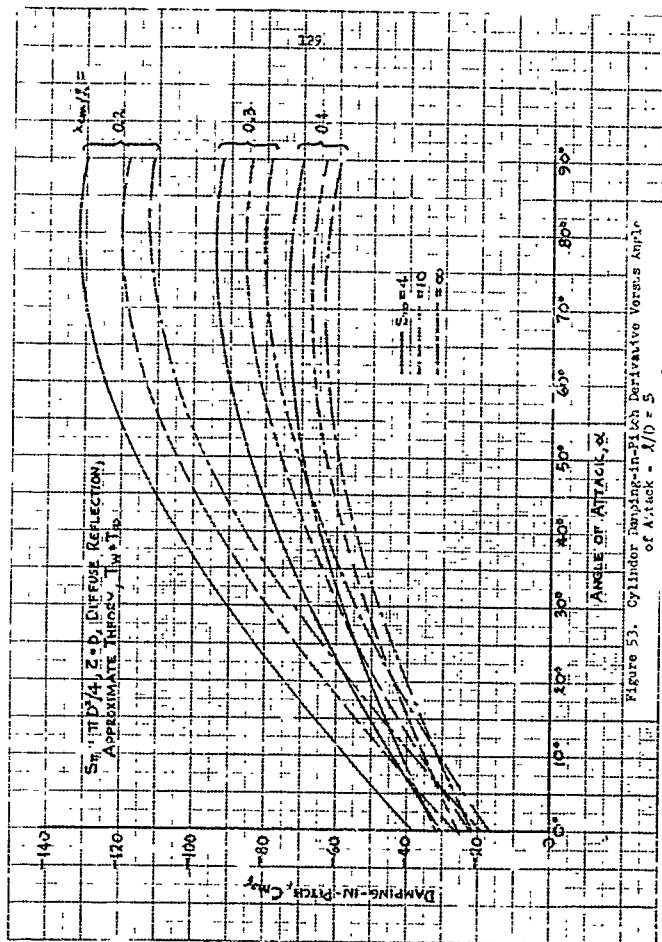


Figure 53. Cylinder Damping-in-Pitch Derivative Versus Angle of Attack - $\lambda/D = 5$

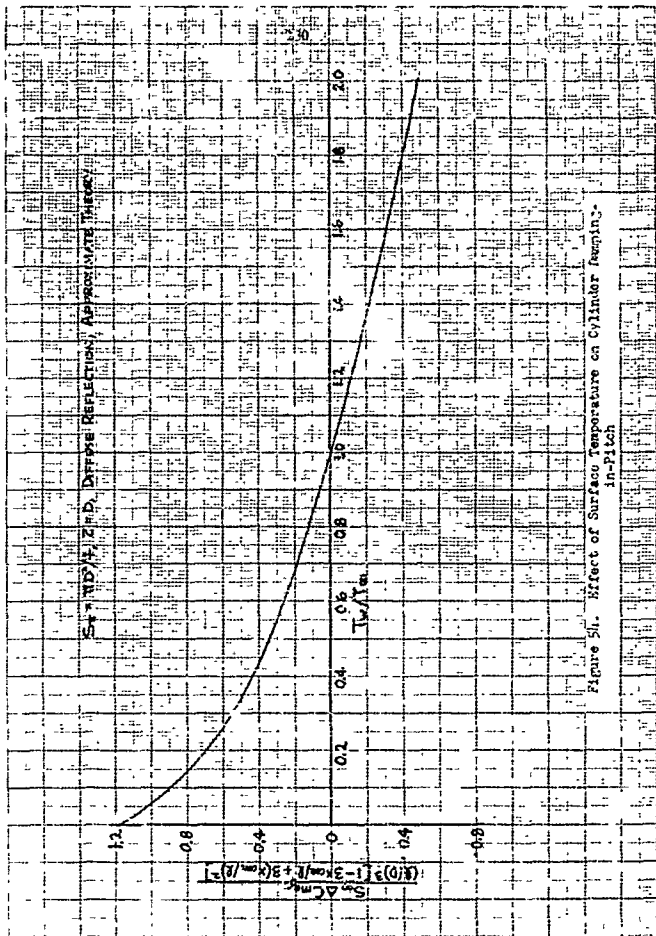


Figure 50. Effect of Surface Temperature on Cylindrical Resonance in Pitch

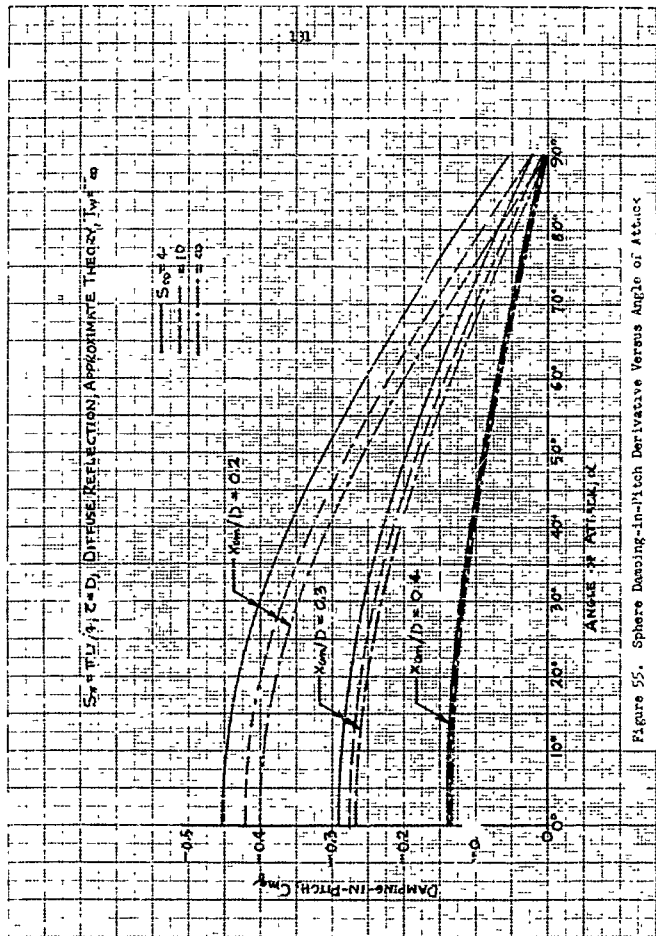


Figure 55. Sphere Damping-in-Pitch Derivative Versus Angle of Attack

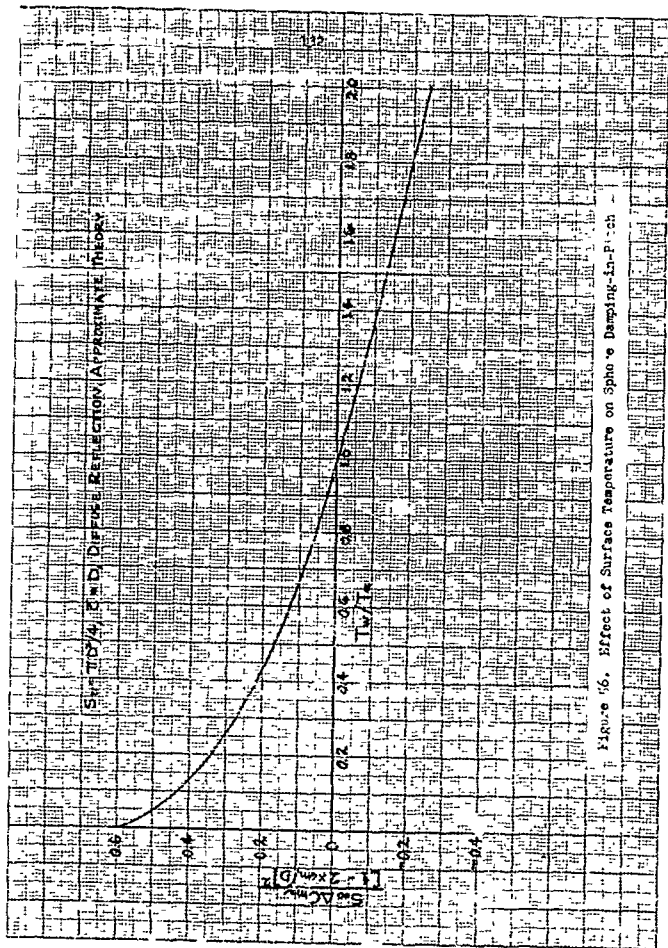


Figure 16. Effect of Surface Temperature on Spoke Damping-In-Pitch

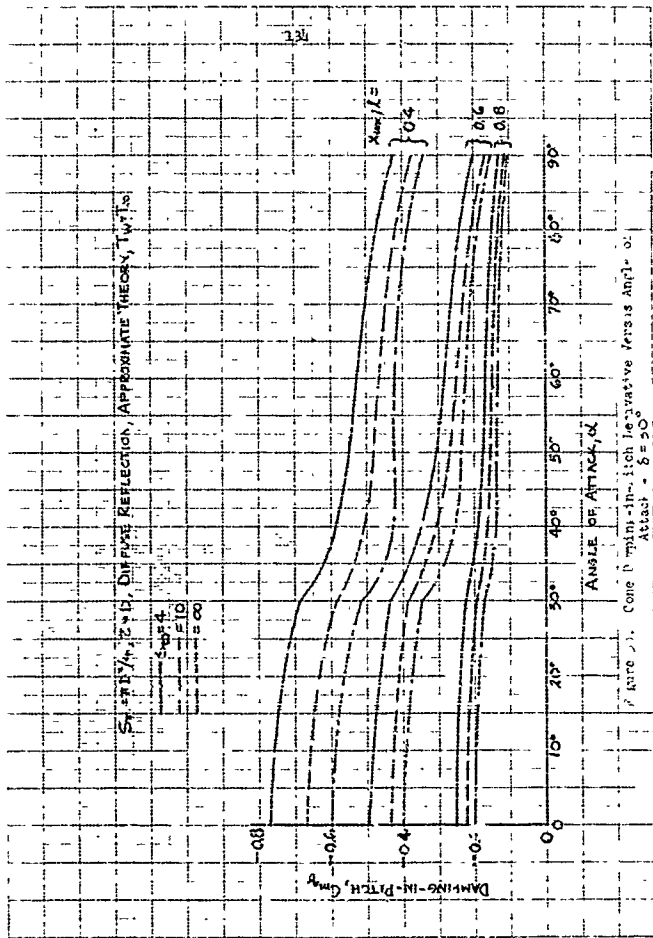


Figure 23. Cone of spins-in-pitch for negative twists Ampl. of
 Attack = $\delta = 30^\circ$

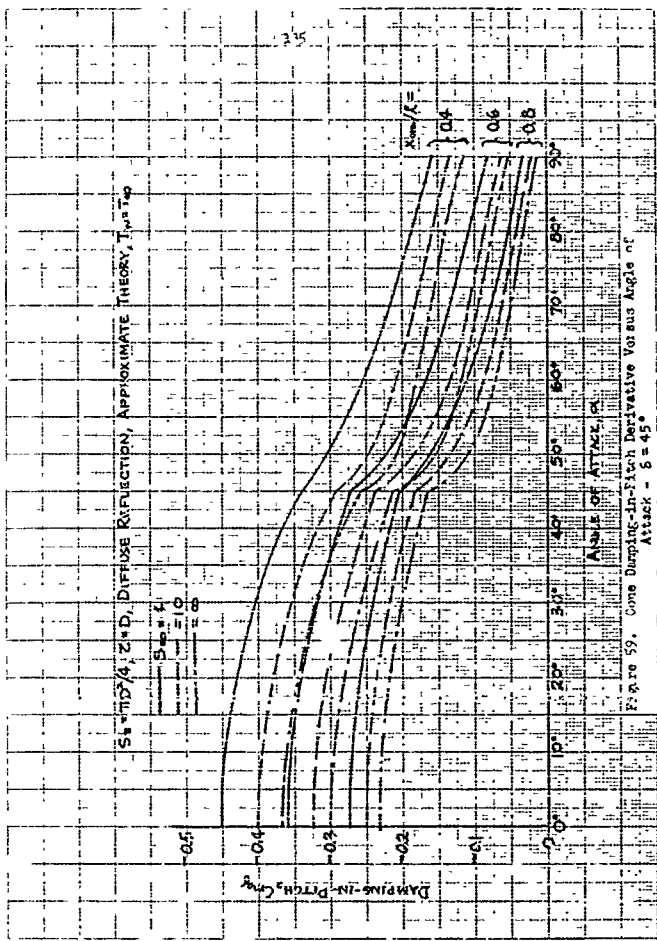
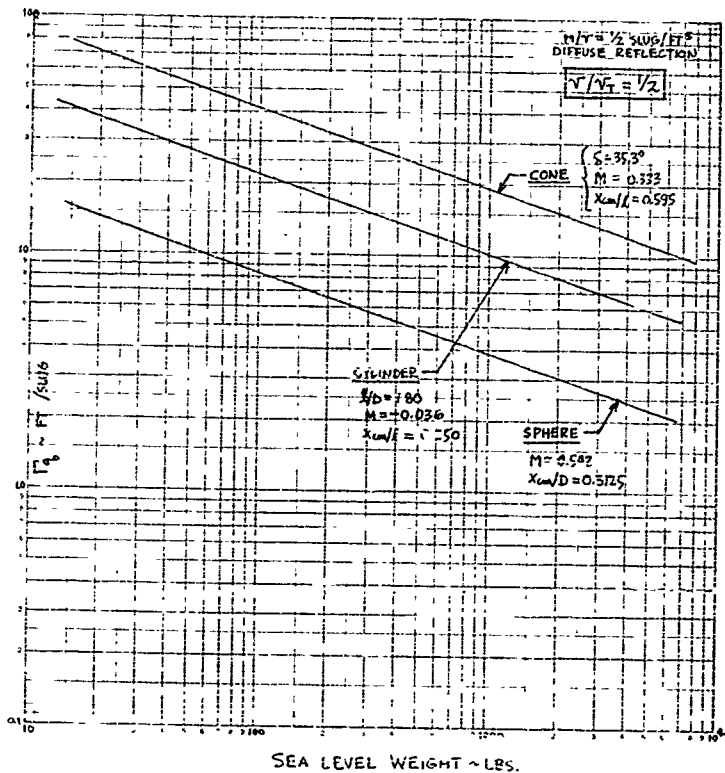


FIGURE 59. Cone Damping-in-Pitch Derivative Versus Angle of Attack - $B = 1$

Figure 61. Comparison of Basic Body Shapes - $\sqrt{V_T} = 1/2$

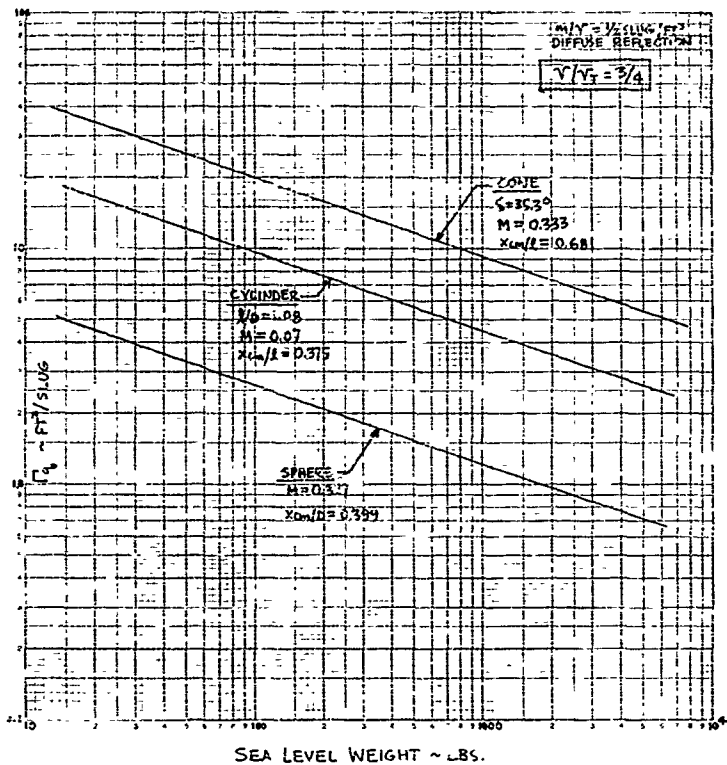


Figure 62. Comparison of Basic Body Shapes - $\sqrt{V_T} = 3/4$

CONCLUSIONS

Recent developments in the application of free-molecule theory (Ref. 6) have permitted a rather detailed aerodynamic analysis of near-Earth satellites. This theory, although restricted to convex body shapes, has been utilized to yield rapid and nearly exact aerodynamic force and moment calculations for most satellite configurations and orbit conditions. Moreover, there are no restrictions as to the variance of either the tangential or normal momentum exchange coefficients, σ and σ' . As shown, the surface temperature, T_w , may also be treated as a variable over the body. In view of the general nature of this approximate theory, numerous calculations (which may be too detailed for some readers) and charts have been presented as examples of the applicability of the theory. Although the foregoing study was intended to "stand alone", the primary purpose of this report was to augment the conclusions of Volume I of this series of reports. That is, aerodynamic stabilization and orientation of near-Earth satellites is feasible as long as proper (but not unreasonable) aerodynamic design and internal mass distribution conditions are met.

A supplemental but significant part of the study was concerned with estimating drag coefficients of simple configurations. The calculations showed that if the drag coefficients are based on the projected frontal area (quite often a random variation) of the satellite, a unified drag coefficient variation could be approximated for most, low fineness ratio (order of one) configurations. For long cylinders or very sharp cones, however, the quasi-uniform drag variation with molecular speed ratio could be in considerable error.

Since the primary purpose of this study was to investigate the effects of aerodynamic torques, subsequent portions of this volume were concerned with methods for estimating aerodynamic static and dynamic pitching moment coefficients as well as the incorporation of these coefficients in the design of practical satellite configurations. Although the calculation of aerodynamic coefficients in free-molecule flow are inherently different from that in continuum flow, the conventional "airplane" definitions of C_m . $C_{m\alpha}$ and $C_{m\dot{\alpha}}$ were conveniently utilized throughout this volume. Expressions for the static pitching moment coefficient, C_m , were presented for the three basic cylindrical, spherical and conical body shapes. In addition, charts of C_m versus angle of attack were presented for these shapes, which may be useful in other free-molecule design studies not related to this report. These charts were also used to substantiate the linear C_m approximation for small angle of attack ranges; a basic and common assumption. Consequently, expressions for the initial pitching moment slope, $C_{m\alpha}$, were formulated for the basic body shapes, and subsequently for the more complex shapes of the power law body, the truncated cone, the hemisphere-cylinder, and the cone-cylinder. For simplicity purposes, the usual assumption of diffuse molecular reflection was utilized for these $C_{m\alpha}$ calculations.

Since the free-molecule theory used in this study was not restricted to specific values of the reflection coefficients, σ and σ' , and the surface temperatures, T_w ; examples were presented which illustrated the effects of both uniform and non-uniform variations of σ , σ' and T_w . It was shown that the surface temperature level as well as longitudinal and axial variations of temperature have little effect on static stability or orientation, at least for the simple configurations considered. On the other hand, the magnitude of the reflection coefficients was shown to affect the pitching moment slope by varying amounts, depending on the configuration and the relative dominance between pressure and shear. For nearly diffuse molecule-surface interactions (σ and σ' between 0.9 and 1.0), however, the example pitching moment slopes were shown to be only slightly different from completely diffuse values.

Based upon the satellite motion analysis in Volume I, the aerodynamic stability parameter Γ was investigated for the three basic body shapes as well as the more complex configurations. Since Γ was defined as being the pitching moment slope, times its reference dimensions, divided by the pitching moment of inertia, the maximization of Γ established certain optimum body geometry for each set of constraints. The satellite models selected for the investigations had homogeneous payloads concentrated in the forward portion with rigid, but massless, shells or skirts comprising the aft portions. The skirts, which could logically be fairings between the payload and booster, augmented the aerodynamic stability without affecting the pitching moment of inertia. Accordingly, the optimization process tended to maximize the aerodynamic contribution while minimizing the mass contribution. For a specified payload volume to total satellite volume ratio and a specified payload mass density, the maximization of Γ resulted in optimum configurations which had rather low (and practical) length to diameter ratios. On this basis, it was shown that the pointed cone, the power law body, and the truncated cone were generally the most stable for a given payload weight. For other constraints, however, such as a specified maximum diameter, the cylinder and the cone-cylinder showed promise as being useful and practical aerodynamic shapes. The sphere with its impractical small w , as expected, the poorest configuration. The optimum sphere-capped cylinder, however, was shown to have nearly the same static stability as the optimum flat-faced cylinder.

Since the approximate free-molecule theory used in this study permitted rapid calculations of the aerodynamic damping-in-pitch derivative, and since pitch damping was necessarily considered in the satellite motion analysis (Volume I), the aerodynamic investigation was concluded with a brief study of the damping-in-pitch derivative, $C_{m\dot{\alpha}}$, and its counterpart, $\Gamma_{\dot{\alpha}}$, for the basic cylinder, sphere and cone configurations. As in the case of static pitching moment, C_m , design charts of $C_{m\dot{\alpha}}$ were presented for the basic body shapes. Since it was argued in Volume I that aerodynamic damping is negligible if $\Gamma_{\dot{\alpha}}$ is of the same order of magnitude as Γ , sample calculations of $\Gamma_{\dot{\alpha}}$ were made for the cone, sphere and cylinder using optimum static stability geometry (for maximum Γ). The insignificance of aerodynamic damping, as pertaining to this study, was verified.

Although this study has provided a foundation for satellite aerodynamic design, several important and unanswered questions remain. For example, the lack of a general, three-dimensional theory for predicting the effects of molecular reflections between surfaces has prevented the aerodynamic analysis of concave bodies; e.g., configurations with flared skirts or inflatable, spherical stabilizers. This lack of a usable surface-surface interaction theory has also excluded investigations of complex, "winged" satellite configurations, especially from the viewpoint of orientation and orbit control. In addition, aerodynamic analyses of satellites and satelloids in the near free-molecule or transitional regime are essentially non-existent. Consequently, it is clear that the practical applications of rarefied gasdynamics have been only briefly exploited. Even with the extensive analysis contained herein, the free-molecule aerodynamic investigation of simple, convex body shapes is by no means complete. For instance, the simplifying assumptions of homogeneous payloads and massless skirts leave much to be desired. Also, no attempt was made to analytically determine an optimum configuration, by the methods of variational calculus techniques, which would provide an absolute maximum for the static stability parameter Γ .

Insofar as passive aerodynamic stabilization and orientation of near-Earth satellites has been found to be feasible, it is recommended that concentrated effort be given to the advancement of applied rarefied gasdynamics in order to lay the foundations for active aerodynamic satellite control. It is realized, of course, that a conceptual understanding of basic gas kinetics is a prerequisite to the development of a useful and accurate method of predicting L_∞ density, aerodynamic characteristics. This also requires increased study of the molecule-surface interaction phenomenon, especially at satellite energies. Accordingly, numerous problems remain which both research and engineer must solve if aerodynamic control and stability is to be incorporated in sophisticated satellite systems.

APPENDIX ATHE EFFECT OF SOLAR RADIATION PRESSURE ON SATELLITE TORQUE

Due to the (nearly) exponential decrease of atmosphere density with altitude, indications are that the magnitude of satellite torques due to solar radiation pressure may approach the magnitude of aerodynamic and gravitational torques at altitudes near 400 miles. In order to estimate these solar torques more precisely, it is necessary to develop expressions for photon pressure and shearing forces on a body surface of general shape. The qualitative analysis to follow assumes that the free-stream photon "gas" is analogous to a unidirectional particle field, and that the photons have a mass density and travel with the speed of light. Accordingly, this analogy permits utilization (but slight modification) of the free-molecule aerodynamic expressions in Section 1.

The pressure and shearing stresses due to an oncoming photon stream incident upon a unit surface area may be respectively written as

$$p_i = P_{s\infty} \frac{c_n^2}{c_\infty^2} \quad (A-1)$$

$$\tau_i = P_{s\infty} \frac{c_n c_T}{c_\infty^2}$$

where $P_{s\infty}$ represents the free-stream radiation pressure (one-half of the maximum measurable pressure) and where c_n and c_T are the normal and tangential components of the free-stream photon velocity c_∞ . If all the incident photons are reflected from the surface specularly, then normal and tangential forces per unit area due to the rebounding photons are

$$p_r = p_i = P_{s\infty} \frac{c_n^2}{c_\infty^2} \quad \left[\begin{array}{l} \text{No absorption,} \\ \text{specular reflection} \end{array} \right] \quad (A-2)$$

$$\tau_r = \tau_i = P_{s\infty} \frac{c_n c_T}{c_\infty^2}$$

and hence, the total force components per unit area become

$$P = P_i - P_r = 2 \beta_{\infty} \frac{C_N^2}{C_0^2}$$

$$\gamma = \tau: -\tau_r = 0 \quad \left[\begin{array}{l} \text{No absorption,} \\ \text{specular reflection} \end{array} \right] \quad (A-3)$$

which are analogous to the Newtonian equations used in aerodynamics if β_{∞} is replaced by the free-stream dynamic pressure. Eqs. (A-3), however, generally do not represent the photon reflection process existing on most satellite materials. That is, (1) some of the photons are not reflected but may be absorbed and transmitted through the material, and (2) the reflected photons may not rebound in a specular fashion. An extreme of the latter is the case of completely diffuse reflection in which there is no preferred direction for the rebounding photons. Then if the actual reflection process is assumed to vary linearly between specular and diffuse, Eqs. (A-2) may be more correctly written as

$$\begin{aligned} P_r &= \Lambda [(1-\lambda)\tau_i + \lambda p_d] \\ \tau_r &= \Lambda [(1-\lambda)\tau_i + \lambda \tau_d] \end{aligned} \quad (A-4)$$

where the subscript d refers to completely diffuse reflection; the reflectivity Λ represents the percentage of incident photons reflected; and λ is a measure of the diffusivity; i.e., $\lambda = 1$ is for completely diffuse reflection while $\lambda = 0$ is for completely specular reflection. Since there is no preferred direction for diffuse reflection, $\tau_d = 0$. Furthermore,

$$p_d \cong \frac{2}{3} p_i$$

Eqs. (A-4) now become

$$\begin{aligned} P_r &= \Lambda \left(1 - \frac{\lambda}{3}\right) p_i \\ \tau_r &= \Lambda (1 - \lambda) \tau_i \end{aligned} \quad (A-5)$$

and the total pressure and shearing stress may be written as

$$p = p_i + p_r = \left[1 + \lambda - \frac{1}{3}\lambda\lambda \right] \beta_{\infty} \frac{C_N^2}{C_{\infty}^2}$$

$$\tau = \tau_i - \tau_r = \left[1 - \lambda + \lambda\lambda \right] \beta_{\infty} \frac{C_N C_T}{C_{\infty}^2} . \quad (A-6)$$

For completely specular reflection, $\lambda = 0$, and Eqs. (A-6) become

$$p = (1 + \lambda) \beta_{\infty} \frac{C_N^2}{C_{\infty}^2}$$

$$\tau = (1 - \lambda) \beta_{\infty} \frac{C_N C_T}{C_{\infty}^2} . \quad (A-7)$$

Likewise, for diffuse reflection, $\lambda = 1$, and

$$p = \left(1 + \frac{2}{3}\lambda \right) \beta_{\infty} \frac{C_N^2}{C_{\infty}^2}$$

$$\tau = \beta_{\infty} \frac{C_N C_T}{C_{\infty}^2} . \quad (A-8)$$

For the examples to follow; i.e., the effect of solar radiation pressure on satellite torques, the specular equations, Eqs. (A-7) will be assumed for simplicity.

With the foregoing equations, the solar torque on a body of revolution may be calculated using the last of Eqs. (20), which is rewritten here as,

$$L_S = - \int_{SURF} \left\{ \left[p - \frac{C_N C_T}{C_{\infty}^2} \tau \right] \left[r r' + x - x_{cm} \right] \cos \theta \right. \\ \left. + \tau \frac{C_{\infty}}{C_T} \sqrt{1 + r'^2} \left[r \cos \theta \cos \alpha_i + (x - x_{cm}) \sin \alpha_i \right] \right\} r d\theta d\Omega \quad (A-9)$$

where the integration is over the sunny surface only and where α_s is the solar 'angle of attack'. Also, from Eq. (22),

$$\frac{C_M}{C_{00}} = \frac{1}{1+\mu^2} \left[r' \cos \alpha_s + s \mu \alpha_s \cos \delta \right].$$

For the present study, it is of more interest to calculate the initial torque slope (i.e., a measure of the stability) rather than the total torque. Then by comparing the solar torque slope with the aerodynamic and gravitational torque slopes, the "homing" characteristics of a satellite may be evaluated. Since the cylinder, sphere, and cone have been extensively treated in the aerodynamic analysis, it is convenient to calculate the solar torque slopes for these bodies. Thus, the cylinder, sphere and cone evaluations of the derivative of Eq. (A-7) with respect to α_s in the limit $\alpha_s \rightarrow 0$ are

$$\begin{aligned} \left(\frac{\partial L_s}{\partial \alpha_s} \right)_{\text{CYLINDER}} &= -\rho_{\infty} \frac{\pi D^3}{8} \left(\frac{k}{D} \right) (1-\lambda) \left(1 - 2 \frac{x_{\text{cm}}}{l} \right) \\ \left(\frac{\partial L_s}{\partial \alpha_s} \right)_{\text{SPHERE}} &= -\rho_{\infty} \frac{\pi D^3}{8} \left(1 - 2 \frac{x_{\text{cm}}}{D} \right) \\ \left(\frac{\partial L_s}{\partial \alpha_s} \right)_{\text{CONE}} &= -\rho_{\infty} \frac{\pi D^3 \alpha_s^2 \xi}{12} \left\{ 2\lambda \left(1 - \frac{3}{2} \frac{x_{\text{cm}}}{l} \cos^2 \delta \right) \right. \\ &\quad \left. + \frac{3}{2} (1-\lambda) \left(1 - \frac{x_{\text{cm}}}{l} \right) \right\} \end{aligned} \quad (\text{A-10})$$

where cylinder nose effects are included and where the specular photon reflection expressions, Eqs. (A-7), are used.

The corresponding aerodynamic torque slopes are, from Eqs. (64), (67) and (73),

$$\left(\frac{\partial L_A}{\partial \alpha}\right)_{\text{CYLINDER}} = -q_{\infty} \frac{\pi D^3}{4} \left(\frac{l}{D}\right) \left\{ \frac{3}{4} \left[\frac{1}{\sin^2 \delta} + \frac{\pi}{8 S_{90}} \frac{\sqrt{T_w}}{\sqrt{T_{\infty}}} \right] \frac{l}{D} + 1 \right\} \left(1 - 2 \frac{X_{cm}}{D} \right)$$

$$\left(\frac{\partial L_A}{\partial \alpha}\right)_{\text{SPHERE}} = -q_{\infty} \frac{\pi D^3}{4} \left\{ Q(S_A) + \frac{\sqrt{\pi}}{3 S_{90}} \frac{\sqrt{T_w}}{\sqrt{T_{\infty}}} \right\} \left(1 - 2 \frac{X_{cm}}{D} \right)$$

(A-11)

$$\begin{aligned} \left(\frac{\partial L_A}{\partial \alpha}\right)_{\text{CONE}} &= -q_{\infty} \frac{\pi D^3 \cot \delta}{4} \left\{ \frac{\sqrt{\pi}}{6 C_m \sin \delta} \frac{\sqrt{T_w}}{\sqrt{T_{\infty}}} \left(1 - \frac{3}{2} \frac{X_{cm}}{D} \cos^2 \delta \right) \right. \\ &\quad \left. + \left(1 - \frac{X_{cm}}{D} \right) \right\} \end{aligned}$$

where q_{∞} is the free-stream dynamic pressure.

Finally, the gravitational torque slopes may be found from Appendix A of Volume I. For a body of revolution, the initial torque slope is

$$\left(\frac{\partial L_G}{\partial \theta}\right)_{\theta \rightarrow 0} = \frac{3M}{r^3} (\bar{I} - \bar{I}_x) = -\frac{3M}{r^3} M \bar{I} \quad (\text{A-12})$$

where

M = product of Earth's mass and universal gravitational constant $\approx 1.495 \times 10^{26}$ lb^2/sec^2

r = distance from Earth's center to satellite mass center

θ = inclination of the satellite X axis to the local horizon.

The moments of inertia of the cylinder, sphere and cone have been determined in Section 3.4.2. Consequently, Eq. (A-12) becomes

$$\left(\frac{\partial L_g}{\partial \theta}\right)_{\text{CYLINDER}} = -\frac{31 m D^2}{r^3} \left[\frac{1}{16} - \frac{1}{3} \left(\frac{\kappa_{\text{cm}}}{l}\right) \left(\frac{l}{D}\right)^2 \right]$$

$$\left(\frac{\partial L_g}{\partial \theta}\right)_{\text{SPHERE}} = -\frac{7}{2} \frac{m D^2 \epsilon}{r^3} \left[1 - \frac{5}{2} \epsilon + 2 \epsilon^2 - \frac{1}{2} \epsilon^3 \right]$$

(A-13)

$$\left(\frac{\partial L_g}{\partial \theta}\right)_{\text{LOBE}} = -\frac{4 m D^2}{20 r^3} \left(\frac{\kappa_{\text{cm}}}{l}\right)^2 (4 - \cot^2 \delta)$$

where ϵ is the sphere payload fineness ratio and a function of κ_{cm}/D .

As an example, Eqs. (A-10), (A-11) and (A-13) are compared -- Figs. A-1, A-2 and A-3 for the special case of

$$\begin{aligned} \text{payload volume, } \mathcal{V} &= 10 \text{ ft}^3 \\ \text{payload volume ratio, } \mathcal{V}/\mathcal{V}_T &= 1/2 \\ \text{payload density, } m/\mathcal{V} &= 1/2. \end{aligned}$$

The optimum aerodynamic geometry from Section 3.4.2 is selected for these conditions. Also, a circular orbit is assumed so that q_{∞} may be written in terms of altitude (Ref. 7). The reflectivity R is taken to be 0.5, and the free-stream solar pressure P_{∞} is assumed constant and equal to 10^{-7} lbs/ft² (an average of Refs. 14, 15 and 16). As before, T_w is assumed to be 5500R and hence, Fig. 2 is applicable.

The curves in Figs. A-1, A-2 and A-3 clearly show, at least for these sample configurations, that solar torques are small when compared with aerodynamic torques for altitudes below 2 million feet (say). Moreover, if the aerodynamic and gravitational torque slopes are combined (a measure of Q_p^*), then the importance of the gravity gradient at the higher altitudes is clearly illustrated. That is, the sphere and cone (Figs. A-2 and A-3) have stable gravitational torque slopes at $\theta = 0$, and hence, augment the aerodynamic stability. Accordingly, the dominance of solar torques is delayed until higher altitudes are reached. The opposite effect is evident in the case of the cylinder (Fig. A-1) which has an unstable gravitational torque slope (for this example); i.e., the solar torque becomes dominant at a lower altitude due to the reduction of the combined aerodynamic and gravitational stability.

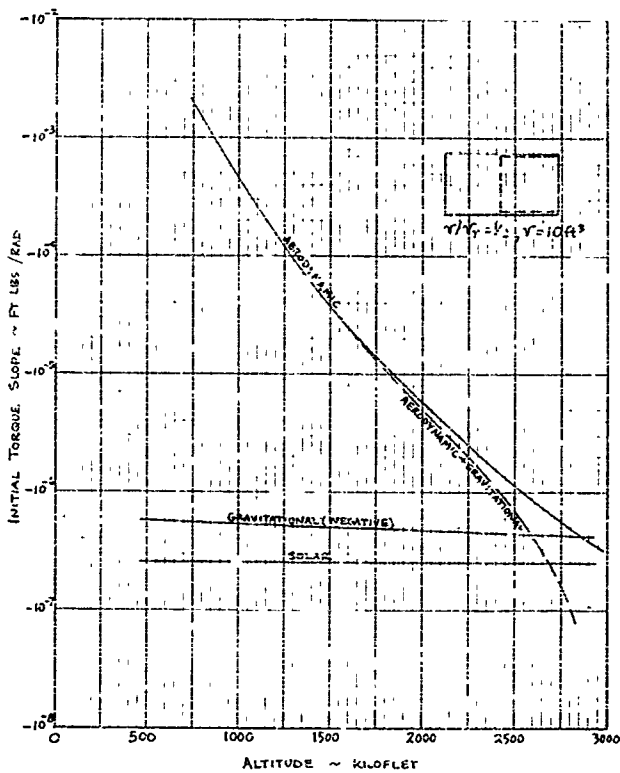


Figure A-1. Comparison of Various Initial Torque Slopes - Optimal cylinder

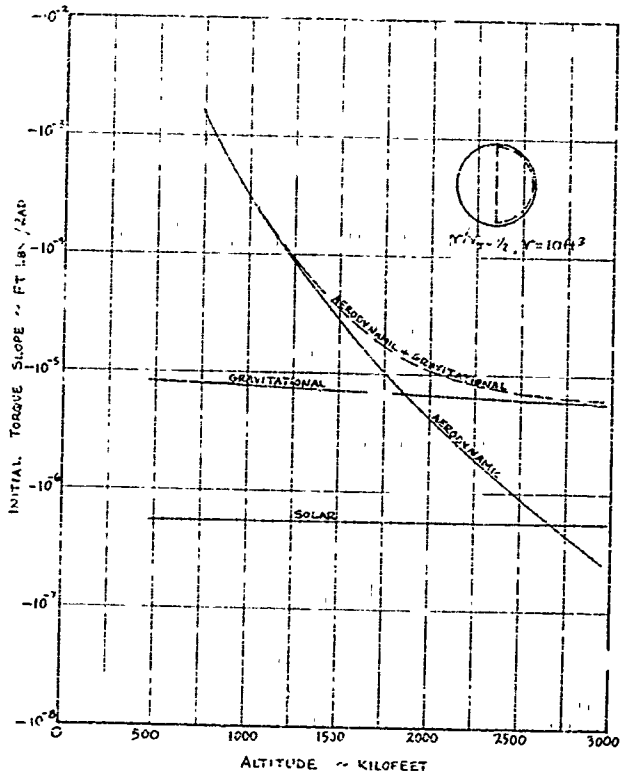


Figure A-2. Comparison of Various Initial Torque Slopes - Sphere

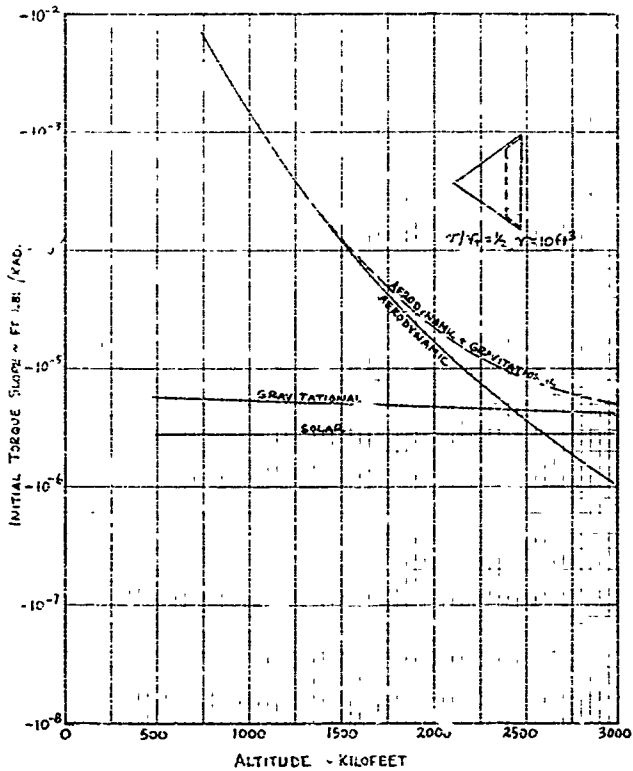


Figure A-3. Comparison of various Initial Torque Slopes - Contin. Cont.

BIBLIOGRAPHY

1. SchAAF, S. A. and Cramore, P. L., "Flow of Rarefied Gases," High Speed Aerodynamics and Jet Propulsion, Volume III, Section H (edited by H. W. Emmons), Princeton University Press, 1958.
2. SchAAF, S. A. and Talbot, L., "Mechanics of Rarefied Gases," Handbook of Supersonic Aerodynamics, Section 16, Naviro Report 1168 (Vol. 5), February 1959.
3. Patterson, G. H., Molecular Flow of Gases, John Wiley and Sons, Inc., New York, 1956.
4. Schrelo, D. M., "The Aerothermodynamics of Free Molecular Flow with Applications to Satellite Vehicle Design," North American Aviation, Inc., Report NA 59H-345, 17 August 1959.
5. Bell, S. and SchAAF, S. A., "Aerodynamic Forces on a Cylinder for the Free Molecule Flow of a Non-Uniform Gas," ARS Journal (Jet Propulsion), Vol. 23, September-October 1953, pp. 314-317.
6. Schrelo, D. M., "Approximate Free Molecule Aerodynamic Characteristics," ARS Journal, Vol. 30, No. 8, August 1960, pp. 765-767.
7. Minner, R. A., "Higher Atmospheric Densities and Temperatures Demanded by Satellite and Recent Rocket Measurements," ARS Preprint 781-52, 1959.
8. Talbot, L., "Free Molecular Flow Forces and Heat Transfer for an Infinite Cylinder at Angle of Attack," Jour. of the Aero. Sci., Vol. 24, No. 5, June 1957, pp. 456-459.
9. Stalder, J. A. and Zuri, V. J., "Theoretical Aerodynamic Characteristics of Bodies in a Free-Molecule Flow Field," NACA TN 2423, July 1951.
10. Lyon, F. J., "Heat Transfer Methods for High Speed Vehicles," North American Aviation, Inc., Report NA 58H-71, 10 February 1958.
11. Shelt, Ronald and Oler, Frederic C. R., "Some Experimental Results from the Agena Satellite Program," Aerospace Revi., February 1961.
12. SchAAF, S. A., "Recent Progress in Rarefied Gasdynamics," ARS Journal, Vol. 30, No. 5, May 1960, pp. 443-447.

13. Patterson, G. N., "Molecular Approach to Problems of High-Altitude, High-Speed Flight," AGARD Report No. 134, July 1957.
14. Wall, John K., "The Feasibility of Aerodynamic Attitude Stabilization of a Satellite Vehicle," ARS Preprint 787-59, May 1957.
15. Gatt, P. R., "Insolation of the Upper Atmosphere of a Satellite," Scientific Uses of an Earth Satellite, University of Michigan Press, 1956.
16. Roberson, R. E., "Attitude Control of a Satellite Vehicle - An Outline of the Problems," ARS Preprint 485-57, Presented at the Eighth International Astronautical Congress, Barcelona, Spain, 1957.
17. Stalder, J. R., Goodwin, G., and Ciesager, H. O., "A Comparison of Theory and Experiment for High-Speed Free-Molecule Flow," NACA Report 1032 1951.
18. Ashley, H., Applications of the Theory of Free Molecule Flow to Aeronautics," Jour. of the Aero. Sci., Vol. 16, No. 2, February 1949, pp. 95-104. Also: IAS Preprint No. 164, 1949.
19. Gustafson, W. A., "Aerodynamic Moments on Bodies Moving at High Speed in the Upper Atmosphere," ARS Journal, Vol. 29, No. 4, April 1959, pp. 301-303.
20. Gustafson, W. A., "The Newtonian-Diffuse Method for Computing Aerodynamic Forces," General Research in Flight Sciences - Volume II. Fluid Mechanics, Lockheed Missiles and Space Division Report LM5D-48381, January 1959.